TOUGHENING AND FAILURE MECHANISM OF COMPOSITE MATERIALS FOR IMPACT AND DAMAGE TOLERANCE

By

Wei Zhang

A DISSERTATION

Submitted to
Michigan State University
in partial fulfillment of the requirements
for the degree of

Mechanical Engineering-Doctor of Philosophy

2015

ABSTRACT

TOUGHENING AND FAILURE MECHANISM OF COMPOSITE MATERIALS FOR IMPACT AND DAMAGE TOLERANCE

By

Wei Zhang

Impact resistance is a material's ability to resist the force of a sudden impact. Compared to static loading, materials are more susceptible to a shock force applied over a short duration. Avoiding the catastrophic failure during impact events is the major challenge in the design of impact resistant material. Various approaches have been applied to increase the material's impact resistance. One approach is to combine two or more materials with distinguished physical or chemical properties to produce a new material with better performance without changing the characteristics of the constituents. The proposed study focuses on this approach, specifically, characterizing the toughening and failure mechanism of fiber-reinforced materials or laminate panels for impact and damage tolerance. Two types of materials are chosen for the research work. One is the transparent laminated glassy panel and the other is the natural fiber reinforced composite material, cortical bone. The material properties and failure mechanism were characterized through uniaxial tensile testing (both quasi-static and high strain rate), Charpy impact testing, and drop-weight impact testing. Post-failure examinations were carried out using a scanning electron microscope and bright field microscope. Numerical approaches including traditional finite element analysis method, multiscale modeling technique based on the classical computational homogenization scheme, and XFEM technique for discontinuities were applied to investigate the correlation between impact resistance and damage tolerance of the materials to their microstructure, hierarchical structures, and physical and mechanical properties of each constituent.

ACKNOWLEDGMENTS

The author would like to express her sincere appreciation to her advisor Dr. Srinivasan Arjun Tekalur for his persistent support, guidance, and advice throughout the duration of this research work. The author would also like to express her deepest appreciation to Dr. Alejandro Diaz, Dr. Seungik Baek, and Dr. Laura McCabe for all their valuable suggestions, help, and encouragement in this research.

The author would also like to thank Andy VanderKlok, Abhishek Dutta, Aiswarya Venkadachalam, David Gonzalez, and Oishik Sen, for providing an amicable environment in the laboratory. The author would like to thank the support of Gail Berry, Mike McClean, Adam, and Todd for their help throughout the course of the research. The author would like to acknowledge Ziwei Zhong, Brinn Cochrane, Brooke Peruski, and Steven Utz for helping run the experiments and machine the specimens. The authors also would like to thank Bellingar Packing (Ashley, Michigan) for providing the bovine femurs.

Last the author would like to express her gratitude to her parents, sister, and friends (Miao Wang, Shutian Yan, Lisi Pei, Danghe Shi, Wu Zhou, Fang Hou, and Christopher Cater) for their support, and thanks as well to everyone else who helped complete this research.

TABLE OF CONTENTS

LIST OF TABLES

LIST OF FIGURES

Chapter 1

Introduction

1.1 Objective and Expected Significance

Laminated transparent glassy panels have a wide application in both military structures such as transparent armour and gun shields, as well as civilian structures such as residential and commercial aquariums, automobile windshields, aircraft windows, etc. Implementing an optimal design to maximize its impact resistance, as well as keeping it lightweight and transparent is of great engineering interest in the design and manufacture of laminated glassy panel. As a fiber reinforced natural composite material, bone is lightweight, rigid, and tough. The unique biological microstructure of bone provides its special toughening mechanism to achieve its functional integrity including rigid support and metabolic function. Study of the relationship of its mechanical behavior, loading, and structure helps to develop understanding of the toughening mechanism of bone, improve its clinical treatment, and inspire new materials that mimic artificial bone.

1.1.1 Specific Aim 1

Transparency, light weight, and high impact resistance are three major factors needed to be considered when designing armour plates. The amorphous polymer, polycarbonate (PC), has been widely used as armour materials due to abilities to undergo large plastic deformation before failure, its light weight, its good transparency, and its ease of manufacturing. However, due to its ductility, PC is susceptible to penetration with localized plastic deformation in projectile testing. To increase energy dissipation and avoid localized deformation, commercial glass panels are typically designed as laminated structure built with two materials with contrasting material properties: ductility and brittleness. The reason is that brittle material reinforces the glassy panel by dissipating energy through cracking, and ductile material strengthens the brittle material by avoiding shattering into pieces. Glass is one of the typical brittle materials chosen for the laminated glassy panel due to its transparency. Recently, it was found that poly polymethyl methacrylate (PMMA), a transparent thermoplastic material, is a good alternative to glass due to its lighter weight and higher shatter-resistance. The density of PMMA, 1190 Kg/m^3, is the same as PC and is half of glass, 2400-2800 Kg/m^3. Additionally, the impact resistance of PMMA is almost double that of glass. The relatively rigid PMMA compensates the large compliance of PC and reinforces PC by increasing the area involved in damage. Furthermore, PMMA and PC are of almost the same index of refraction, which improves transparency of the glass panel. The PMMA and PC layers are bonded together with a soft interlayer, impact resistant adhesive.

The mechanical behavior of amorphous polymers is pressure sensitive. Thus, the yield stress under compression is different from the yield stress under tension. In tension, PMMA and PC exhibit a significantly contrasting failure mechanism. PC shows higher impact resistance and larger plastic deformation, and PMMA instead exhibits brittle failure and almost zero plastic deformation but a higher tensile strength. In compression, these two materials follow a same trend: large plastic deformation with strain relaxation after yielding, followed by a strain hardening. PC and PMMA are highly strain rate dependent materials. That means their yielding stress changes with strain rate. Due to the large plastic deformation, classical continuum mechanics are not accurate enough to predict the mechanical response of amorphous polymers. Many constitutive models based on large deformation theory have been developed for amorphous materials. Among the constitutive models, Arruda and Boyce's [1] three dimensional model based on a rubber elasticity spring system was the most popular used in modeling the mechanical response of PMMA and PC subjected to various strain rate.

Impact resistance of a glassy laminated panel depends on many factors, including the hierarchical configuration, thickness of each layer, mechanical properties of each layer, weight and geometry of the projectile, and impact velocity. The objective of the research work was to experimentally and numerically investigate the toughening mechanism of laminate PMMA and PC plates subjected to impact testing. First, low-velocity drop weight tests were conducted to evaluate the threshold condition and failure mechanism of PMMA and PC subjected to impact loading. The experimental methods and results are presented in Chapter 2. Then, the material model based on the existing Arruda and Boyce's physical model for amorphous polymers was coded and implemented in the commercial finite element modeling (FEM) software ABAQUS/EXPLICIT to predict the strain rate and pressure dependent behavior of PC. The failure behavior of monolithic PMMA and PC and layered PMMA/PC laminate subjected to low and high speed impact loading were then numerically investigated by ABAQUS. Lastly, an optimization approach was implemented using MATLAB and ABAQUS. The detailed methods, results, and finding of the numerical investigation are presented in Chapter 3.

1.1.2 Specific Aim 2

The second type of material studied is the fiber-reinforced cortical bone. As the major constitution of the skeleton of vertebrates, bone not only provides rigid support and protection to the soft tissues and organs but also participates in the fundamental metabolic activity such as the regulation of calcium. According to their shapes, bone can be classified as long bone, flat bone, short bone, etc. The femur and tibia are two typical long bones, which are the major support of vertebrate. The diaphysis of long bone is made of the dense cortical bone; and the two ends, called epiphysis, are made of the phony trabecular bone.

On the microstructural level (from 10-500 *mu*m) [2], mature cortical bone (also called osteon bone) can be considered a fiber-reinforced composite with fibers, cylindrical osteons, distributed in the interstitial lamellae matrix. Osteon, the major functional unit of mature cortical bones, grows along the loading axis (longitudinal direction) and comprises a center Haversian system surrounded by concentric lamellae. The longitudinal Haversian system surrounds blood vessels and nerves, which provide nutrition supplies and communicate with osteocyte contained in lacunae through small transverse canals, canaliculi. Osteons are connected to each other by oblique channels called Volkmann's canals. In the nanostructural level (from a few hundred nanometers to 1 *mu*m) [2], lamellae are formed by type I collagen fibrils and embedded mineral. The boundary between osteon and surrounding bone tissue, called the cement line, exhibits ductile properties due to its low mineral composition. Immature bone (laminar bone) is characterized as laminar structure. During its life span, bone consistently undergoes targeted and non-targeted remodeling in order to assure its functional integrity. Non-targeted remodeling is a bone adaption to meet the metabolic needs, and targeted remodeling is triggered by microdamage induced in daily fatigue activities. Deterioration of bone is a process of damage accumulation in the form of microcracking spanning a wide range of dimensional scales.

Osteon bone is an orthotropic composite material with a higher Young's modulus and strength along the longitudinal direction, which is the growing direction of ostoen or the loading axis, compared to the transverse direction, which is perpendicular to loading axis. Osteon with a central hole, cement line, and interstitial bone matrix are the three major components of osteon structure. The dimension, properties, micro-arrangement, and density of osteon are predicted to have a strong correlation to bone's overall mechanical performance, including microcracking initiation and propagation and remodelling of bone.

The objective of this research work was to investigate the failure and toughening mechanism of the unique osteon structure. Both FEM modeling and experimental methods were used to conduct the study. First, damage accumulation and effects on the strength and toughness of compact bovine bone was studied through uniaxial tensile testing, Charpy impact testing, and tensile split hopkinson bar (SHPB) testing. The experimental procedures and findings are presented in Chapter 4. Second, numerical studies were conducted to investigate the significant role of cement lines, density and size of osteons, and the properties of each constituent on the fracture mechanism of cortical bone through multi-scale modeling and XFEM technique in ABAQUS. The corresponding methods and results are presented in Chapter 5.

1.2 Background Rational and Review of Relevant Literature

In literature, some aspects of the previously mentioned aims have been investigated. This section provides an overview on current understandings relevant to the problems.

1.2.1 Transparent Laminated Panel

Many impact testing methods have been used to evaluate the impact resistance of transparent armor materials. The testing methods include low velocity drop weight impact tests [3, 4, 5, 6, 7, 8, 9, 10, 11], high velocity impact tests by use of an air gun [12, 13, 14, 15], and a shock wave impact by use of explosives [10, 11].

Among them, the low velocity drop weight impact test is popularly used to evaluate the threshold conditions indicating the onset of damage and to investigate the failure mechanism of the tested material. Liu [3] conducted a low velocity drop weight impact test on a monolithic PMMA plate using an instrumented drop weight impact tester. The variations of force with time and strain energy release rate were examined. The brittle-ductile transition temperature of PMMA was also evaluated to be in the range of 85°C to 96°C [3]. A low velocity impact and quasi-static failure of PMMA, based on global and local strain measurements, were conducted by Pearson and his colleagues [4]. In their work, Fiber Bragg Grating (FBG) sensors, were used to measure local strains, which were combined with the measurements from quasi-static indentation and low-velocity impact test to examine the failure mechanisms of PMMA. Multiple strikes were applied to the PMMA sample until failure. Stenzler [16] investigated the impact mechanics of transparent multi-layered polymer composites using an instrumented intermediate velocity impact test facility. The multi-layered structures with various bonding adhesives were investigated to evaluate the impact performance [16].

The ballistic impact response of PMMA plate structures attracts high attention due to its wide application in military defense [13, 17]. Sarva [17] studied the impact of a PMMA /PC (polycarbonate) hierarchical assembly by using a projectile at the impact velocities ranging from 300 to 550 m/s. It was shown that a hierarchical assembly exhibited higher penetration resistance compared to uniform distributed PMMA discs structure [17]. Hsieh [14] measured the ballistic impact response of coextruded PC/PMMA multilayered composites; the thickness of the PMMA plate was proved to play an important role in improving the ballistic performance of the same.

With the development of computational techniques, finite element modeling has been widely used in the study of the mechanical response of materials subjected to dynamic loading [3, 15, 19, 20, 21]. Finite element models were developed to predict the dynamic response of PMMA plates [3] and fibrous composite panels [19] subjected to a low velocity drop weight. A computational model [15] was used to study the ballistic impact response of PMMA plate structures. All the work shows that finite element simulation is a powerful tool to study the failure and fracture mechanism of materials.

Some study has been done on the optimization of layered PMMA/PC plate panels. The general procedures they followed includes thoroughly understanding the impact event, quantitatively finding the analytical solutions of the non-stationary strain problem, constructing the corresponding objective function according to the purpose of the optimization, and solving the objective function to achieve the desired optimization. The challenge of the optimization problems for the PMMA/PC layered plates is the difficulty in configuring the analytical solutions due to the unstable and instantaneous nature of brittle cracking. The classical laminate theory uses effective and reasonable assumptions to reduce the three-dimensional elasticity problems to solvable two-dimensional mechanics of deformable body problems [18]. Thus, the classical laminate theory is widely used to map the stress states of laminated plate subjected to stationary loading. However, to solve the layered plates subjected to impact loading, attempts have to be made to refine the classical theory so that it can be used to solve the dynamic loading problems [22, 23, 24, 25]. Smetankina [22] used a refined laminate theory on the basis of the hypothesis of the refined theory of Timoshenko to investigate the strain-stress state of multilayer plates under impulse and impact loading. In their work the transverse shear was taken into account and the displacement and the external load are expanded into Fourier series functions satisfying the problem boundary conditions. The numerical results had a good agreement with the experimental results. Shupikov [23] used Smetankina's refined laminate theory to investigate the optimal design of multilayer plates. In their work attempts were made to minimize the stress in layers and the total mass of the multilayered plates. Shokuhfar [24] investigated the optimal design of smart hybrid composite plates subjected to low-velocity impact using the plate theory developed by Whitney [25]. The interaction between the projectile and the plate was modeled by a system having two-degrees of freedom, consisting of spring-masses.

While the classical laminate theory are widely used to study the impact loading problem, many publications [26, 27, 28] deal with the dynamic loading problem from the aspect of wave propagation by application of wave theory. Chen [28] developed an analytical solution to the problem of one-dimensional high amplitude wave propagation in layered heterogeneous systems. The approach of his solution was to convert the initial velocity boundary value problem to a time dependent stress boundary value problem and the stress time history was obtained by means of superposition. Luo [27] investigated the stress wave propagation for a layered structure under impulsive loads. It was shown that the reduced amplitude and elongated pulse duration could be obtained with proper selection of materials and dimensions of layers when an incident stress pulse passed through a layered structure. Taha [26] developed a multi-objective optimization approach for design of blast-resistant composite laminates using carbon nanotubes. A simplified approach for wave propagation in bounded elastic media was adopted.

The optimal design of layered structure could also be implemented based on the concept [29, 30] of energy balance, during an impact event. Ray [30] optimized the energy dissipation characteristics of active constrained layer damping treatments of plates using a rational design approach. In his work, the governing equation was given based on the system energy balance, which includes the potential energy, kinetic energy, the work done by the piezo-electric control force, and the work dissipated in the viscoelastic core. Kam [29] investigated the optimal arrangements of laminated composite plates with maximum stiffness to the side constraints by applying the laminate theory as developed by Whitney. In Kam's work, the objective function was formulated in terms of the energy balance. The effects of aspect ratio, length to thickness ratio, and number of layers on the optimal lamination configuration were studied.

The literature review shows that there has been extensive research focused on the experimental and FEM study of laminated composite material, as well as optimal design of laminated composite material based on analytical analysis in the past decades. However, the unique characteristic and failure mechanism of PMMA and PC subjected to impact loading has yet not been fully understood.

1.2.2 Damage Accumulation in Bone

As a tough and lightweight natural composite, bone works as a scaffold to provide support and protect to internal organs. Understanding the failure mechanisms in bone is of great medical interest for preventing bone fracture failure.

The mechanical properties of compact bone have been widely studied in the past 50 years. Mcelhane [31] investigated the dynamic response of both fresh human and bovine femur subjected to dynamic compressive loading at strain rate up to 1000 s^{-1}. It was found that strain rates between 0.1-1 s^{-1} were the critical strain rates at which the energy absorption capacity and the maximum strain to failure exhibit large variation. The Young's modulus and ultimate stress increased with the strain rates. Saha and Hayes [32, 33]measured tensile impact properties of human and bovine compact bone using a pendulum-type instrumented tensile impact tester at a strain rate of 133 s^{-1}. Tensile strength, energy absorption capacity, and modulus of elasticity were found to be negatively correlated with the percentage area of secondary osteons. Crowninshiled and Pope [34] examined the response of compact bovine bone in tension at various strain rates (from 0.01 to 200 s^{-1}). Ultimate tensile stress both in longitudinal and transverse directions increased with the strain rate. Energy capacity reached maximum at a strain rate of 0.1 s^{-1}. Lewis and Goldsmith [35] designed a biaxial SHPB apparatus to measure the dynamic material properties of bovine femur in compression, tension, torsion, and combined torsion and compression. It was found that the bone exhibited viscoelastic properties in compression, and the fracture stress increased with strain rates. Currey [36] measured the material properties of compact bovine bone in tension at various strain rates (from 0.00013 to 0.16 s^{-1}). It was found that the strain rate effect on Young's modulus could be considered simply as the result of bone being a viscoelastic material, but the strain rate effect on yield strength and breaking strength could not be predicted directly from the viscoelasticity of bone with using any further facts. Wright and Hayes [45] conducted uniaxial tensile tests of cortical bovine bone at seven strain rates (from 5.3 x 10^{-4} to 237 s^{-1}). The ultimate strength, modulus of elasticity, and energy absorption capacity were found to increase with strain rates.

Robertson and Smith [37] investigated the compressive strength of the porcine mandible and its dependence upon microstructure and strain rate. Similar conclusions as Mcelhane were obtained. Ferreira [38] investigates the strain rate effects on the Young's modulus and ultimate strength of bovine femur bone subjected to compressive loading by SHPB. Ultimate strength was found to increase with the increase of strain rate. However, Young's modulus was found to decrease with the increase of strain rate. The study also showed that experimental results are scattering due to bone's highly heterogeneous structure. Pithious et al [39] measured the stress-strain relationship in both quasi-static and dynamic compressive loading (1000 s^{-1}). It was found that the bovine compact bone was three to four times more brittle under a dynamic load than under a quasi-static one. Adharapurapu et al. [40] used a two-bar three point bending apparatus, modified from SHPB, to measure the dynamic fracture toughness of bovine bone at high strain rates. The dynamic fracture toughness was significantly lower than the static one. The cleavage-like fracture was observed on the fracture surface at very high loading rates of 2 x 105 s^{-1}. Hansen et al [41] examined the strain rate effects on the material properties of human cortical bone in compression with strain rates from 0.14 to 29.1 s^{-1}, and in tension with strain rates from 0.08 to 17 s^{-1}. There was a significant difference found between the trend of the ultimate stress and failure strain in compression and tension. The ultimate stress in compression increased with strain rate, but the ultimate stress in tension decreased with strain rate. Stress and strain at yield decreased with strain rate for both compression and tension. However, the effects of strain rates on the post yield properties of bone not following the simple linear relationship implied that strain rate has a stronger effect on post yield deformation than on initiation of yielding.

The morphology and composition of the osteonal cement line in human bone were studied by Schaffler [42]. His results showed that collagen is absent in cement lines, which contain significantly less calcium and phosphorus but more sulfur than surrounding bone matrix. The intrinsic and extrinsic mechanisms were widely accepted to be the major toughening mechanisms for bone subjected to quasi-static loading. Intrinsic mechanisms [43] are microstructural damage mechanisms that operate ahead of the crack tip, and extrinsic mechanisms [43] act to shield the crack from the applied driving force and operate principally behind the crack tip in the crack wake. In detail, the toughening mechanism can be classified into crack deflection by osteons, crack bridging by collagen fibers, uncracked-ligament bridging, diffuse microcracking, and void. Vanishth et al. [44, 45] revealed a rising R-curve behaviour in bone. Rising R-curve behaviour is a direct result of the extrinsic toughening mechanisms. Kulin et al. [46] studied the effects of aging and loading rate on the compressive failure, fracture toughness, and resistance of equine cortical bone by use of split-Hopkinson pressure bar (SHPB). The post fracture surface analysis by use of both of the confocal microscopy and scanning electronic microscopy (SEM) showed a transition of ductile to brittle. It was attributed to the viscoelastic behavior of collagen which comprised 50 percent of bone structure. However, the failure mechanism of bone in high strain rate is still not fully uncovered due to the challenge of recording the high speed fracture process during high strain rate loading. It is pertinent to further investigate the toughening mechanism of bone subjected to high strain rate loading.

Although the existing research has shown that the mechanical properties of bone have some correlation to its microstructure, the role of cement lines and osteons on the overall mechanical properties of cortical bone and the initiation and propagation of microcracks has not been discovered yet. Thus, the proposed work was to conduct a series of research through experimental investigation and FEM analysis to address the above issues.

REFERENCES

REFERENCES

[1] Ellen M Arruda and Mary C Boyce. Evolution of plastic anisotropy in amorphous polymers during finite straining. *International Journal of Plasticity*, 9(6):697–720, 1993.

[2] Jae-Young Rho, Liisa Kuhn-Spearing, and Peter Zioupos. Mechanical properties and the hierarchical structure of bone. *Medical engineering & physics*, 20(2):92–102, 1998.

[3] Yanxiong Liu and Benjamin Liaw. Drop-weight impact tests and finite element modeling of cast acrylic/aluminum plates. *Polymer Testing*, 28(8):808–823, 2009.

[4] JD Pearson, MA Zikry, M Prabhugoud, and K Peters. Measurement of low velocity and quasi-static failure modes in pmma. *Polymer composites*, 28(3):381–391, 2007.

[5] Herzl Chai and Guruswami Ravichandran. On the mechanics of fracture in monoliths and multilayers from low-velocity impact by sharp or blunt-tip projectiles. *International journal of impact engineering*, 36(3):375–385, 2009.

[6] Md Akil Hazizan and WJ Cantwell. The low velocity impact response of foam-based sandwich structures. *Composites Part B: Engineering*, 33(3):193–204, 2002.

[7] Ik Hyeon Choi and Cheol Ho Lim. Low-velocity impact analysis of composite laminates using linearized contact law. *Composite structures*, 66(1):125–132, 2004.

[8] Md Akil Hazizan and WJ Cantwell. The low velocity impact response of an aluminium honeycomb sandwich structure. *Composites Part B: Engineering*, 34(8):679–687, 2003.

[9] Michael Hebert, Carl-Ernst Rousseau, and Arun Shukla. Shock loading and drop weight impact response of glass reinforced polymer composites. *Composite Structures*, 84(3):199–208, 2008.

[10] Srinivasan Arjun Tekalur, Arun Shukla, and Kunigal Shivakumar. Blast resistance of polyurea based layered composite materials. *Composite Structures*, 84(3):271–281, 2008.

[11] Shinji Ogihara, Tomoyuki Ishigure, and Akira Kobayashi. Study on impact perforation fracture mechanism in pmma. *Journal of materials science letters*, 17(8):691–692, 1998.

[12] S Sahraoui and JL Lataillade. Deformation and fracture of pmma at high rates of loading. *Journal of applied polymer science*, 51(9):1527–1532, 1994.

[13] L Roy Xu and Ares J Rosakis. An experimental study of impact-induced failure events in homogeneous layered materials using dynamic photoelasticity and high-speed photography. *Optics and Lasers in Engineering*, 40(4):263–288, 2003.

[14] Alex J Hsieh and John W Song. Measurements of ballistic impact response of novel co-extruded pc/pmma multilayered-composites. *Journal of reinforced plastics and composites*, 20(3):239–254, 2001.

[15] Sai Sarva, Adam D Mulliken, Mary C Boyce, and Alex J Hsieh. Mechanics of transparent polymeric material assemblies under projectile impact: simulations and experiments. Technical report, DTIC Document, 2004.

[16] Joshua S Stenzler and NC Goulbourne. Impact mechanics of transparent multi-layered polymer composites. In *Society for experimental mechanics-SEM annual conference and exposition on experimental and applied mechanics*, page V3, 2009.

[17] S Sarva, AD Mulliken, and MC Boyce. The mechanics of large-strain inhomogeneous deformation of polymeric materials under dynamic loading conditions. In *Journal de Physique IV (Proceedings)*, volume 134, pages 95–101. EDP sciences, 2006.

[18] YM Gupta and JL Ding. Impact load spreading in layered materials and structures: concept and quantitative measure. *International Journal of Impact Engineering*, 27(3):277–291, 2002.

[19] U Faroop and Karl Gregory. Computational modeling and simulation of low velocity impact on fibrous composite panels drop_weight un_partitioned model. *Journal of Engineering and Applied Sciences*, pages 1819–6608, 2009.

[20] Myungsoo Park, Jeonghoon Yoo, and Dong-Teak Chung. An optimization of a multi-layered plate under ballistic impact. *International journal of solids and structures*, 42(1):123–137, 2005.

[21] Pizhong Qiao, Mijia Yang, and Florin Bobaru. Impact mechanics and high-energy absorbing materials: review. *Journal of Aerospace Engineering*, 21(4):235–248, 2008.

[22] NV Smetankina, S Yu Sotrikhin, and AN Shupikov. Theoretical and experimental investigation of vibration of multilayer plates under the action of impulse and impact loads. *International journal of solids and structures*, 32(8):1247–1258, 1995.

[23] AN Shupikov, SV Ugrimov, AV Kolodiazhny, and VG Yareschenko. High-order theory of multilayer plates. the impact problem. *International journal of solids and structures*, 35(25):3391–3403, 1998.

[24] A Shokuhfar, SMR Khalili, F Ashenai Ghasemi, K Malekzadeh, and S Raissi. Analysis and optimization of smart hybrid composite plates subjected to low-velocity impact using the response surface methodology (rsm). *Thin-Walled Structures*, 46(11):1204–1212, 2008.

[25] JM Whitney and NJ Pagano. Shear deformation in heterogeneous anisotropic plates. *Journal of Applied Mechanics*, 37(4):1031–1036, 1970.

[26] Mahmoud M Reda Taha, Arife B Colak-Altunc, and Marwan Al-Haik. A multi-objective optimization approach for design of blast-resistant composite laminates using carbon nanotubes. *Composites Part B: Engineering*, 40(6):522–529, 2009.

[27] Xiaobo Luo, Amjad J Aref, and Gary F Dargush. Analysis and optimal design of layered structures subjected to impulsive loading. *Computers & Structures*, 87(9):543–551, 2009.

[28] X Chen, N Chandra, and AM Rajendran. Analytical solution to the plate impact problem of layered heterogeneous material systems. *International journal of solids and structures*, 41(16):4635–4659, 2004.

[29] TY Kam and FM Lai. Maximum stiffness design of laminated composite plates via a constrained global optimization approach. *Composite structures*, 32(1):391–398, 1995.

[30] MC Ray and A Baz. Optimization of energy dissipation of active constrained layer damping treatments of plates. *Journal of Sound and Vibration*, 208(3):391–406, 1997.

[31] J H McElhaney. Dynamic response of bone and muscle tissue. *Journal of Applied Physiology*, 21(4):1231–1236, 1966.

[32] S Saha and WC Hayes. Tensile impact properties of human compact bone. *Journal of biomechanics*, 9(4):243–251, 1976.

[33] S Saha and WC Hayes. Relations between tensile impact properties and microstructure of compact bone. *Calcified tissue research*, 24(1):65–72, 1977.

[34] RD Crowninshield and MH Pope. The response of compact bone in tension at various strain rates. *Annals of Biomedical Engineering*, 2(2):217–225, 1974.

[35] JL Lewis and W Goldsmith. The dynamic fracture and prefracture response of compact bone by split hopkinson bar methods. *Journal of biomechanics*, 8(1):27–40, 1975.

[36] JD Currey. The effects of strain rate, reconstruction and mineral content on some mechanical properties of bovine bone. *Journal of Biomechanics*, 8(1):81–86, 1975.

[37] Diane Margel Robertson and Dennis C Smith. Compressive strength of mandibular bone as a function of microstructure and strain rate. *Journal of biomechanics*, 11(10):455–471, 1978.

[38] F Ferreira, MA Vaz, and JA Simoes. Mechanical properties of bovine cortical bone at high strain rate. *Materials characterization*, 57(2):71–79, 2006.

[39] Martine Pithioux, Damien Subit, and Patrick Chabrand. Comparison of compact bone failure under two different loading rates: experimental and modelling approaches. *Medical engineering & physics*, 26(8):647–653, 2004.

[40] Raghavendra R Adharapurapu, Fengchun Jiang, and Kenneth S Vecchio. Dynamic fracture of bovine bone. *Materials Science and Engineering: C*, 26(8):1325–1332, 2006.

[41] Ulrich Hansen, Peter Zioupos, Rebecca Simpson, John D Currey, and David Hynd. The effect of strain rate on the mechanical properties of human cortical bone. *Journal of biomechanical engineering*, 130(1):011011, 2008.

[42] Mitchell B Schaffler, David B Burr, and Richard G Frederickson. Morphology of the osteonal cement line in human bone. *The Anatomical Record*, 217(3):223–228, 1987.

[43] RK Nalla, JS Stölken, JH Kinney, and RO Ritchie. Fracture in human cortical bone: local fracture criteria and toughening mechanisms. *Journal of biomechanics*, 38(7):1517–1525, 2005.

[44] D Vashishth, KE Tanner, and W Bonfield. Contribution, development and morphology of microcracking in cortical bone during crack propagation. *Journal of Biomechanics*, 33(9):1169–1174, 2000.

[45] D Vashishth, KE Tanner, and W Bonfield. Experimental validation of a microcracking-based toughening mechanism for cortical bone. *Journal of Biomechanics*, 36(1):121–124, 2003.

[46] Robb M Kulin, Fengchun Jiang, and Kenneth S Vecchio. Loading rate effects on the r-curve behavior of cortical bone. *Acta biomaterialia*, 7(2):724–732, 2011.

Chapter 2

Impact Behavior and Dynamic Failure of PMMA and PC Plates

2.1 Introduction

In this chapter, low velocity drop weight tests were conducted on the monolithic PMMA and bilayered PMMA and PC at various impact conditions to evaluate the threshold conditions indicating the onset of damage and failure mechanism of PMMA and PC plates. The experimental results will also serve as the validation for the numerical study in Chapter 3. The failure mechanism of monolithic PMMA was first studied through drop-weight impact tests with impact conditions of constant impact mass with various impact velocities, constant energy with various impact velocities and mass, and constant velocities with various impact mass. The threshold conditions, energy dissipation, and crack pattern were evaluated. Then, the bonded and unbonded bi-layered PMMA and PC structures was tested to investigate the effects of the interfacial bonding on the overall impact performance of layered PMMA plates. The failure mechanism was transversely compared through the monolithic PMMA plate, the bonded PMMA layered structures to the unbonded PMMA layered structures.

Table 2.1 Mechanical and physical properties of PMMA and PC plate.

Specimen	Density (kg/mm^3)	Modulus of Elasticity (MPa)	Poisson's Ratio	Tensile strength (MPa)	Shear Strength (MPa)	Compression Strength (MPa)
PC	1.2×10^{-6}	2300	0.3	65.5	41.4	86
PMMA	1.19×10^{-6}	3100	0.33	74.4	68.9	120.7

2.2 Experimental Procedures

The drop-weight impact tests were carried out through an Instron Dynatup 9250 drop weight tower (Fig. 2.1), which was equipped with a load cell above the tup to record the force history during the test. A velocity detector was mounted on the tup to measure the initial velocity of the impact. During the test, the 12.7 mm diameter hemispherical tup was raised to a specific height above the specimen and was allowed to drop the weight onto the specimen. The drop-weight range was 2.7-14.7 kg for the low weight drop. The tested specimens were commercial PMMA and PC plates, which were square plates (100 mm x 100 mm) with a thickness of 6.4 mm for the monolithic plate and 3.2 mm for each of the plates in a layered configuration. The mechanical and physical properties are summarized in Table 2.1. When the impact tower was armed, the specimen was fixed by a hydraulic clamp with a diameter of 76.2 mm. To avoid double impact, a rebound brake cylinder caught the tup after the first impact. All the experiments were performed at room temperature. The same tests were repeated twice, and similar results were obtained repeatedly.

2.3 Experimental Results

2.3.1 Monolithic PMMA Plates

To examine the failure mechanism of the mono-PMMA plates, multiple tests were conducted. The combinations included constant impact mass (6.61 kg) with various impact velocities, constant

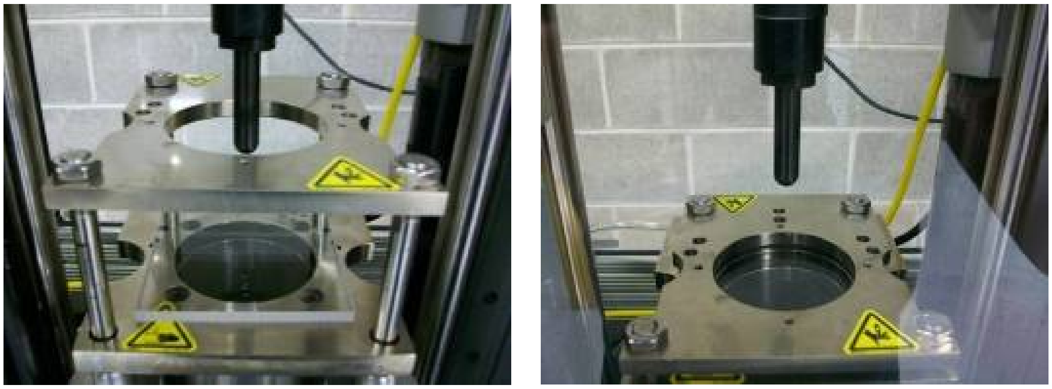

(a) **(b)**

Figure 2.1 Instron Dynatup 9250 drop weight tower: (a) before clamping; (b) after clamping.

energy (12 J) with various impact velocities and mass, and constant velocities (0.7 m/s and 1.0 m/s) with various impact mass.

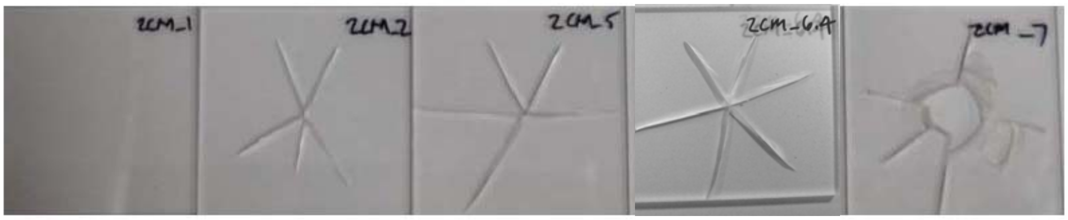

Figure 2.2 Post-failure pictures of mono-PMMA plates under constant impact mass: velocities are 0.7 m/s, 1.0 m/s, 2.0 m/s, and 3.0 m/s respectively from left to right.

The post-failure photographs of the monolithic PMMA plates under constant drop weights are shown in Fig. 2.2. It was observed that no visible crack was induced on the specimen under the impact velocity of 0.7 m/s, and 5 radial cracks propagated on the specimen under the velocities of 1.0 m/s and 2.0 m/s respectively. And 6 radial cracks were induced on the specimen under the velocities of 3.0 m/s. When the impact velocity reached 5.0 m/s, the specimen was penetrated. The curves of force versus time and force versus displacement of the specimen under the impact velocities of 0.7 m/s and 2.0 m/s are shown in Fig. 2.3 and Fig. 2.4 respectively. A smooth force against time curve was obtained when the velocity of 0.7 m/s was applied. However, when the specimen was subjected to the impact velocity of 2.0 m/s, the force curve first gradually reached a peak point and then underwent a sudden drop followed by oscillations and eventually rested on zero. The first sudden drop of the force curve indicated the onset of damage. Fig. 2.4 shows that the unloading process of the specimen under an impact velocity of 0.7 m/s did not fully follow the same track of the loading process. The phenomenon indicated that the PMMA plate exhibited elastic hysteresis behavior under impact loading. The corresponding hysteresis energy, the work done during the loading and unloading cycles, was calculated to be around 0.7 J. When the specimen was broken, the area under the force-displacement curve before the cracking point was the threshold energy. The threshold energy of the specimen subjected to an impact velocity of 2.0 m/s was calculated to be 2.8 J (Fig. 2.4).

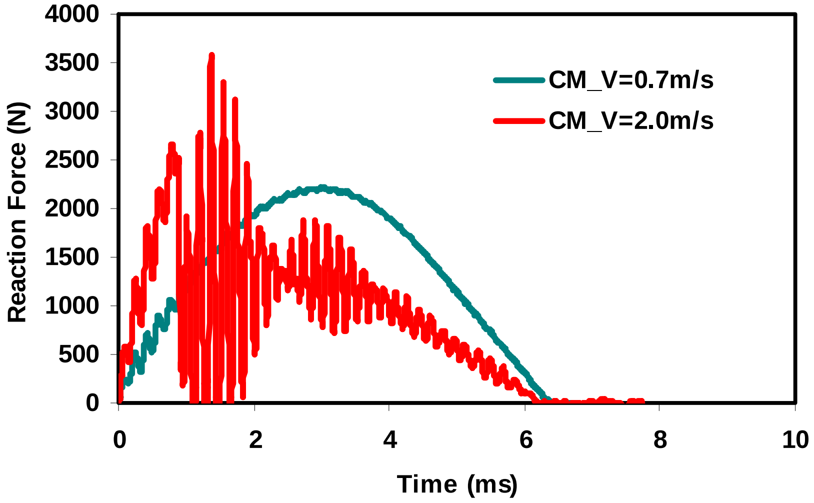

Figure 2.3 Reaction force versus time of mono-PMMA plates under constant impact mass of 6.61 kg.

The peak force and time to crack of the monolithic PMMA plates under constant impact mass are shown in Fig. 2.5. The plots showed that higher velocities induced higher reaction force and needed less time to initiate crack. The time to crack was around 3.0 ms, 2.1 ms, 0.76 ms, 0.73, and 0.26 ms respectively when the specimens were subjected to the impact velocities of 0.7 m/s,

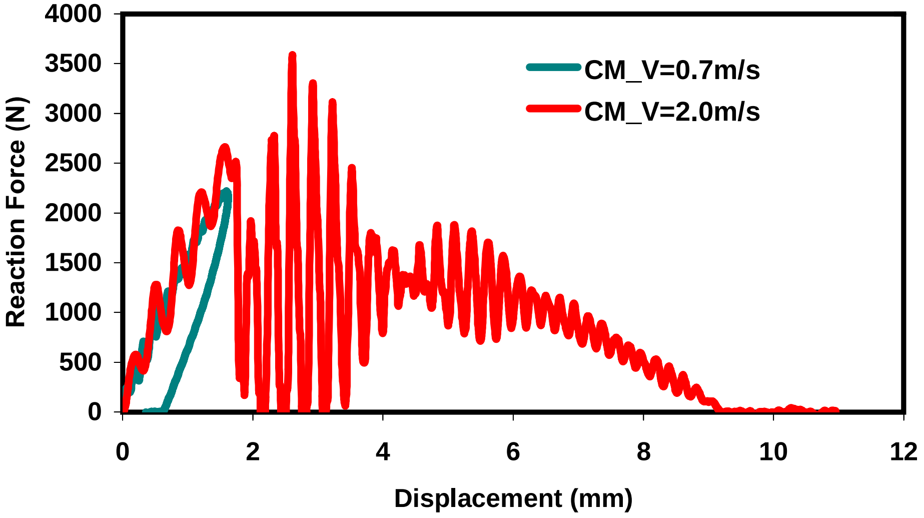

Figure 2.4 Reaction force versus displacement of mono-PMMA plates under constant impact mass.

1.0 m/s, 2.0 m/s, 3.0 m/s, and 5 m/s respectively. The corresponding threshold energies examined were in the range of 1.9 - 2.9 J, as summarized in Table 2.2. When the impact energy reached the threshold value, cracks initiated on the bottom surface of the PMMA plates and propagated to the top due to the maximum tensile stress induced on the bottom caused by bending. Fig. 2.6 showed the peak force and time to crack of the monolithic specimen under constant velocities, 0.7 m/s and 1.0 m/s. The curves also show that higher velocities induced higher reaction force and need less time to initiate crack. The peak force and time to crack of the monolithic PMMA plate under constant energy, 12 J, are shown in Fig. 2.7. The curves showed that higher drop-weight and lower impact velocity needed a longer time to fail compared to lower drop-weight and higher impact velocity. Thus, it can be concluded that the dynamic failure of PMMA is more sensitive to impact velocity than impact mass. The threshold energy of the monolithic PMMA plate under constant impact energy was kept in the range of 2.4 to 2.6 J, as summarized in Table 2.3.

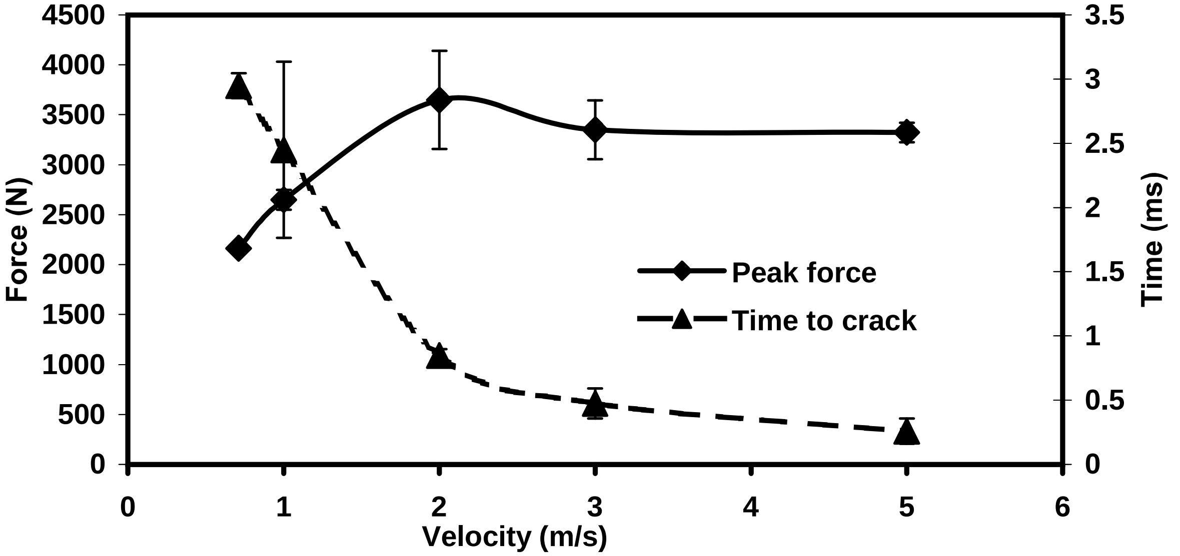

Figure 2.5 Peak force and time to crack of mono-PMMA plates under constant impact mass.

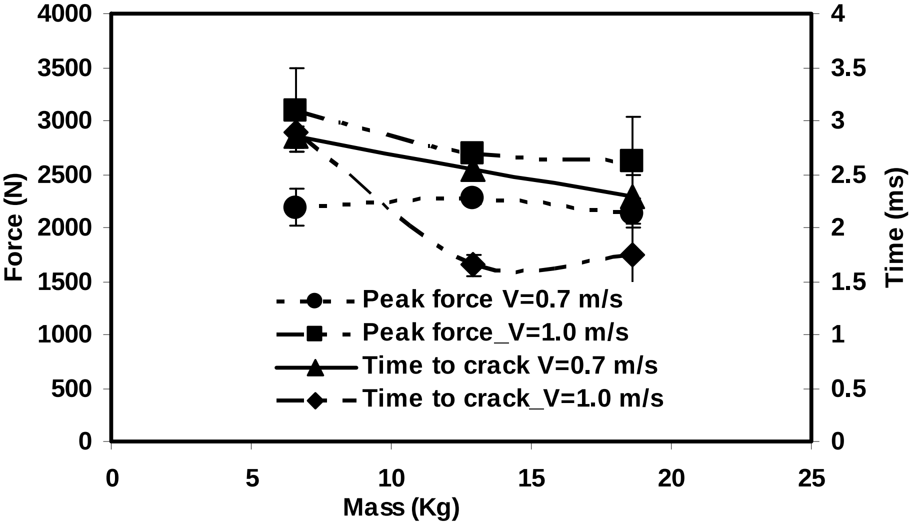

Figure 2.6 Peak force and time to crack of mono-PMMA plates under constant impact velocities (0.7 m/s and 1.0 m/s).

Table 2.2 Threshold energy of mono-PMMA plates under constant impact mass.

Impact Velocities (m/s)	0.7	1.0	2.0	3.0	5.0
Average Threshold Energy (J)	N/A	2.9 ± 0.21	2.8 ± 0.28	2.1 ± 0.07	1.9 ± 0.02

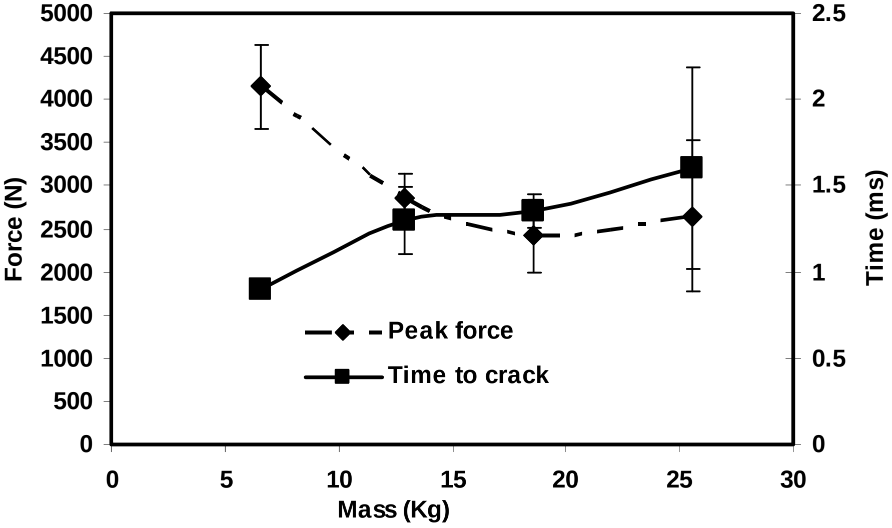

Figure 2.7 Peak force and time to crack of mono-PMMA plates under constant impact energy.

Table 2.3 Threshold energy of mono-PMMA plates under constant impact energy 12 J.

Impact Velocities (m/s)	1.88	1.35	1.11	0.94
Drop Weight (kg)	6.61	12.91	18.57	25.57
Average Threshold Energy (J)	2.4 ± 0.18	2.6 ± 0.42	2.4 ± 0.21	2.5 ± 0.35

2.3.2 Layered Plates

The mechanical performance of the composite materials can be changed or improved by increasing or decreasing the comprising layers, or by using different materials in each layers. In the current study, we seek to examine how the ductile PC affects on the impact performance of brittle PMMA plate, and furthermore how the interstitial layer affects on the overall impact behavior of the layered structures. To achieve these objectives, various configurations were designed: PMMA on the top of PC plates with weak and strong bonding, PC on the top of PMMA plates with weak and strong bonding, and PMMA on the top of PMMA plates with weak and strong bonding. The weak bonding was created by placing two plates together without adhesive. The strong bonding was achieved by using Loctite E-30CL glass bonder epoxy between layers. The tensile strength of the E-30CL epoxy is 55 MPa. When cured for 5 days at 25°C, the shear strength of the epoxy was 13.4 MPa with the substrate of PC, and 2.1 MPa with the substrate of PMMA. The adhesive was dispensed using a manual dispensing gun and was cured at room temperature. The layered combinations included PMMA on the top of PC plates, PC on the top of PMMA plates, and bi-layered PMMA plate structures. The impact scenarios of the bi-layered structures are summarized in Table 2.4.

Table 2.4 Summary of impact scenarios of bi-layered structures.

Models		Velocity (m/s)	Mass (Kg)	Energy (J)
PC on the top of PMMA	PC/PMMA_NA_CM_1	0.70	7.25	1.78
	PC/PMMA_NA_CM_2	1.00	7.25	3.55
	PC/PMMA_NA_CM_3	2.00	7.25	14.50
	PC/PMMA_NA_CM_4	3.00	7.25	32.63
	PC/PMMA_AD_CM_1	1.00	7.25	3.55
	PC/PMMA_AD_CM_2	2.00	7.25	14.50
	PC/PMMA_AD_CM_3	3.00	7.25	32.63
PMMA on the top of PC	PMMA/PC_NA_CM_1	0.70	7.25	1.78
	PMMA/PC_NA_CM_2	1.00	7.25	3.55
	PMMA/PC_NA_CM_3	2.00	7.25	14.50
	PMMA/PC_NA_CM_4	3.00	7.25	32.63
	PMMA/PC_AD_CM_1	1.00	7.25	3.55
	PMMA/PC_AD_CM_2	2.00	7.25	14.50
	PMMA/PC_AD_CM_3	3.00	7.25	32.63
PMMA on the top of PMMA	PMMA/PMMA_NA_CM_1	0.70	7.25	1.78
	PMMA/PMMA_NA_CM_2	1.00	7.25	3.55
	PMMA/PMMA_NA _CM_3	2.00	7.25	14.50
	PMMA/PMMA_NA _CM_4	3.00	7.25	32.63
	PMMA/PMMA_AD_CM_1	0.70	7.25	1.78
	PMMA/PMMA_AD_CM_2	1.00	7.25	3.55
	PMMA/PMMA_AD_CM_3	2.00	7.25	14.50

2.3.2.1 Bi-layered Structures of PMMA on the Top of PC

The post-failure photographs of the bi-layered structures of PMMA on the top of PC with weak bonding are shown in Fig. 2.8. The results showed that no visible crack was observed on both PC and PMMA plates when the specimens were subjected to the impact velocities of 0.7 m/s and 1.0 m/s respectively. However, when higher velocities (2.0 m/s, 3.0 m/s, and 5.0 m/s), were applied, 4 to 5 radial cracks were observed on the PMMA plates. The PC plates were kept unbroken for all the velocities. Furthermore, no ductile deformation was observed on the PMMA plates. The corresponding forces against time curves and impact energy against time curves are shown in Fig. 2.9. The unbroken specimens were indicated by the smooth curves.

Figure 2.8 Post-failure pictures of bi-layered structures with PMMA on the top of PC plates under constant impact mass: the velocities are 0.7 m/s, 1.0 m/s, 2.0 m/s, 3.0 m/s, and 5 m/s respectively from left to right; the first row is the top PMMA plates and the second row is the bottom PC plates.

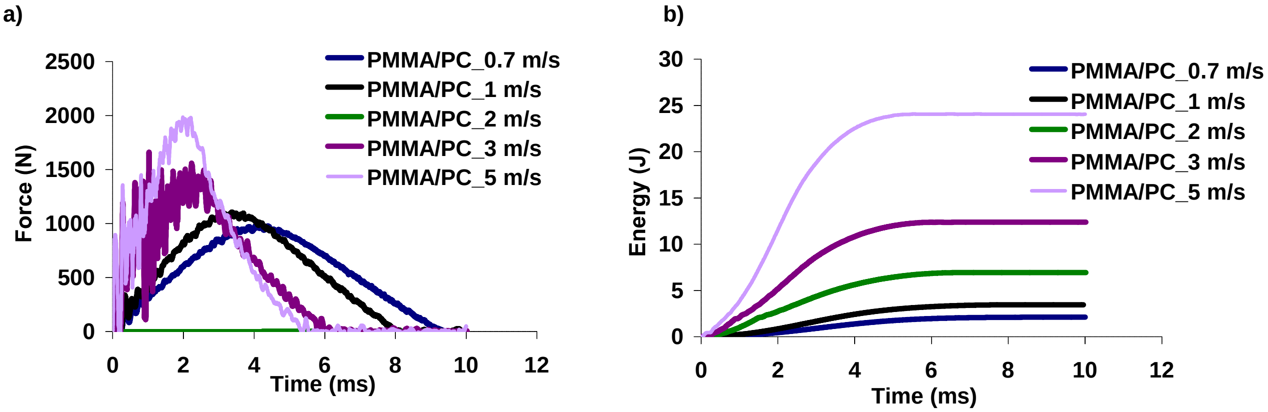

Figure 2.9 a)Reaction force history of bi-layered structures with PMMA on the top of PC with weak bonding under constant impact mass 6.61 kg;b)Impact energy history of bi-layered structures with PMMA on the top of PC with weak bonding under constant impact mass 6.61 kg

2.3.2.2 Bi-layered Structures of PC on the Top of PMMA

Fig. 2.10 shows the reaction force and time and impact energy and time relationships of the bi-layered structures of PC on the top of PMMA with weak bonding under constant impact mass 6.61 Kg. Compared to the bi-layered structures of PMMA on the top of PC, only one smooth curve was obtained when placing PC on the top of PMMA which means cracks occurred on all specimens except one under the impact velocity of 0.7 m/s. The phenomenon also can be observed on the post failure pictures, Fig. 2.11 . When the velocities were larger than 0.7 m/s, radial cracks were induced on all the PMMA plates. No crack was observed on the PC plates.

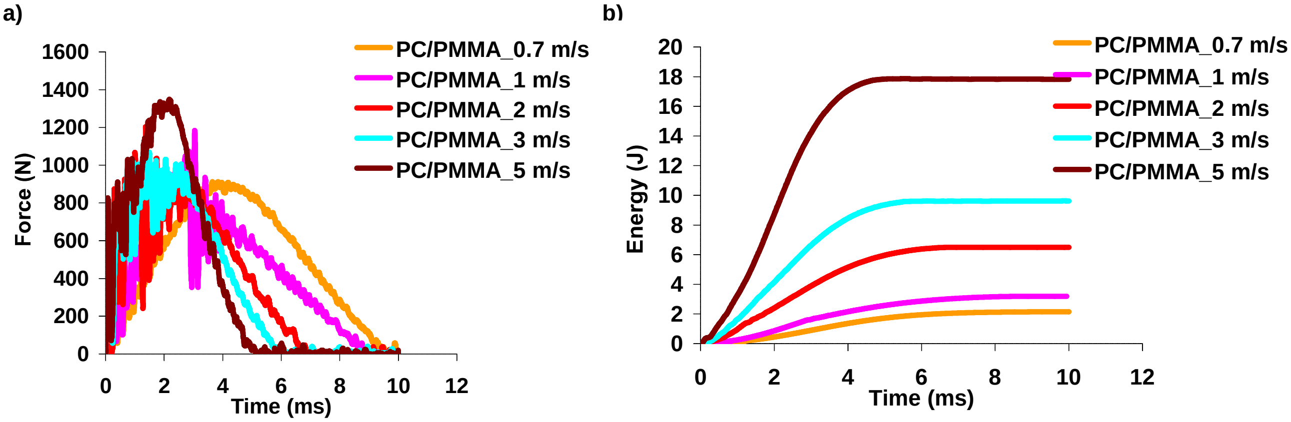

Figure 2.10 a)Reaction force history of bi-layered structures with PMMA on the top of PC with weak bonding under constant impact mass 6.61 kg; b)Impact Energy history of bi-layered structures with PMMA on the top of PC with weak bonding under constant impact mass 6.61 kg;

2.3.2.3 Bi-layered Structures of PMMA on the Top of PMMA

The post-impact pictures of the bi-layered PMMA/PMMA structures with weak bonding are shown in the Fig. 2.12. Brittle failure, revealed by radial cracking pattern, was observed on each PMMA plate of the bi-layer PMMA/PMMA structures with weak bonding when the impact velocity was larger than 0.7 m/s.

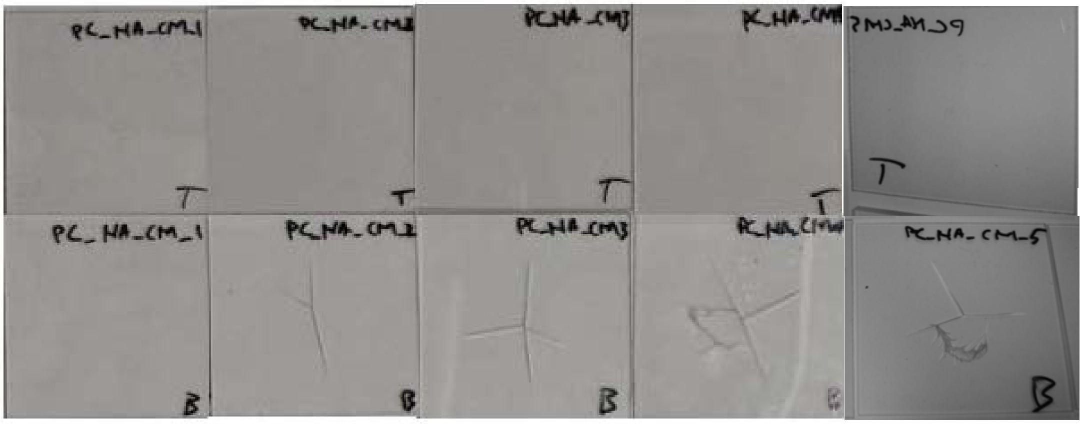

Figure 2.11 Post-failure pictures of bi-layered structures with PC on the top of PMMA plates under constant impact mass: the velocities are 0.7 m/s, 1.0 m/s, 2.0 m/s, 3.0 m/s, and 5 m/s respectively from left to right; the first row is the top PC plates and the second row is the bottom PMMA plates.

Figure 2.12 Pos-failure pictures of bi-layered PMMA plates under constant impact mass: the velocities are 0.7 m/s, 1.0 m/s, 2.0 m/s and 3.0 m/s respectively from left to right; the first row is the top PMMA plates and the second row is the bottom PMMA plates.

2.4 Discussion

The peak force and the time to crack of bi-layered PMMA and PC plates with weak bonding are summarized in Table 2.5. The results show that in the same impact conditions PMMA on the

Table 2.5 Threshold energy, energy dissipated, and time to crack of bi-layered PMMA and PC plates with weak bonding under constant impact mass 6.61 kg.

Specimen	Velocity (m/s)	Threshold Energy (J)	Time to Crack (ms)	Energy Dissipated (J)
PMMA/PC	0.7	N/A	N/A	2.1
PC/PMMA	0.7	1.5	4.0	2.1
PMMA/PC	1.0	N/A	N/A	3.5
PC/PMMA	1.0	1.6	2.8	3.2
PMMA/PC	2.0	2.0	2.3	6.9
PC/PMMA	2.0	1.7	1.4	6.5
PMMA/PC	3.0	1.9	1.7	12.4
PC/PMMA	3.0	1.6	1.3	9.6
PMMA/PC	5.0	0.8	0.3	24.1
PC/PMMA	5.0	0.7	0.3	17.8

Table 2.6 Peak force and time to crack of bi-layered PMMA and PC plates with strong bonding under constant impact mass 6.61 kg.

Specimens	Velocity (m/s)	Peak Force (N)	Time to Peak Force (ms)	Threshold Energy (J)	Energy Dissipated (J)
PMMA/PC_AD	1.0	2500	4.5	N/A	2.5
PC/PMMA_AD	1.0	2200	2	2.1	3.9
PMMA/PC_AD	2.0	3500	1.7	5.8	9.8
PC/PMMA_AD	2.0	2400	1	2.1	8.8
PMMA/PC_AD	3.0	3800	1.1	6.8	14.3
PC/PMMA_AD	3.0	3800	0.6	2	12.4

top PC needed longer time to failure compared to the bi-layered structures with PC on the top of PMMA. Compared to the post-failure pictures of the bi-layered structures with PC on the top of PMMA with weak bonding shown in Fig. 2.5, less damage was observed on the bi-layered structures with PMMA on top of PC shown in Fig. 2.8. The same results were observed on the strong bonding cases, the peak force, time to crack, and threshold energy which are summarized in Table 2.6. Thus, it can be concluded that PMMA on the top of PC can provide a better impact resistance compared to PC on the top of PMMA.

The comparisons were also made through the bi-layered PMMA and PC structures with strong bonding, the bi-layered PMMA and PC structures with weak bonding, and the mono-PMMA plates

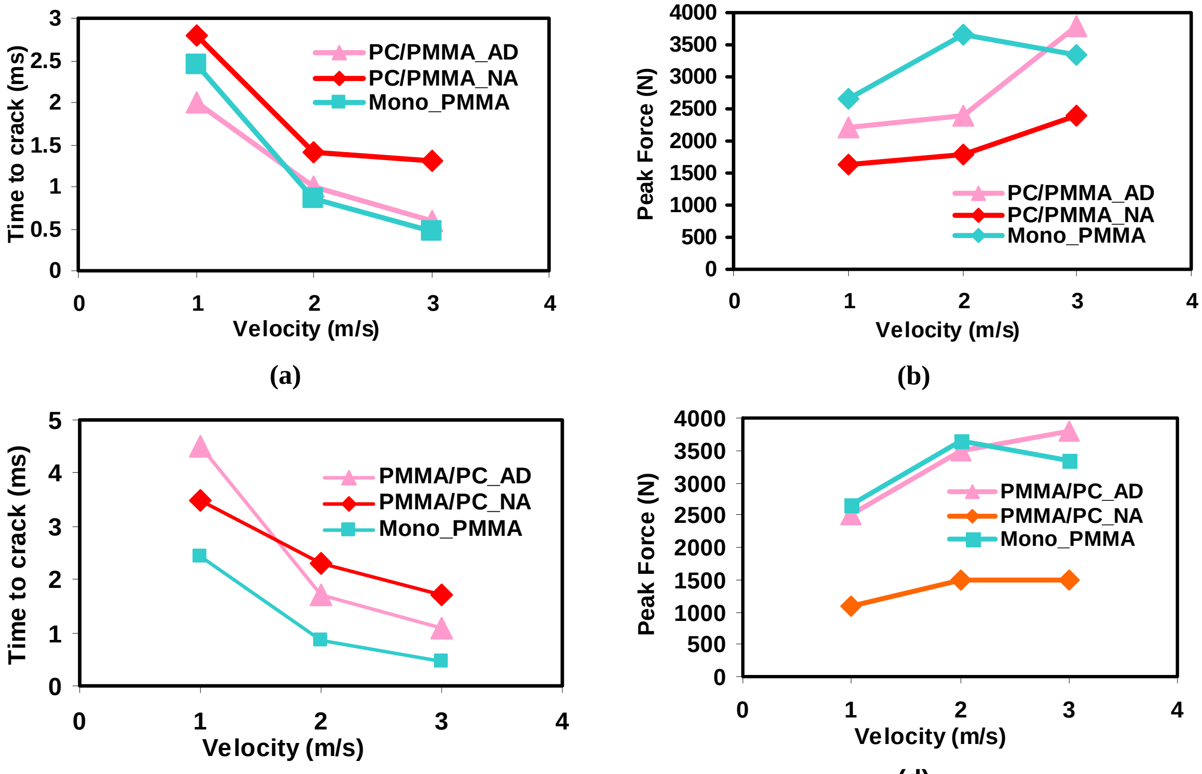

(a) (b)

(c) (d)

Figure 2.13 Comparison of the reaction force of the mono-PMMA plates to the bi-layered PMMA and PC structures with weak bonding and strong bonding under constant impact mass.

under constant impact mass, as shown in Fig. 2.13. It was found that compared to the monolithic PMMA plates and the strong bonded bi-layered structures, the bi-layered plates with weak bonding took a longer time to failure, and induced lower reaction force on the specimen. It is therefore the bi-layered PMMA and PC structures with weak bonding that showed advantage over both the monolithic PMMA and the strong bonded bi-layered PMMA and PC structures during impact events.

Fig. 2.14 shows the comparisons of the reaction forces, time to crack, and threshold energy of the bi-layered PMMA/PMMA plates to the mono-PMMA plates under constant impact mass. The results showed that the bi-layered structures led to lower reaction forces compared to the monolithic PMMA plates. The peak force of the bi-layered structure seemed to be half that of the

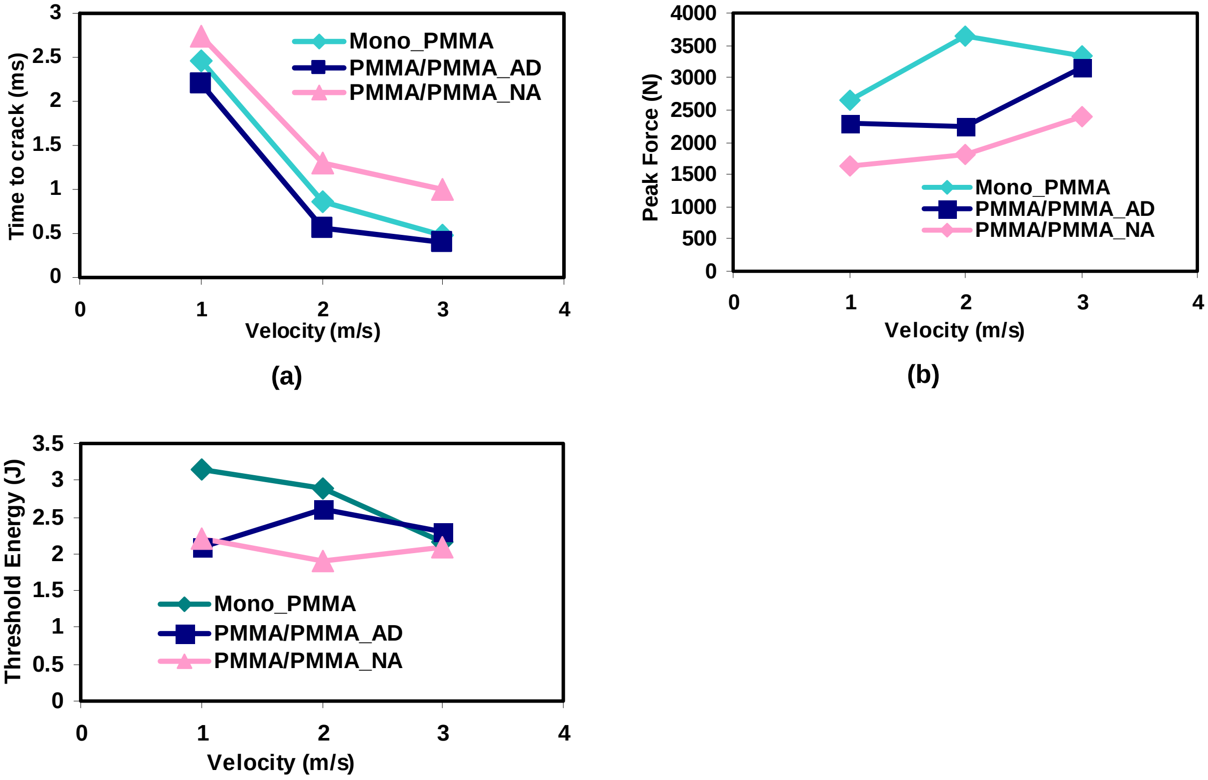

(a)

(b)

(c)

Figure 2.14 Comparison of the reaction force of the mono-PMMA plates to the bi-layered PMMA/PMMA structures with weak bonding and strong bonding under constant impact mass: (a) Time to crack; (b) Peak force; (c) Threshold energy.

mono-layered PMMA plates. The bi-layered structure took a longer time to initiate cracks and attain peak force. It is therefore concluded that layered-structures are beneficial to improve the impact resistance of the PMMA plates. For this particular adhesive, no benefits were observed on bi-layered PMMA/PMMA structures with strong bonding either. The average time to reach the peak force was around 2.2 ms for the bi-layered structure, and 1.7 ms for the mono-PMMA plate. The bi-layered structures seemed to delay the crack initiation by 29% of the mono-PMMA plate. Compared to the average threshold energy (2.5 J) of the monolithic PMMA plates, that (2.0 J) of the bi-layered structures (except the bi-layered structure with PMMA on the top of PC with strong bonding) was lower than the monolithic PMMA plates. The lower threshold energy of the bi-layered structures is because the threshold energy only depended on the PMMA plates since the PC plates were not broken during the impact events. The high threshold energy of the bi-layered structures with PMMA on the top of PC with strong bonding meant that cracking was induced not only on the PMMA plates but also on the PC plates

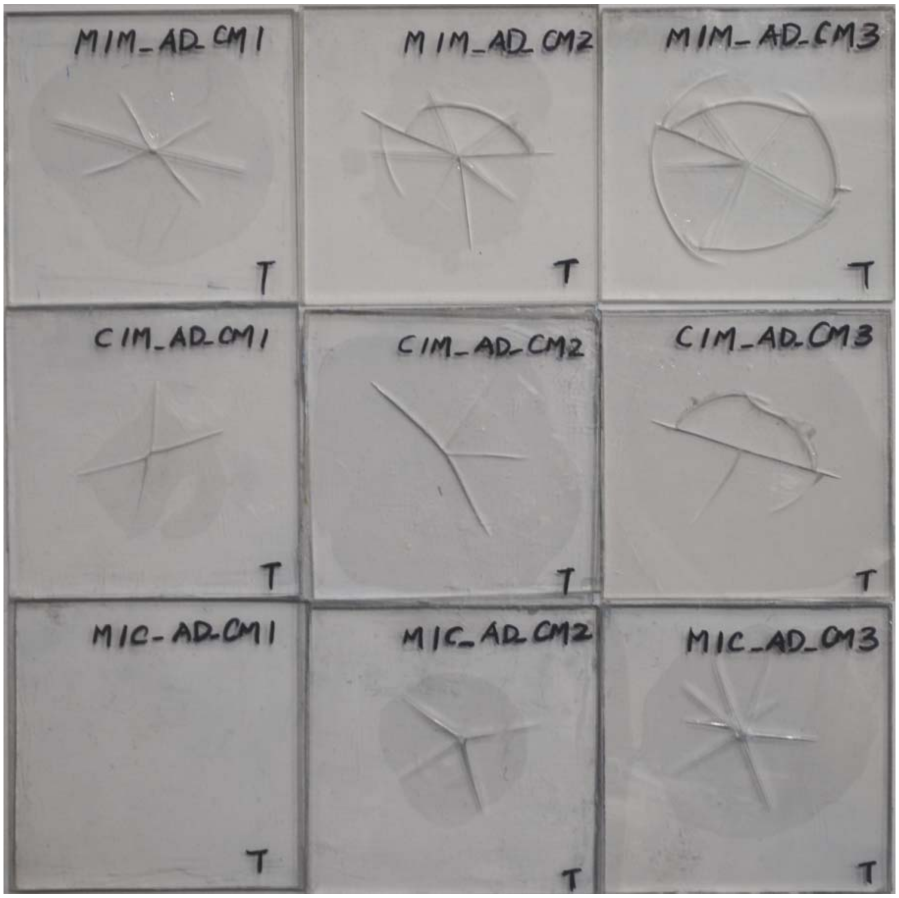

Figure 2.15 Post-failure pictures of the bonded bi-layered structures under constant impact mass: velocities are 1.0 m/s, 2.0 m/s and 3.0 m/s respectively from left to right; the first row is the bonded PMMA/PMMA plates, the second row is the bonded PC/PMMA plates and the third row is the bonded PMMA/PC plates.

From previous results, we can see that although both the PMMA plates were broken when the PMMA/PMMA bi-layered structures with weak bonding were subjected to impact velocity larger than 1.0 m/s, as opposed to the monolithic PMMA plates, it seemed that the natural gap between the two PMMA plates reduced the impact damage by some scale. The interlayer, the natural gap, therefore, has some effects on the impact performance of the tested specimen. Thus, to further evaluate how the soft interlayers affect the impact resistances of the bi-layered structures, the strong bonded bi-layer structures were tested. The post-failure results are shown in Fig. 2.15. In the mixed mode, brittle cracking indicated by the radial crack and ductile deformation indicated by the circular crack were observed on some specimens. Cracks were induced on all the PMMA plates except for the configuration with PMMA on top PC subjected to the impact velocity of 1 m/s. Localized delimitations were observed.

2.5 Conclusion

The low velocity impact response of the monolithic PMMA plate and a multi-layered PMMA/PC and PMMA/PMMA plates with weak and strong interface bonding were studied by both experimental and finite element methods. The threshold impact energies of the monolithic PMMA plates were found to be in the range of 2.0 to 3.1 J. It was found that the time to crack depended on the impact velocity. Higher velocity took less time to initiate crack. The PMMA plate exhibits elastic hysteresis behavior during drop weight impact test. The failure of PMMA is more sensitive to impact velocity than impact mass. For the same impact energy, higher impact mass and lower velocity needed a longer time to failure compared to lower impact mass and higher impact velocity. The findings agreed well with literature [1, 2, 3, 4].

The bi-layered structures exhibited lighter deformation compared to the monolithic PMMA plates. The layered structures seemed to delay the time to failure and create a lower reaction force. Under the same impact conditions, the average time to failure of the bi-layer structures with the PMMA on top of PC was 170% of the monolithic PMMA plates. When designing a bi-layered

PMMA and PC structure, a higher impact resistant can be obtained by putting the PMMA plate facing the impactor because the maximum tensile stress is induced in the bottom PC layer, which is able to undergo more deflection before cracking. For the particular Loctite E-30CL glass bonder Epoxy adhesive, bi-layer configuration with weak bonding has an advantage over the strong bonding case during an impact event. Results of this work clearly demonstrate that layered-structures are beneficial to improve the impact resistance of the PMMA plates and interfacial bonding plays a role in determining the extent of the same.

REFERENCES

REFERENCES

[1] Yanxiong Liu and Benjamin Liaw. Drop-weight impact tests and finite element modeling of cast acrylic plates. *Polymer Testing*, 28(6):599–611, 2009.

[2] JD Pearson, MA Zikry, M Prabhugoud, and K Peters. Measurement of low velocity and quasi-static failure modes in pmma. *Polymer composites*, 28(3):381–391, 2007.

[3] Michael Hebert, Carl-Ernst Rousseau, and Arun Shukla. Shock loading and drop weight impact response of glass reinforced polymer composites. *Composite Structures*, 84(3):199–208, 2008.

[4] Shinji Ogihara, Tomoyuki Ishigure, and Akira Kobayashi. Study on impact perforation fracture mechanism in pmma. *Journal of materials science letters*, 17(8):691–692, 1998.

Chapter 3

Failure and Toughening Mechanism of PMMA and PC Laminated Glassy Panel Subjected to Impact Loading

3.1 Introduction

Transparent laminate composite is usually made of two materials with contrast material properties, ductile and brittle, to enhance the overall fracture toughness of the laminate [1, 2, 3, 4]. The transparent glassy polymer, polymethylmethacrylate (PMMA), brittle in nature, and polycarbonate (PC), ductile in nature, are the two typical materials used in laminate composite due to their light weight, transparency, low cost, and machinability. PMMA dissipates energy through cracking and usually shatters into pieces when subjected to impact loading. On the contrary, PC absorbs energy by plastic deformation and usually is penetrated with a local deformation with four steps of failure behavior: the elastic dishing, petalling, deep penetration, and cone cracking and plugging [5]. It is hypothesized that the glassy laminate composite manufactured by alternatively gluing the thin layers of PMMA and PC together has a higher energy absorption capacity than the monolithic PC or PMMA when subjected to impact loading. Although this phenomenon has been experimentally observed and proved [6, 7, 8], the toughening mechanism including the interaction between impact resistance and impact velocities, geometry and aspect ratio of projectile, and thickness and mechanical properties of each layers has not been yet fully understood.

As amorphous thermoplastic, PMMA and PC are pressure, loading rate, and temperature dependent. The pressure dependent behavior is reflected by the different stress-strain response under tension and compression [9, 10, 11, 12, 13, 14]. The deformation of amorphous polymer is governed by the state of orientation of the chain network of the microstructure. During the process of deformation, the chain network changes from random orientation to a highly orientated state, which is the preferred state in strengthening the polymer [15, 9, 12]. The pressure dependent behavior of amorphous polymer is the result of different orientation processes in tension and compression: planar orientation process in compression and uniaxial orientation process in tension [9] respectively. PMMA and PC are highly strain rate dependent, exhibiting an increase in yield strength with an increase in strain rate [16].

The impact behavior of PMMA and PC subject to various strain rates has been studied extensively through use of various impact testing methods including low velocity drop-weight, impact tests [17, 18, 19, 20, 21], high velocity impact by use of an air gun [2, 22, 23, 4, 24, 25], and shock wave impact by use of explosives [26, 27]. It was found that multiple radial cracks are usually induced in the PMMA plate subjected to low to intermediate impact load, and the energy release rate of PMMA is found to be in the range of 252-728 J/m [19]. The thickness or volume fraction of the PMMA plate was observed to play an important role in improving the ballistic performance of multilayered composites subject to high velocity impact ranging from 300 to 550 m/s [1, 2]. The failure of a PMMA and PC laminate plate with a higher volume fraction of PMMA is dominated by brittle cracking. On the contrary, the failure is dominated by ductile deformation. The experimental observations showed that the impact resistance of PMMA and PC laminate depends on many variables. To avoid a case-by-case or trail and error study, an optimal design procedure for maximizing the impact-resistance of glassy panels should be conducted.

The challenge of the optimization methods for the PMMA/PC layered plates is the difficulty in configuring the analytical solutions for dynamic problems due to the unstable and instantaneous nature of brittle cracking subjected to impact loading. The classical laminate theory, wave theory, and energy method are the three major approaches in constructing the analytical solutions for optimizing the impact resistance of laminate structures. Although the classical laminate theory is widely used to map the stress states of laminated plate subjected to stationary loading, solving the layered plates subjected to impact loading is still challenging. Attempts have to be made to refine the classical theory so that it can be used to investigate the strain-stress state of multilayer plates under impulse and impact loading [28, 29, 30]. Smetankina [30]used a refined laminate theory on the basis of the hypothesis of the refined theory of Timoshenko to investigate the strain-stress state of multilayer plates under impulse and impact loading. In his work, the transverse shear was taken into account and the displacement and the external load are expanded into Fourier series functions satisfying the problem boundary conditions. The numerical results had a good agreement with the experimental results. Shupikov [29] used Smetankinas refined laminate theory to investigate the optimal design of multilayer plates. In his work, attempts were made to minimize the stress in layers and the total mass of the multilayered plates. The approach of wave propagation in layered heterogeneous systems was to convert the initial velocity boundary value problem to a time dependent stress boundary value problem, and the stress time history was obtained by means of superposition [31, 19, 32]. Luo [19] investigated the stress wave propagation for a layered structure under impulsive loads. It was shown that the reduced amplitude and elongated pulse duration could be obtained with proper selection of materials and dimensions of layers when an incident stress pulse passed through a layered structure. The optimal design of layered structures could also be implemented based on the concept energy balance [33, 34] during an impact event. Ray [34] optimized the energy dissipation characteristics of active constrained layer damping treatments of plates using a rational design approach. In his work, the governing equation was given based on the system energy balance, which includes the potential energy, kinetic energy, and the work done by the piezo-electric control force, and the work dissipated in the viscoelastic core.

The previous literature shows that there has been extensive research focused on the experimental and FEM study of laminated composite material, as well as optimal design of laminated composite material based on analytical analysis in the past decades. However, the unique characteristic and failure mechanism of PMMA and PC subjected to impact loading has yet not been fully understood. Thus, in this research of work, a material model for amorphous materials with large deformation was first implemented in ABAQUS/EXPLICIT based on the existing Boyce and Arruda's [9] physical model to predict the pressure and strain rate dependent stress-strain relationship of PC. Second, the impact behavior of monolithic PMMA and PC and layered PMMA/PC laminate at low and high impact loading was numerically investigated by use of ABAQUS/EXPLICIT and the failure mechanism, crack pattern, and energy dissipation were transversely compared. Lastly, to further evaluate material characteristics such as strain-rate sensitivity and pressure dependent behavior of the monolithic components on the ballistic performance of these PMMA/PC laminated systems, an optimal study by incorporating MATLAB optimization tool box and ABAQUS FEM simulations were conducted. The role of aspect ratio, yielding stress of PC, and failure stress of PMMA on the impact behavior were studied. This work serves as a design tool for effectively choosing materials and structures for optimizing ballistic performance of ceramic-plastic laminates-based armor.

3.2 Methods

As amorphous polymers, both PMMA and PC are strain rate, temperature, and pressure dependent materials. A typical stress-strain curve of PMMA and PC under compression is shown in Fig. 3.1. The deformation includes three parts: linear elastic deformation, strain softening, and strain hardening. From the point view of microscopic structure of PMMA and PC, the linear elastic region is where the applied force has not passed the intermolecular interactive barriers and the molecular structures are rotating or sliding along each other. After breaking the intermolecular force, molecular segments change to new positions which causes the strain softening. The strain hardening is due to the contribution of the segments reordering, which tends to orient parallel with loading direction to maximize molecular force.

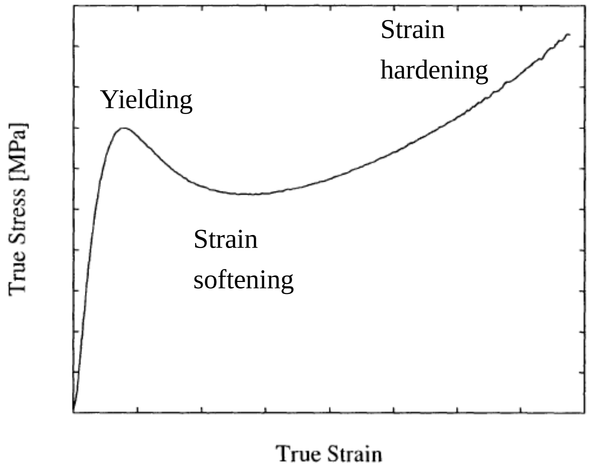

Figure 3.1 Schematic representation of amorphous polymers under compression.

In the past decades, many constitutive equations have been proposed to predict the linear-softening-hardening behavior of amorphous glassy polymers. Among them, Arruda and Boyce's three-dimensional physical-based model [9] is one of the most adopted. Boyce's model was developed based on Harvard and Thackray [35] and Argon's physical model [15], which divided resistance inside the amorphous materials into two parts: one is the molecular resistance; another is the entropic resistance. The entropic resistance contributes the strain hardening of the materials, and the molecular resistance accounts for the strain softening. Thus, a material subroutine based on Arruda and Boyces constitutive model for amorphous polymers was developed and implemented in ABAQUS to predict the strain rate and pressure dependent behavior of PC subjected to uniaxial loading at different strain rate. The elastic material properties used in the constitutive model are shown in Table 3.1.

Table 3.1 Material properties for PC and PMMA.

Material	**Density (kg/mm3)**	**Modulus of Elasticity (MPa)**	**Poisson's Ratio**
PC	**$1.2\text{x}10^{-6}$**	**2300**	**0.3**
PMMA	**$1.19\text{x}10^{-6}$**	**3100**	**0.33**

The PMMA was simulated as a brittle material using the brittle cracking material model of ABAQUS. When elements are under compression, the stress-strain response is linear. The failure of an element is caused by tensile failure. Thus, when the maximum stress at the element is larger than the post yielding stress, the crack will initiate until failure of the element. Failed elements will be removed from computation. The elastic material properties of PMMA are shown in Table 3.1.

The geometry and mesh of the FEM analysis are shown in Fig. 3.2. The overall thickness of the laminate panel simulated is 6.4 mm. The projectile was modeled as a rigid body, and an 8-node C3D8 linear brick element was used for modeling the specimen. Two types of projectile were simulated. One is spherical projectile with a radius of 6.35 mm (Type 2), which was used for the low velocity impact test. The other was the blunt projectile with a radius of 2.73 mm (Type 1) which was used for the high velocity impact test. The peripheries of the laminate plates were

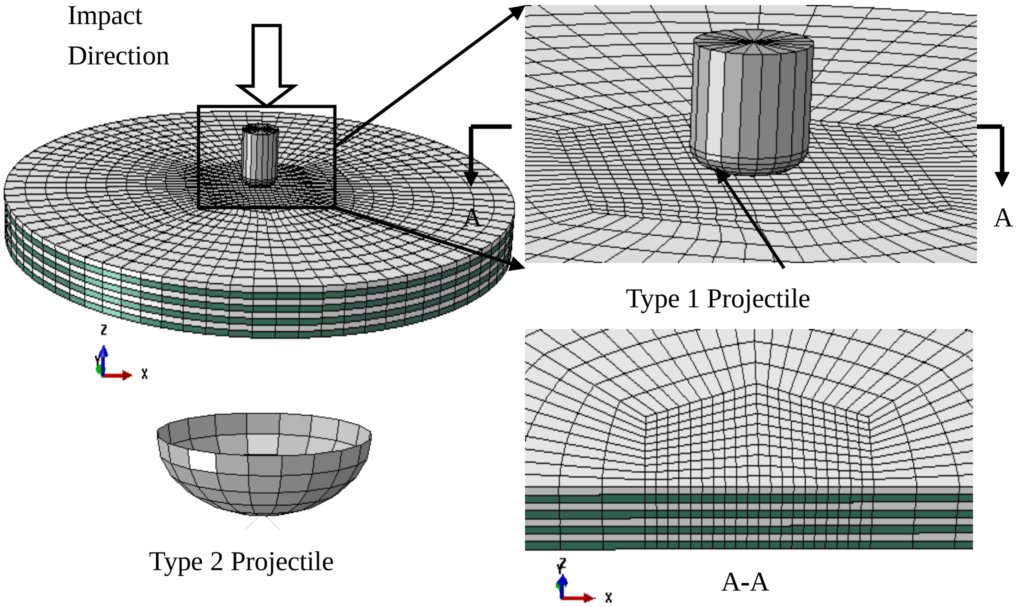

Figure 3.2 Geometry and mesh of FE simulations.

fixed in the impact direction. The mesh density of the specimen was chosen based on the low cost of computation without compromising the accuracy of the results. Impact force, energy, and stress and strain contour were obtained. The various configurations of the laminate structure simulated are summarized in Table 3.2. The σ_{pc} and σ_{PMMA} are the yielding stress of PC and failure stress of PMMA respectively.

Table 3.2 Various configurations of the laminate plate panel simulated.

Case No.	**Impact Velocity (m/s)**	**Radius of Projectile (m)**	**Mass of Projectile (Kg)**	**Numbers of Layer**	**Sequences of Plates**	$\frac{\sigma_{PC}}{\sigma_{PMMA}}$	**Type of Interface**
1	5	0.00273	7.1	8	MCMCMCMC	0.96	bounded
2	5	0.00635	7.1	8	MCMCMCMC	0.96	bounded
3	300	0.00273	0.0032	8	MCMCMCMC	0.36	bounded
4	300	0.005	0.0032	8	MCMCMCMC	0.36	bounded

The impact resistance depends on thickness of each layer, material properties of each layer, sequences of layers, aspect ratio of plates to projectile, and impact velocities, as well as the mass of projectile. Thus, optimization is conducted based on some of the above design variables. The objective function was to maximize the energy absorption, which was equivalent to the minimum residual velocity. The energy balance during an impact event is shown as

$$E_{dissipated} = K_{initial} - K_{residual} = \frac{1}{2}m(v_{initial}^2 - v_{residual}^2) \tag{3.1}$$

where $K_{dissipated}$, the dissipated energy;$K_{initial}$, initial kinetic energy; $K_{residual}$, residual energy; m, the mass of projectile; $v_{initial}$, the initial velocity of the projectile; and $v_{residual}$, the residual velocity of the projectile.

The optimal study was performed by incorporating MATLAB and FEM simulations by ABAQUS. The MATLAB fmincon function was used as the searching method to find the minimum of objective function. The flow chart of the optimization study is shown in Fig. 3.3.

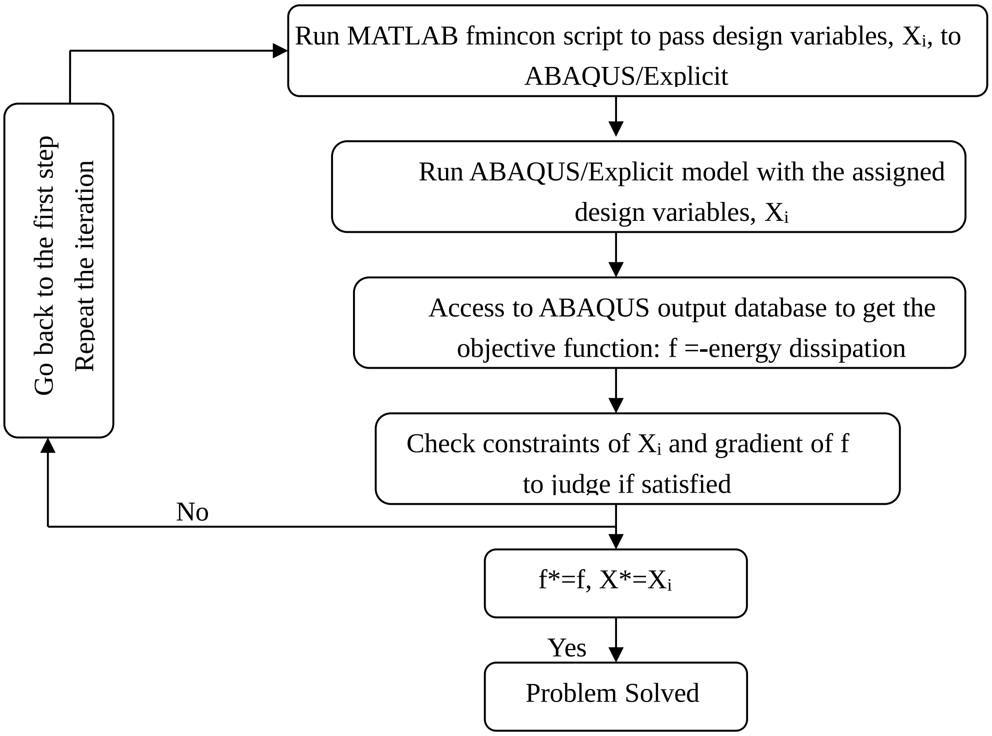

Figure 3.3 Schematic representation of the optimization process

3.3 Results

3.3.1 Verification of Material Model for Impact Testing Simulation

The material model for PC was tested in a single element subjected to uniaxial compressive load at low and high strain rates. The stress-strain relationships from the simulations were compared to the experimental results in the literature [16]. The plots are shown in Fig. 3.4. Due to the lack of experimental data for the strain rate of -5 s^{-1}, the experimental result at the strain rate of -1 s^{-1} was used as reference data for the FEM result at -5 s^{-1}. The comparisons show that the material model could predict the pressure and strain rate dependent behavior of PC with acceptable accuracy.

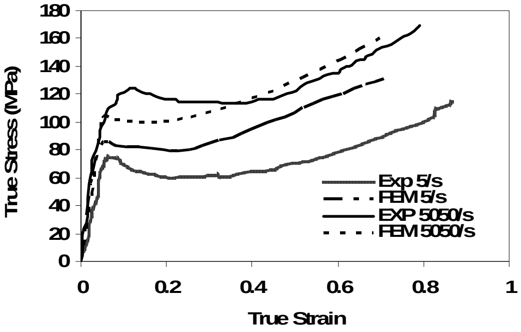

Figure 3.4 Comparisons of the numerically predicted uniaxial stress-strain curves (compression) of PC to the experimental measurements.

The stress-strain relationship predicted by the material mode at different strain rates was used as the material model input for PC in the impact testing simulations. The simulation results of monolithic PC and PMMA subjected to low velocities are compared to the ones from the low velocity impact testing [36] (Fig. 3.5). The FEM simulations of low velocity impact testing have a good agreement with the experimental results. There are no force and energy curves for high velocity impact testing available in the existing literature. Sarva [24] measured the fraction of residual and initial kinetic energy of monolithic PC plate and 6-layered laminate PC and PMMA plate with a dimension of 100x100 mm and thickness of 6.35 mm subjected to impact velocities of 300-500 m/s. Thus, the FEM simulations referred to the experimental results from Sarva as baseline results. The FEM simulation results and discussion are shown in section 3.3.3.

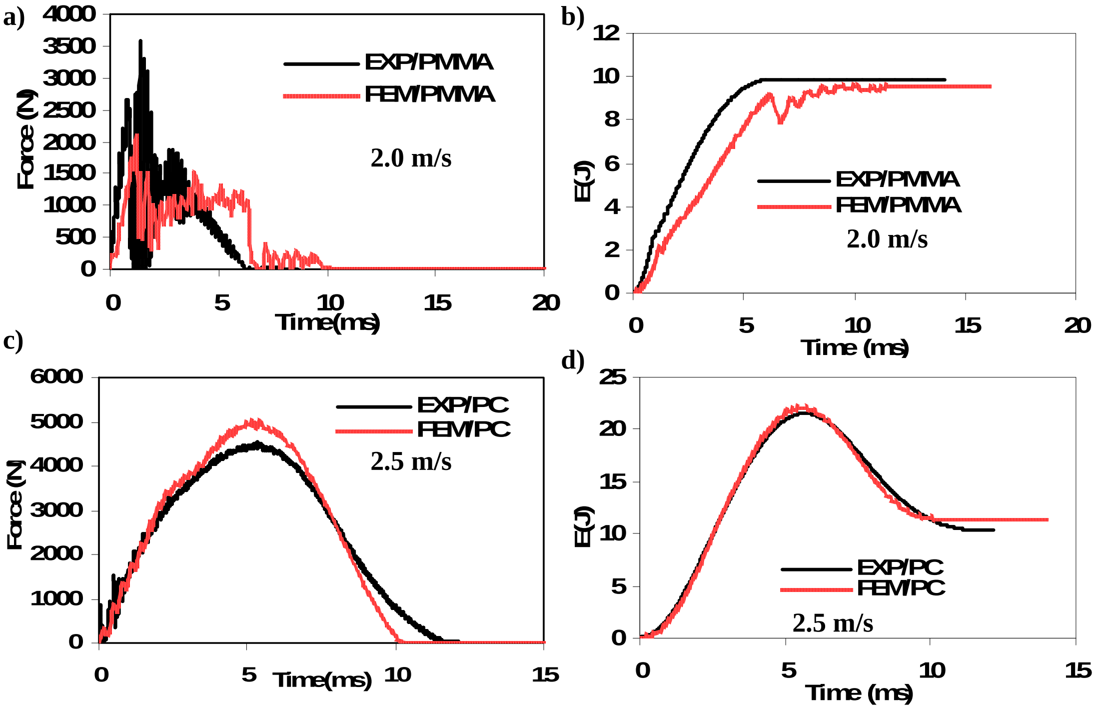

Figure 3.5 Comparisons of FEM low velocity impact simulation results to experimental results: a) Reaction force vs. time for monolithic PMMA subjected to impact velocity of 2.0 m/s; b) Impact energy vs. time for monolithic PMMA subjected to impact velocity of 2.0 m/s; c) Reaction force vs. time for monolithic PC subjected to impact velocity of 2.5 m/s; d) Impact energy vs. time for monolithic PC subjected to impact velocity of 2.5 m/s.

3.3.2 FEM of Low Velocity Impact Test

The kinetic energy history and various types of energy dissipation of layered PMMA and PC laminate panel and monolithic PC subjected to impact velocity of 5m/s by a spherical projectile with radius of 6.35 mm are shown in Fig. 3.6. The results showed that monolithic PC was beneficial to the low velocity impact testing with an aspect ratio (a ratio of the diameter of projectile to the diameter of the plate) of 0.167. The energy dissipated by a monolithic PC was about 1.58 times higher than 8-layered PMM/PC laminate (Fig. 3.6). The impact event of monolithic PC was dominated by plastic dissipation. However, strain energy was the major form of energy dissipation for brittle PMMA. The results showed that although the strain energy dissipated by the layered laminate increased from 0.4 J to 5.4 J compared to monolithic PC, the total energy dissipated actually decreased because the plastic energy dissipated decreased from 42.1 J to 19.9 J.

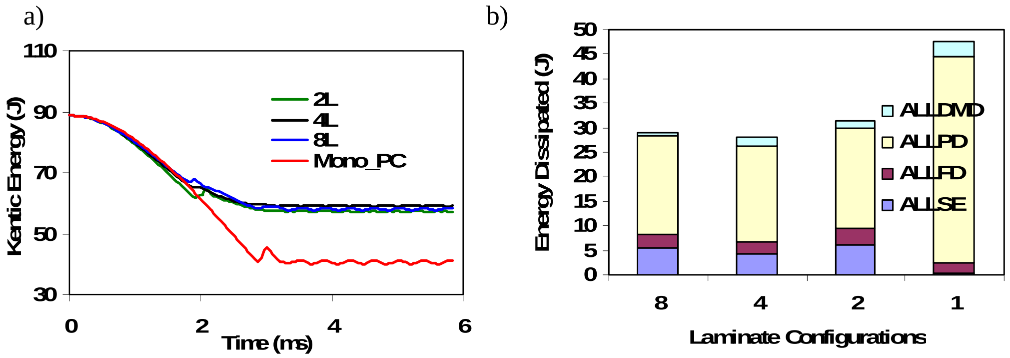

Figure 3.6 FEM results of layered PMMA/PC laminate panel and monolithic PC subjected to impact velocity of 5 m/s by a spherical projectile with radius of 6.35 mm: a) Kinetic energy vs. time; b) Distribution of various energies dissipated calculated by ABAQUS/EXPLICIT. Note: ALLSE, strain energy; ALLFD, fiction dissipation; ALLPD, plastic dissipation; ALLDMD, damage dissipation.

The stress contours of half plates of the 8-layered PMMA/PC laminate, monolithic PC, and monolithic PMMA at different time frames are shown in Fig. 3.7. It was shown that the crack in the monolithic PMMA first initiated on the back of the plate and then propagated radially. In total, 4 radial cracks were formed and this has a good agreement with the experimental observations [36]. As expected, the deformation of monolithic PC was dominated by local plastic deformation. The 8-layered PMMA/PC laminate mitigated the radial cracking in the PMMA layers, but the plastic deformation in the PC layers was not magnified.

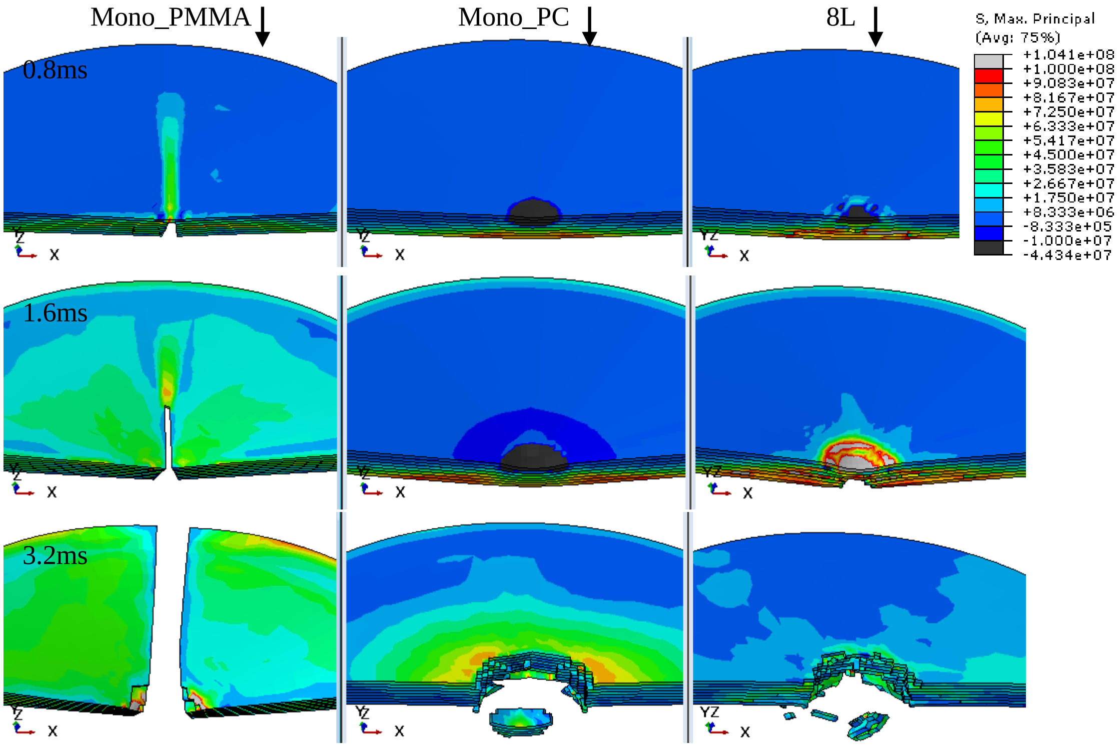

Figure 3.7 Stress contours of 8-layered PMMA/PC laminate, monolithic PC, and monolithic PMMA subjected to impact velocity of 5 m/s by a spherical projectile with radius of 6.35 mm at different time frames.

3.3.3 FEM of High Velocity Impact Test

The kinetic energy history and various types of energy dissipation of layered PMMA and PC laminate panel and monolithic PC subjected to impact velocity of 300 m/s by a blunt projectile with a radius of 2.73 mm are shown in Fig. 3.8. The results showed that the energy dissipated by a 8-layered PMMA/PC laminate increased 5 percent more than the monolithic PC. The amount of energy dissipated in different forms including strain energy, plastic dissipation, friction dissipation, and damage dissipation calculated by ABAQUS/EXPLICIT are shown in Fig. 3.8b. It can be seen that although the volume fraction of PC deceased from 1 to 0.5 in 8-layered PMMA/PC laminate compared to the monolithic PC, the plastic dissipation only deceased about 24 percent. These results indicated that the PMMA layer enhanced the PC layer by amplifying the local plastic deformation of PC. Compared to monolithic PC, the strain energy, friction dissipation in the 8-layered PMMA/PC laminate increased from 1.7 J to 10.4 J and 3.9 J to 5.6 J respectively. Compared to the experimental results shown by Sarva [24], although the total energy dissipation predicted by the simulations did not match (lower than experimental measurements), the computational trend that layered PMMA/PC laminate improving the energy dissipation appeared to match the experimental trend.

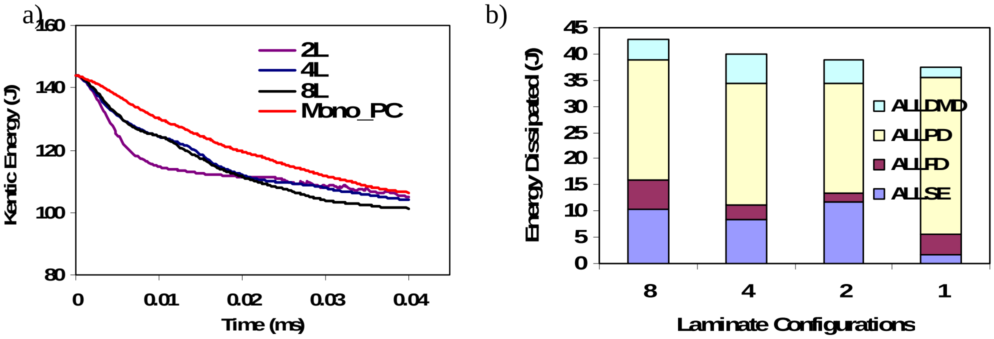

Figure 3.8 FEM results of layered PMMA/PC laminate panel and monolithic PC subjected to impact velocity of 300 m/s by a blunt projectile with radius of 2.73 mm : a) Kinetic energy vs. time; b) Distribution of various energies dissipated calculated by ABAQUS/Explicit.

The stress contours of the half plates of the 8-layered PMMA/PC laminate, monolithic PC, and monolithic PMMA at different time frames are shown in Fig. 3.9. The simulation contour showed that the failure of monolithic PMMA was dominated by brittle cracking. Many spalls were observed on the back surface of the immediate impact region. The failure mechanism of PMMA has a good agreement with the experimental observation shown by Sarva [24]. The deformation of monolithic PC was dominated by local plastic deformation, which occurred in the immediate impact zone under the projectile. Stress contour of the 8-layered PMMA/PC laminate showed that the laminate structures magnified the plastic deformation zone and decreased the brittle damage area.

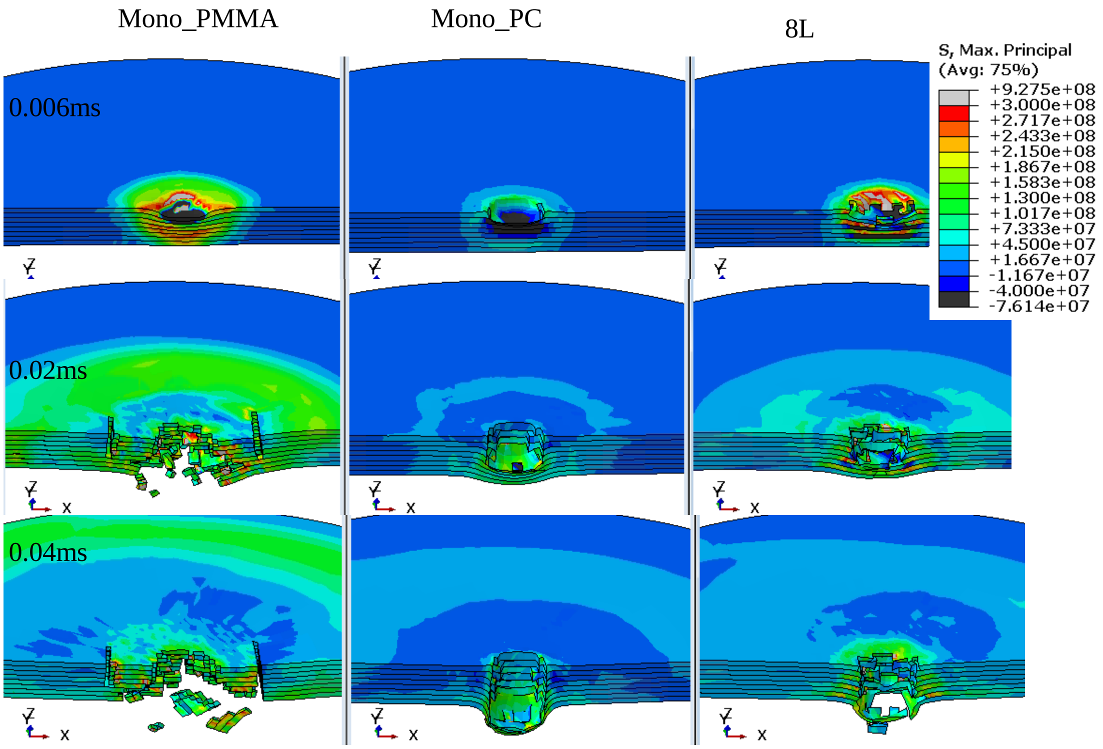

Figure 3.9 Stress contours of 8-layered PMMA/PC laminate, monolithic PC, and monolithic PMMA subjected to an impact velocity of 300 m/s by a blunt projectile with radius of 2.73 at different time frames.

3.3.4 Optimal Design of Laminate Panel Subjected to Impact Test

The study in the previous two sections showed that the 8-layer laminate PMMA and PC panel subjected to high velocity impact with a smaller projectile has more benefits than the low velocity impact with a larger projectile. Thus, to evaluate the effect of aspect ratios on the impact behavior of the PMMA and PC laminate more simulations with different aspect ratios were conducted. The fraction of kinetic energy versus various aspect ratios of the monolithic PC and 8-layer laminate subjected to the impact velocities of 5 m/s and 300 m/s are plotted in Fig. 3.10. For both of the monolithic PC and PMMA, the fraction of kinetic energy decreased with aspect ratio. When the aspect ratio decreased to about 0.07, both the high and low velocity showed that the 8-layered laminate panel started to dissipate more energy than the monolithic PC.

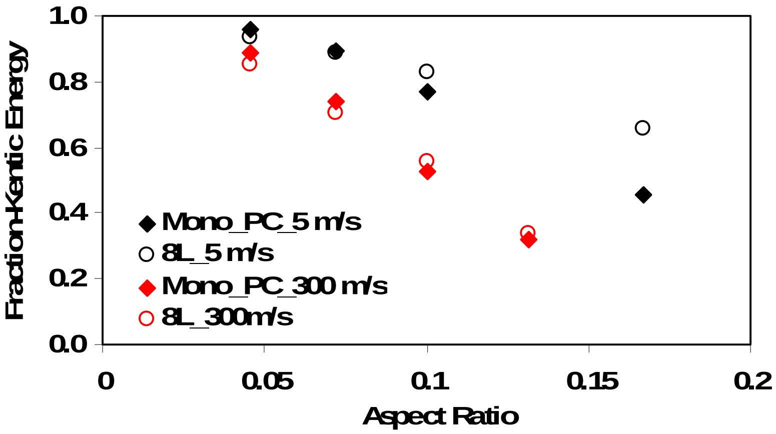

Figure 3.10 Fraction of kinetic energy of 8 layers of PMMA and PC laminate panel subjected to impact velocity of 300 m/s by a blunt projectile with radius of 1.73-5 mm and impact velocity of 5 m/s by a spherical projectile with radius of 6.35-1.73 mm.

Non-linear optimization of the energy dissipation capacity of 8-layered PMMA/PC laminate were conducted by use of MATLAB optimization tool box, fmincon. The residual kinetic energy of the laminate system was minimized in terms of two variables: one is the multiplier of post-yielding stresses of PC at impact speed of 300 m/s within the range of 0.5 to 2.0 (Case 1); another is multiplier of stress at failure of PMMA at impact speed of 300 m/s within the range of 0.6 to 1.4 (Case 2). The iteration processes of the two optimization cases are shown in Fig. 3.11. For both of the cases, the residual kinetic energy has a negative correlation with the multipliers. For case 1, it took 6 iterations to seek the minimum residual kinetic energy with a value of 84.6 J at a multiplier of 1.99, which yields to a post yielding stress of PC 182.5 MPa. For Case 2, it took 16 iterations to seek the minimum residual kinetic energy with a value of 98.2 J at a multiplier of 1.38, which yields to a failure stress of PMMA 351 MPa.

To evaluate the joint effects of the above two variables on the energy dissipation capacity of 8-layered PMMA/PC laminate, an optimization was also performed by use of both two multipliers as variables to minimize the residual kinetic energy of the laminate system subjected to impact velocity of 300 m/s. The corresponding optimization iteration process is shown in Fig. 3.12. The

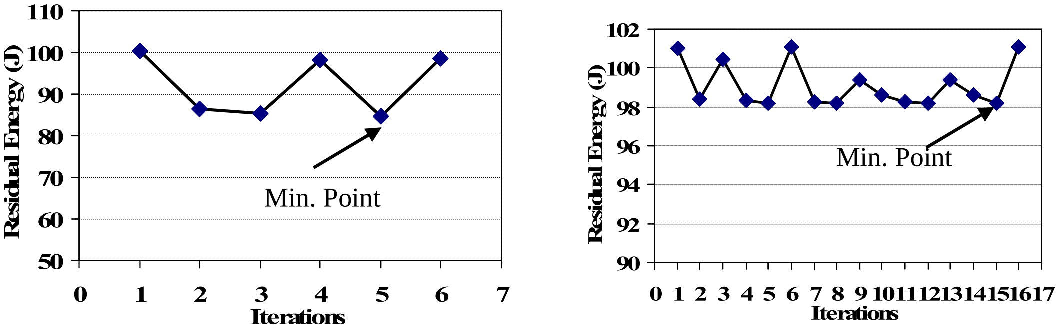

Figure 3.11 Non-linear optimization of residual kinetic energy of 8-layered PMMA/PC laminate subjected to impact velocity of 300 m/s by a blunt projectile with radius of 2.73 mm: a) multiplier of yielding stress of PC as variable; b) multiplier of stress at failure of PMMA as variable.

optimization showed that the objective function was oscillating at a value of 84 J with both of the two multipliers oscillating at their upper bound at the end of the iteration.

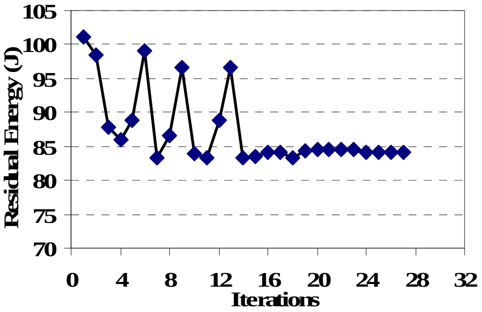

Figure 3.12 Non-linear optimization of residual kinetic energy of 8-layered PMMA/PC laminate subjected to impact velocity of 300 m/s by a blunt projectile with radius of 2.73 mm in terms of two variables: multiplier of yielding stress of PC and multiplier of stress at failure of PMMA.

3.4 Discussion

At a low strain rate ($\leq 1\ s^{-1}$), the stress-strain relationships of PMMA and PC follow a similar trend (Figure 1): linear elastic, strain rate dependent yielding, strain softening, and strain hardening. With the increase of strain rate, PMMA starts to show its brittle nature with a different stress-strain response: linearly increasing to a high peak stress, a steep softening, and failure. Due to these different material characteristics, PMMA and PC exhibit different failure behavior under impact loading: the failure of PMMA is governed by brittle cracking and the failure of PC is governed by plastic deformation. Thus, plastic and brittle material models were used to simulate the impact performance of PMMA and PC respectively by ABAQUS/EXPLICIT. In conjunction with damage initiation and evolution material failure model, the rate and pressure dependent stress-strain curves of PC predicted by Arruda and Boyces three-dimensional physical-based models [9] was used as the material inputs of ABAQUS/EXPLICIT to predict the impact behavior of PC plates subjected to low (5 m/s) and high speed (300 m/s) impact loading. The material model of brittle cracking of ABAQUS/EXPLICIT was used to simulate the brittle failure behavior of PMMA subjected to impact loading.

It was found that at the impact conditions of the aspect ratio of 0.17, impact speed of 5 m/s, and impact mass of 7.1 kg, 8-layered PMMA/PC did not show benefits over the monolithic PC in terms of energy dissipation. However, in the same impact conditions, with the decrease of the aspect ratio to a critical value, 0.07, the 8-layered PMMA/PC started to dissipate more energy than the monolithic PC. The same phenomena was observed in the high speed impact simulations with a impact mass of 0.0032 kg and impact speed of 300 m/s. When the aspect ratio was small, the deformation of the PC plate was governed with local plastic deformation. However, in the layered PMMA/PC laminate, the hard PMMA layers severed as back plates to support the ductile PC layers, and the ductile PC layers served as barriers to prevent the large crack of PMMA coalescing to lead to a catastrophic failure. Thus, at small aspect ratios, the layered PMMA/PC laminate has an improved impact resistance compared to the monolithic PC. With the increase of aspect ratios, the benefits of the laminate structure tended to disappear. The reason was that the failure mechanism of PMMA and PC is different when it was impacted with small and large aspect ratios. As shown in Fig. 3.9, the failure of the PMMA plates was governed with brittle spall-induced damage at small aspect ratios. However, at large aspect ratios (Fig. 3.7), a large scale of radial damage was formed at the bottom surface of the plate due to the high bending force induced by the big projectile. For the PC plate, with the increase of aspect ratio, more areas (the immediate impact zone under the projectile) were involved in the plastic deformation. Thus, the role of PMMA plates in magnifying the plastic damage zone was not significant.

For the purpose of developing a hybrid ductile/brittle transparent laminate that could stand a wide range of impact loading, an optimization of 8-layered PMMA/PC laminate was conducted. The residual kinetic energy was shown to have a negative correlation with the post yielding stress of PMMA and PC. With an increase in post yielding stress of PMMA from 254 MPa to 351 MPa, the energy dissipated only increased 2.8 J. Relatively, with an increase in the post yielding stress of PC from 91.7 MPa to 182.3 MPa, the energy dissipated increased 17.2 J. Thus, it seemed that the impact resistance of 8-layered PMMA/PC laminate is more sensitive to the strain rate hardening of PC.

3.5 Conclusion

The failure behavior of monolithic PMMA and PC and layered PMMA/PC laminate subjected to low and high speed impact loading were numerically investigated. Boyces three-dimensional physical-based models [9] were implemented in ABAQUS to predict the strain rate and pressure dependent behavior of PC. The failure mechanism, fragmentation pattern, and energy dissipation were compared through the simulations. The failure of monolithic PMMA was dominated by brittle cracking. Many spalls were observed on the back surface of the immediate impact region at small aspect ratio. The deformation of monolithic PC was dominated by local plastic deformation which occurred in the immediate impact zone under the projectile. For both of the monolithic PC and layered PMMA/PC laminate, the fraction of kinetic energy decreased with aspect ratio. There is found to exist a critical aspect ratio, 0.07 for both the high velocity impact (300 m/s) and low velocity impact (5 m/s). When the aspect ratio decreased below this critical value, the 8-layered laminate started to dissipate more energy than the monolithic PC. The 8-layered PMMA/PC laminate magnified the plastic deformation zone and decreased the brittle damage area. An optimal study by incorporating MATLAB optimization tool box and ABAQUS FEM simulations was conducted to maximize the impact resistance of the transparent laminated panel. It was found that the impact resistance or the overall ballistic performance of these PMMA/PC laminated systems is relatively more sensitive to strain rate hardening of PC than PMMA.

REFERENCES

REFERENCES

[1] Alex J Hsieh, Daniel DeSchepper, Paul Moy, Peter G Dehmer, and John W Song. The effects of pmma on ballistic impact performance of hybrid hard/ductile all-plastic-and glass-plastic-based composites. Technical report, DTIC Document, 2004.

[2] Alex J Hsieh and John W Song. Measurements of ballistic impact response of novel co-extruded pc/pmma multilayered-composites. *Journal of reinforced plastics and composites*, 20(3):239–254, 2001.

[3] Parimal J Patel, Gary A Gilde, Peter G Dehmer, and James W McCauley. Transparent ceramics for armor and em window applications. In *International Symposium on Optical Science and Technology*, pages 1–14. International Society for Optics and Photonics, 2000.

[4] S Sahraoui and JL Lataillade. Deformation and fracture of pmma at high rates of loading. *Journal of applied polymer science*, 51(9):1527–1532, 1994.

[5] SC Wright, NA Fleck, and WJ Stronge. Ballistic impact of polycarbonatean experimental investigation. *International journal of impact engineering*, 13(1):1–20, 1993.

[6] Ravi Shankar Kalluri. *Failure of transparent polymer composite laminated glass panels under impact loading*. PhD thesis, University of Missouri–Columbia, 2007.

[7] Qasim H Shah. Impact resistance of a rectangular polycarbonate armor plate subjected to single and multiple impacts. *International Journal of Impact Engineering*, 36(9):1128–1135, 2009.

[8] Xin Sun, Kevin C Lai, Tara Gorsich, and Douglas W Templeton. Optimizing transparent armor design subject to projectile impact conditions. *Advances in Ceramic Armor IV: Ceramic Engineering and Science Proceedings, Volume 29, Issue 6*, pages 15–22, 2008.

[9] Ellen M Arruda and Mary C Boyce. Evolution of plastic anisotropy in amorphous polymers during finite straining. *International Journal of Plasticity*, 9(6):697–720, 1993.

[10] C Bauwens-Crowet. The compression yield behaviour of polymethyl methacrylate over a wide range of temperatures and strain-rates. *Journal of Materials Science*, 8(7):968–979, 1973.

[11] C Bauwens-Crowet, J-C Bauwens, and Georges Homes. The temperature dependence of yield of polycarbonate in uniaxial compression and tensile tests. *Journal of Materials Science*, 7(2):176–183, 1972.

[12] MC Boyce and EM Arruda. An experimental and anaiytical investigation of the large strain compressive and tensile response of glassy polymers. *Polymer Engineering & Science*, 30(20):1288–1298, 1990.

[13] Mary C Boyce, Ellen M Arruda, and R Jayachandran. The large strain compression, tension, and simple shear of polycarbonate. *Polymer Engineering & Science*, 34(9):716–725, 1994.

[14] F Rietsch and B Bouette. The compression yield behaviour of polycarbonate over a wide range of strain rates and temperatures. *European Polymer Journal*, 26(10):1071–1075, 1990.

[15] AS Argon. A theory for the low-temperature plastic deformation of glassy polymers. *Philosophical Magazine*, 28(4):839–865, 1973.

[16] AD Mulliken and MC Boyce. Mechanics of the rate-dependent elastic–plastic deformation of glassy polymers from low to high strain rates. *International journal of solids and structures*, 43(5):1331–1356, 2006.

[17] Herzl Chai and Guruswami Ravichandran. On the mechanics of fracture in monoliths and multilayers from low-velocity impact by sharp or blunt-tip projectiles. *International journal of impact engineering*, 36(3):375–385, 2009.

[18] Md Akil Hazizan and WJ Cantwell. The low velocity impact response of foam-based sandwich structures. *Composites Part B: Engineering*, 33(3):193–204, 2002.

[19] Yanxiong Liu and Benjamin Liaw. Drop-weight impact tests and finite element modeling of cast acrylic/aluminum plates. *Polymer Testing*, 28(8):808–823, 2009.

[20] JD Pearson, MA Zikry, M Prabhugoud, and K Peters. Measurement of low velocity and quasi-static failure modes in pmma. *Polymer composites*, 28(3):381–391, 2007.

[21] Joshua S Stenzler and NC Goulbourne. The effect of polyacrylate microstructure on the impact response of pmma/pc multi-laminates. *International Journal of Impact Engineering*, 38(7):567–576, 2011.

[22] JW McCauley, E Strassburger, P Patel, B Paliwal, and KT Ramesh. Experimental observations on dynamic response of selected transparent armor materials. *Experimental Mechanics*, 53(1):3–29, 2013.

[23] Shinji Ogihara, Tomoyuki Ishigure, and Akira Kobayashi. Study on impact perforation fracture mechanism in pmma. *Journal of materials science letters*, 17(8):691–692, 1998.

[24] S Sarva, AD Mulliken, and MC Boyce. The mechanics of large-strain inhomogeneous deformation of polymeric materials under dynamic loading conditions. In *Journal de Physique IV (Proceedings)*, volume 134, pages 95–101. EDP sciences, 2006.

[25] L Roy Xu and Ares J Rosakis. An experimental study of impact-induced failure events in homogeneous layered materials using dynamic photoelasticity and high-speed photography. *Optics and Lasers in Engineering*, 40(4):263–288, 2003.

[26] Michael Hebert, Carl-Ernst Rousseau, and Arun Shukla. Shock loading and drop weight impact response of glass reinforced polymer composites. *Composite Structures*, 84(3):199–208, 2008.

[27] Srinivasan Arjun Tekalur, Arun Shukla, and Kunigal Shivakumar. Blast resistance of polyurea based layered composite materials. *Composite Structures*, 84(3):271–281, 2008.

[28] A Shokuhfar, SMR Khalili, F Ashenai Ghasemi, K Malekzadeh, and S Raissi. Analysis and optimization of smart hybrid composite plates subjected to low-velocity impact using the response surface methodology (rsm). *Thin-Walled Structures*, 46(11):1204–1212, 2008.

[29] AN Shupikov, SV Ugrimov, AV Kolodiazhny, and VG Yareschenko. High-order theory of multilayer plates. the impact problem. *International journal of solids and structures*, 35(25):3391–3403, 1998.

[30] NV Smetankina, S Yu Sotrikhin, and AN Shupikov. Theoretical and experimental investigation of vibration of multilayer plates under the action of impulse and impact loads. *International journal of solids and structures*, 32(8):1247–1258, 1995.

[31] X Chen, N Chandra, and AM Rajendran. Analytical solution to the plate impact problem of layered heterogeneous material systems. *International journal of solids and structures*, 41(16):4635–4659, 2004.

[32] Mahmoud M Reda Taha, Arife B Colak-Altunc, and Marwan Al-Haik. A multi-objective optimization approach for design of blast-resistant composite laminates using carbon nanotubes. *Composites Part B: Engineering*, 40(6):522–529, 2009.

[33] TY Kam and FM Lai. Maximum stiffness design of laminated composite plates via a constrained global optimization approach. *Composite structures*, 32(1):391–398, 1995.

[34] MC Ray and A Baz. Optimization of energy dissipation of active constrained layer damping treatments of plates. *Journal of Sound and Vibration*, 208(3):391–406, 1997.

[35] RN Haward and G Thackray. The use of a mathematical model to describe isothermal stress-strain curves in glassy thermoplastics. *Proceedings of the Royal Society of London. Series A. Mathematical and Physical Sciences*, 302(1471):453–472, 1968.

[36] Wei Zhang, Srinivasan Arjun Tekalur, and L Huynh. Impact behavior and dynamic failure of pmma and pc plates. In *Dynamic Behavior of Materials, Volume 1*, pages 93–104. Springer, 2011.

Chapter 4

The Effects of Damage Accumulation on Tensile Strength and Toughness of Compact Bovine Bone subjected to Static Tensile Loading, Charpy Impact Loading, and SHPB High Strain Rate Tensile Loading

4.1 The Effects of Damage Accumulation on Tensile Strength and the Toughness of Compact Bovine Bone subjected to Static Tensile Loading

4.1.1 Introduction

As a tough and light-weight natural composite, bone works as a scaffold to provide support and protection to internal organs. Understanding the failure mechanisms in bone is of great medical interest for preventing bone fracture failure and improving bone fracture treatment. Bone fractures are a result of tensile failure subsequent to bending or torsion because bone is more susceptible to tensile failure compared to compressive failure[1, 2, 3, 4]. Bone is a strain rate dependent material due to its viscoelastic properties where increases in loading rate have resulted in increases in Young's modulus and ultimate stress [5, 6, 7, 8, 9, 10, 11]. The mechanical properties of compact bone are also related to its hierarchical microstructure. The strength, energy absorption, and modulus of elasticity decrease with the percentage area of osteons [11, 12, 8, 13, 14]. Interestingly, little emphasis has been placed on the role of microcracking on the tensile failure behavior of bone although, like quasi-brittle materials, the failure of bone is characterized as the result of damage accumulation in the form of microcracks.

Microcrack accumulation has been shown to yield a loss of stiffness in compact bone under cyclic fatigue testing [15, 16]. Microcracking was also found to be a primary toughening mechanism that resulted in increased R-curve behavior [17, 18, 19, 20] applied a series of fluorescent chelating agents to monitor the crack growth during cyclic compression fatigue finding that microcracking initiated in the interstitial bone tissue in the early stage of the fatigue life and that longer microcracks developed in the longitudinal direction as opposed to the transverse direction. In recent efforts, Zioupos [21] examined the plastic strain of compact canine femurs, subjected to tensile loading at various strain rates, to the number of cracks (imaged by staining), concluding that the plastic strain had a positive correlation with the number of cracks. However, each of the above studies was limited by the resolution limits imposed by Frost's [22] bulk fuchsin staining technique, which requires the tested specimens to be cut into microsections. Sectioning can introduce new microcracks during cutting; and, furthermore, the small field of view compromises the accuracy of the crack length measurement. Several attempts have been made to avoid these limitations. Zioupus [23] used the acoustic emission method to monitor crack growth in bone and antler specimens under uniaxial tensile loading where microcracks were found to initiate upon yielding in both antler and bovine tibia specimens. However, the shortcoming of the technique is that the growth and distribution of microcracks cannot be directly visualized. Using the laser illumination technique, Reilly [24] found that the microcracks developed on the tensile side of bone specimens subjected to four-point bending. These tensile microcracks first appeared at a strain of 0.004 and the peak growth of the microcracks occurred when the strain reached 0.008. However, due to the step loading and examination, the stress-strain curve was not continuously obtained throughout the test.

In the present dissertation, an innovative optical technique was used to monitor the damage accumulation during the process of tensile failure of compact bovine femur. A high speed camera and a LED panel were set up to record the light illumination of the microcracks initiated and propagating on the specimen surface when stretched under a multipurpose tensile testing system (MTS). By using the strong light scattering effects of crack edges, microcracks are visible as features with higher light intensity. To evaluate the correlation between the developing microcracks and the bone microstructure, specimens from several bovine femurs of different ages were examined. Strain rate effects were also investigated by examining 10 specimens from one piece of bovine femur with strain rates ranging from 0.0001 to 0.012 s^{-1}. As a natural composite material, the mechanical properties of bone depend on the fiber or osteon direction, which runs along the loading axis of bone. It has been shown that osteons potentially act as barriers to prevent coalescence of the microcracks initiated in the interstitial bone tissue [25, 26]. Thus, the failure pattern of bone loaded in the transverse (perpendicular to the osteon direction) and the longitudinal direction (along osteon direction) are expected to be different. To evaluate such orientation effects, the compact bovine specimens machined from one piece of bovine femur bone were loaded in the longitudinal and transverse directions respectively. The stress-strain curves were correlated to the high-speed images to examine the microcrack growth in the specimens. Post-failure examinations were performed with a scanning electron microscope (SEM). Both the front flat surface and the fracture surface were examined.

4.1.2 Material and Methods

The tensile specimens were machined from fresh compact femurs (12 to 30 months old) provided by a local beef abattoir. The mid-diaphysis of the bovine femur was first cut into rough rectangular beams using a band saw. Then, the beams were machined into 60x8x2 mm (longitude) or 30x8x2 mm (transverse) rectangular shapes using a milling machine (ProCut RL80RF311) at a low feed speed. Subsequently, a Dremel hand tool was used to shape the rectangular beams into the dog-bone shape specimens with the exact same geometry. Finally, the specimens were manually polished with 80, 100, 600, 1000 grit. During the entire machining process, the specimens were kept wet with the phosphate buffered saline (PBS) solution. The geometry and dimensions are shown in Fig. 4.1. After machining, the specimens were covered with gauze dipped in PBS solution and preserved in a -20°C freezer until testing. Specimens were thawed just prior to testing. Overall, 28 specimens were machined, including 12 specimens from one femur (30-months old) for strain rate effects, 10 specimens from several femurs with various ages (12 to 30 months old) for microstructure effects, and 6 specimens from one femur (30-months old) to examine orientation effects.

Uniaxial tensile testing was performed using a MTS Insight tensile testing system with a 10 kN load cell. A high speed camera (Phantom V12) was set facing the front side of the specimen to record the fracture process. In order to visualize the microcracks, the tests were performed in a dark room and a strong cold light source was set at the side of the camera to illuminate the specimen. A laser extensometer (EIR Model LE-05) was set up facing the back side of the specimen to measure the extension. Both the high speed camera and the laser extensometer were triggered at the same time as the MTS started to apply the load. The rationale of the research approach is not directed

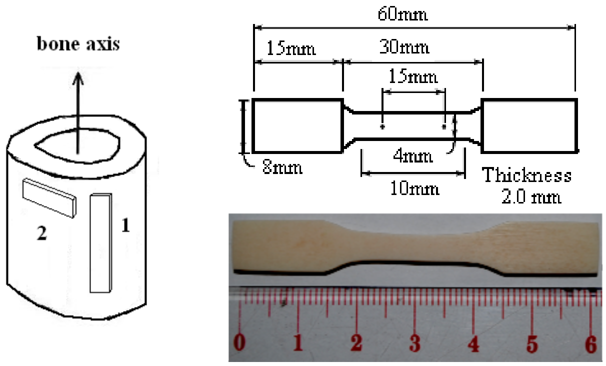

Figure 4.1 Geometry and dimensions of dog-bone specimens. (a), specimen orientation diagram (1, longitudinal specimens, loaded along the osteon direction; 2, transverse specimens, loaded perpendicular to the osteon direction); (b), the dimension of the longitudinal specimens (the length of the transverse specimens is half of the longitudinal specimens)

to quantify the exact amount of microcracking in bone but rather indirectly provide a ”real-time” relationship between microcracking and strain development. It is proposed that there exist critical strain rate and strain levels to initiate and propagate microcracking in bone. It has never been clearly shown what these levels are. More importantly, the orientation of bone and the osteon size affects initiation and propagation of microcracking. The experimental design is geared to bring out these effects. Since we indirectly correlated microcracking by the diffuse light pattern, questions might arise on the validity of using the light intensity as a measure of microcracking. It is true that many materials exhibit a change in color or appearance while subjected to loading (e.g., crazing in polymers). But it is different in the case of bone where the change in light intensity is directly related to microcracking. Validation for the current is provided by Zioupos et al. [21]and in our experimental measurements themselves where the light diffusion gradually increases as the load is applied and reaches peak value at peak load (Fig. 4.2). Exact quantification of light intensity to density of microcracking could be undertaken but again is not the primary focus of the current work.

The specimens were covered with sterile PBS soaked gauze before testing, where the duration

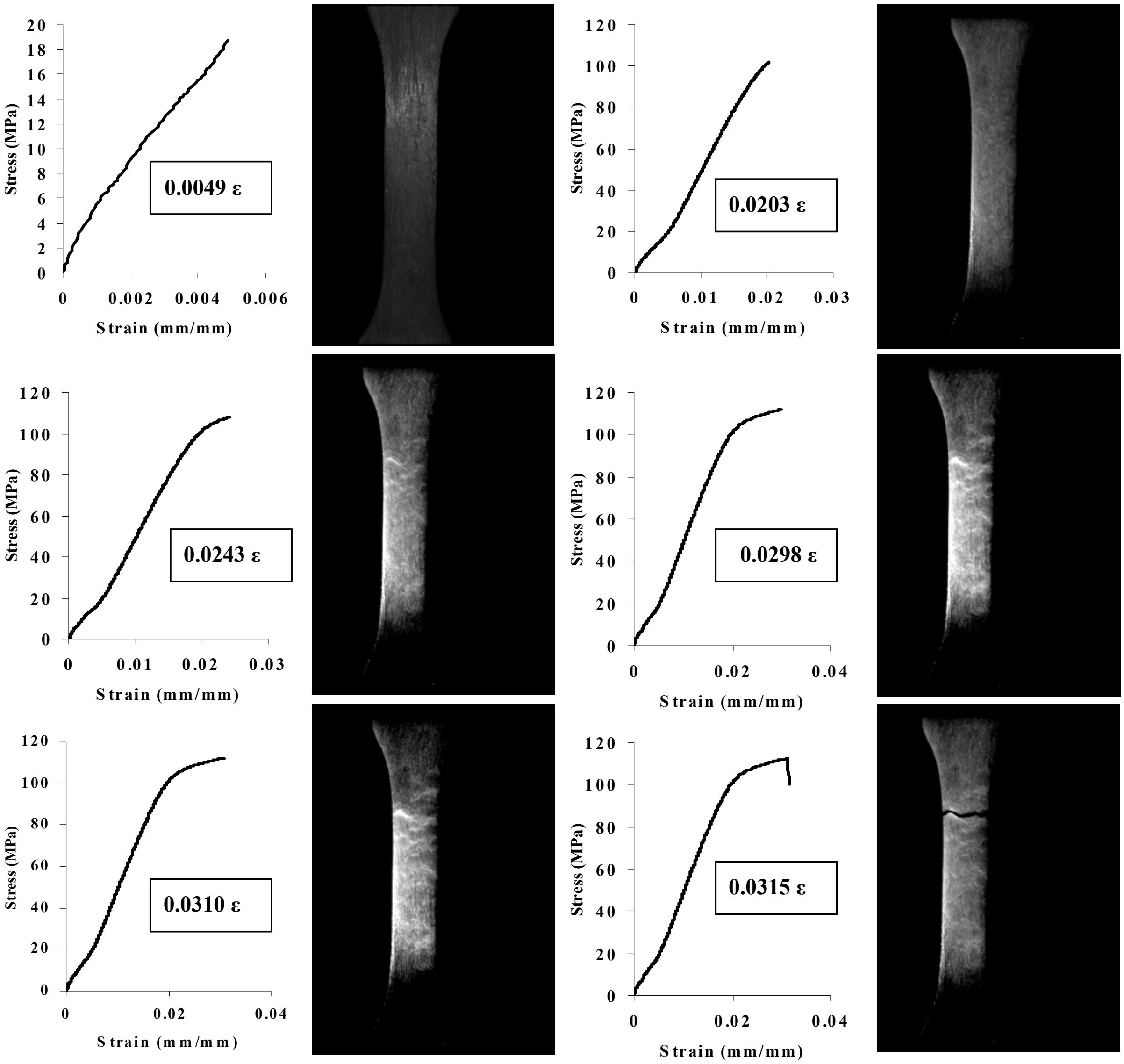

Figure 4.2 Representative images showing real time optical effects during tensile stretching of bovine bone sample. The frame rate of this is 1000 fps.

of the test lasted about one minute. Thus, the specimens were considered wet. For the strain rate evaluation, the cross-head speeds ranged from 0.5 mm/min to 10 mm/min corresponding to strain rates of 0.0001 to 0.0012 s^{-1}. All other tests were performed at a cross-head speed of 0.5 mm/min. The frame rates of the high speed camera were 200 s^{-1}, 800 s^{-1}, and 1500 s^{-1} for tests with cross-head speeds of 0.5 mm/min, 1 to 2 mm/min, and larger than 3 mm/min, respectively.

Images from the camera were used to calculate the light intensity in each frame by a MATLAB code. The light intensity was represented by the normalized gray scale value in each frame, which was calculated by summarizing the gray scale value of each pixel in each frame after subtracting the corresponding value in the reference frame and then normalizing by the numbers of pixel in the frame.

The post-failure fracture damage of the tested specimens was examined in a JEOL JSM-6400V (lanthanum hexaboride electron emitter) scanning electron microscope. Digital images were acquired using analySIS Pro software version 3.2 (Olympus Soft Imaging Solution Corp., Munster, Germany). Before the examination, samples were coated with gold (20 nm thickness) in an Emscope Sputter Coater model SC 500 (Ashford, Kent, England) purged with argon gas. Samples were mounted on aluminum stubs using high vacuum carbon tab.

4.1.3 Experimental Results

4.1.3.1 Imaging Longitudinal Specimens Loaded in the Same Strain Rate of 0.0001 s^{-1}

A higher light intensity was expected when the microcracks initial 0.0001 s^{-1}ted on the specimen surface due to the light scattering effect of the crack edges. High speed grayscale images extracted from the high speed videos were correlated to the stress-strain curves. The microcrack illumination of two typical specimens, one with dispersed microcracks and one with coalesced microcracks, are shown in Fig. 4.3a, b, respectively. It was found that microcrack illumination began to occur at yielding and the specimens with dispersed microcracks developed a larger plastic strain as compared to the specimen with local cracks, which lead to quick failure after yielding. The yielding point was determined by Currey's [7] method, which is the intersection of the tangents of the linear portion and the post-yield portion of the stress-strain curve. The changing in the light intensity with time was calculated for each specimen. The plots of light intensity and stress over time for the two typical specimens (Fig. 4.3a, b) are shown in Fig. 4.3c, d. The calculated results agreed with the visual observation from the images that, for both of these two specimens, the significant increases in light intensity occurred at onset of yielding. After initiation, light intensity gradually increased with time until failure. The specimen with a larger plastic strain (typically 2.0%) developed more microcracks leading to a higher microcracking illumination compared to the specimen with a smaller plastic strain (typically 0.5%).

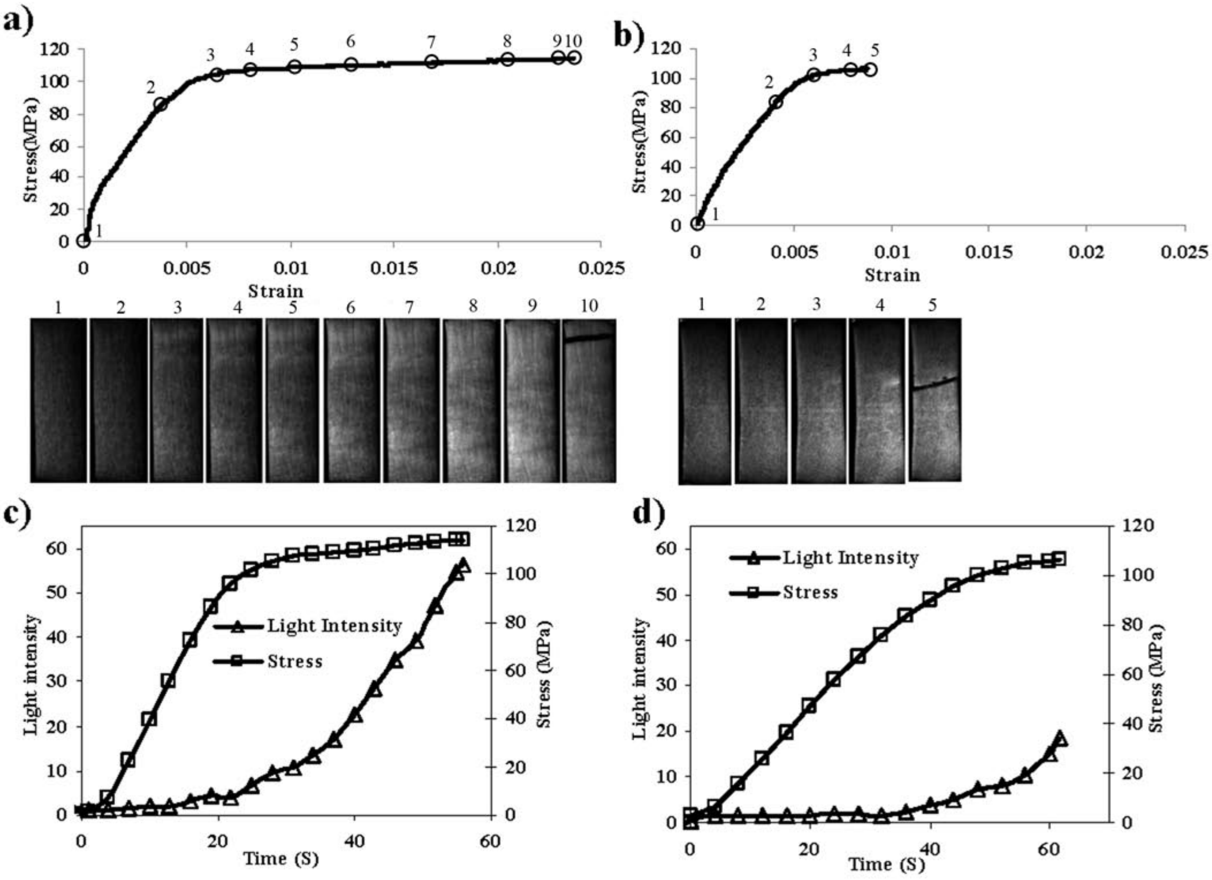

Figure 4.3 Correlations of high speed images with stress-strain curves for two typical longitudinal compact bovine femur specimens tested under a constant strain rate of 0.0001 s^{-1}: (a) stress-strain curve and the corresponding high speed images for a typical specimen with a higher failure strain; (b) stress-strain curve and the corresponding high speed images for a typical specimen with a lower failure strain; (c) the corresponding light intensity and the stress relation for the specimen shown in (a); (d) the corresponding light intensity and the stress relation for the specimen shown in (b).

4.1.3.2 Imaging Strain Rate Effects

Twelve specimens were tested under strain rates of 0.0001 to 0.0012 s^{-1} to evaluate strain rate effects on the stress-strain behavior of compact bovine femur bone. The experimental results showed that the stress-strain curves fell into two groups: one turned as lower strain rate group with strain rates lower than 0.0007 s^{-1}; and the other turned as higher strain rate group with the strain rates equal to or greater than 0.0007 s^{-1}. In the high strain rate group, specimens showed viscoelastic behavior with non-linear stress-strain curves, even in the elastic region. The Young's modulus for this group was calculated as dynamic Young's modulus by dividing the ultimate stress by failure strain. The average Young's modulus of the higher strain rate group was 41.9 GPa, which was about twice that of the lower strain rate group (21.9 GPa). However, the failure strain of the higher strain rate group (0.3%), was about half of the failure strain of the lower strain rate group (0.7%). The difference between the average ultimate stress for the two groups (which was 123.4 MPa for the higher strain rate group and 105.2 for the lower one) was not significant. The plots of Young's modulus, energy absorption capacity, ultimate stress, and the failure strain as a function of strain rate are shown in Fig. 4.4c, d. Young's modulus and ultimate stress have a positive correlation with strain rate, and the energy absorption capacity and the failure strain have a negative correlation with strain rate. The correlation of the stress-strain curve and the high speed images for a typical specimen subjected to a higher strain rate is shown in Fig. 4.4a. The corresponding plots of stress-microcracking illumination and strain-microcracking illumination are shown in Fig. 4.4b. It was shown that the microcracking illumination of the specimen initiated at the onset of yielding, then rapidly increased until failure.

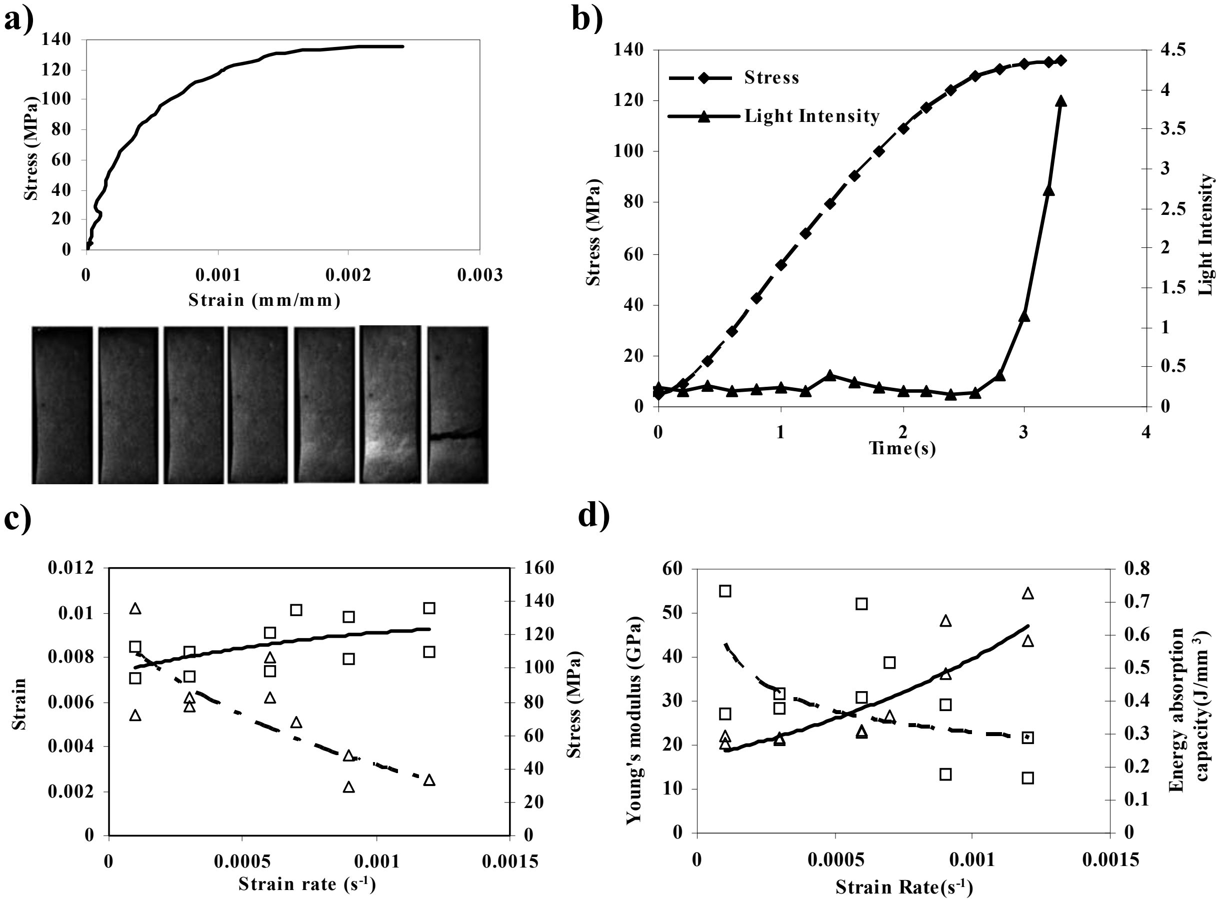

Figure 4.4 Strain rate effects on the mechanical behavior of the longitudinal compact bovine femur specimens: (a) stress-strain curve with the corresponding high speed images for a typical specimen under a strain rate of $0.0012s^{-1}$; (b) the corresponding relation of stress and microcracking illumination for the specimen; (c) the variation of failure strain and ultimate stress with strain rate, △ represents Failure strain and □ represents Ultimate stress; (d) the variation of Young's modulus and energy absorption with strain rate, △ represents Young's modulus and □ represents Energy absorption capacity.

4.1.3.3 Imaging Orientation Effects at a Loading Rate of 0.0001 s^{-1}

The stress-strain curves of the transverse and longitudinal specimens are shown in Fig. 4.5a. It can be seen that the transverse specimens exhibited a strain softening behavior unlike the strain hardening that was typically observed on the longitudinal specimens. The ultimate stress and the Young's modulus of the longitudinal specimens were about twice of the transverse specimens (Fig. 4.5b). The plots of the stress-microcracking illumination and strain- microcracking illumination of a typical transverse specimen are shown in Fig. 4.5c, d, respectively. Unlike the smooth growth of the post-yield light intensity observed on the longitudinal specimens, it was found that the light intensity of the transverse specimens had a significant jump after yielding.

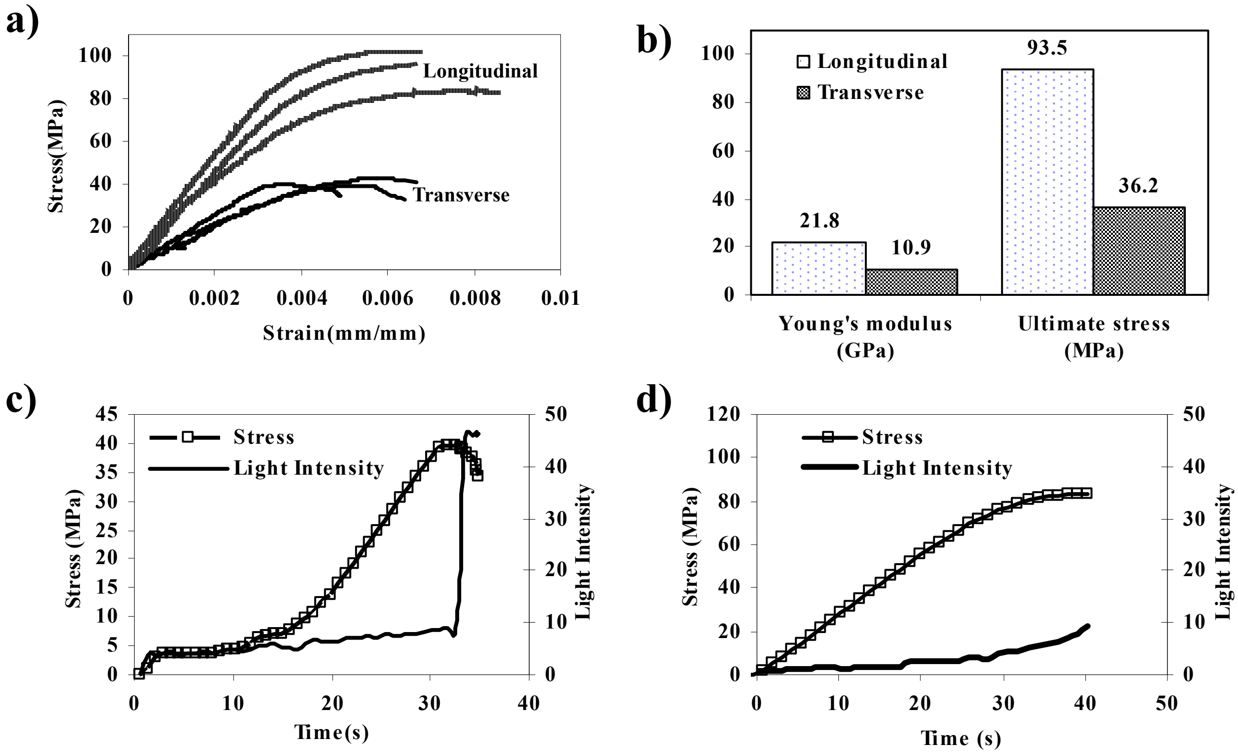

Figure 4.5 The orientation effects on the mechanical properties of the compact bovine femur specimens under a constant strain rate of 0.0001 s^{-1}: (a) the stress-strain curves of the longitudinal and transverse specimens; (b) the comparison of the Young's modulus and ultimate stress of the transverse specimens to the longitudinal specimens; (c) plot of stress and light intensity changing with time for a typical transverse specimen,☐ represents stress and solid line represents light intensity; (d) plot of stress and light intensity changing with time for a typical longitudinal specimen,☐ represents stress and solid line represents light intensity

4.1.3.4 SEM Post-failure Examination

The post-failure photographs of the tested specimens were examined by the SEM. For specimens subjected to the same loading rate, the examination focused on the histological structures and the qualities aspects of microcrack lengths and densities. Fig. 4.6a, b shows the fracture surfaces of the specimens at a failure strain of 2.4% (a) and 0.9% (b). The SEM images show the hierarchical structure of the compact bone, which includes planar lamellae (primary bone), and osteons characterized by cylindrical lamellae surrounding the Haversian channel. Six typical specimens were selected to calculate the osteon area percentage for the entire fracture surface by following Saha's method [13]. The results (Fig. 4.6c) agreed well with the literature showing that the energy absorption capacity and failure strain are negatively correlated with the area percentage of the osteons [7, 8]. Four typical specimens subjected to the same loading rate (0.0001 s^{-1}) were chosen to examine the flat surfaces close to the fracture surface (Fig. 4.7). Higher micro-crack densities and long linear macrocracks over five hundred microns (Fig. 4.7a) were observed on the specimens with higher failure strains.

The typical post-failure SEM images of the longitudinal and transverse specimens are shown in Fig. 4.8. Compared to the microcracks that developed on the longitudinal specimens (Fig. 4.8b), the crack length and density of the transverse specimens were much higher (Fig. 4.8a). The corresponding fracture surfaces of the two typical specimens were shown in Fig. 4.8 c, d, respectively. It can be seen that the fracture surface of the transverse specimen (c) was much smoother in compared to the longitudinal specimen (d). The fracture surfaces of the specimens for the strain rate effects were examined. The SEM images for two typical specimens are shown in Fig. 4.9. Osteon pullout was observed on both of the specimens. But the specimen subjected to the strain rate of 0.0012 s-1 seemed to show more sharp tearing fracture surface (Fig. 4.9c, d) as compared to the specimen under lower strain rate (Fig. 4.9a, b).

4.1.4 Discussion

Innovative use of a relatively simple optical technique was used to study the accumulation of damage in the form of microcracking in compact bovine bone specimens subjected to tensile loading.

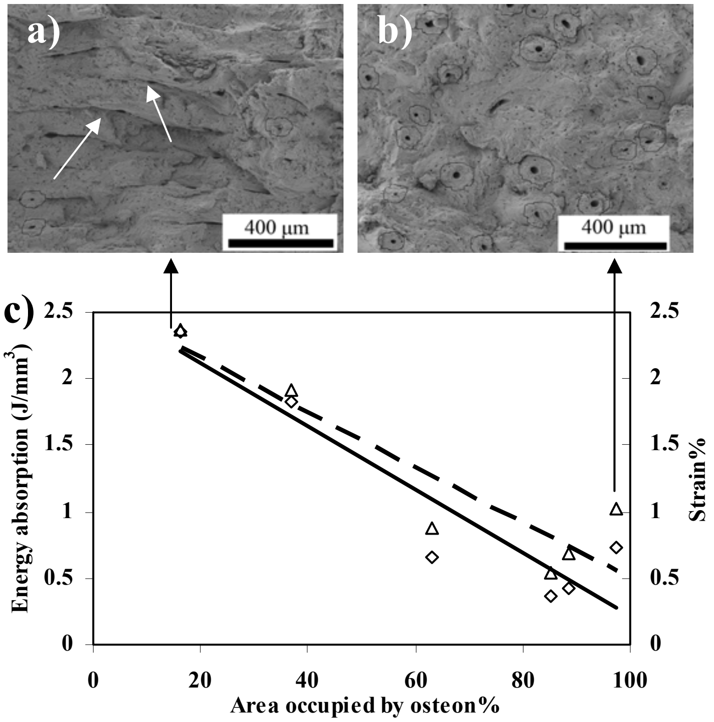

Figure 4.6 Microstructure effects on the mechanical properties of the longitudinal compact bovine femur specimens subjected to a constant strain rate of 0.0001 s^{-1}: (a) SEM fracture surface of a typical specimen with a failure strain 2.4%; (b) SEM fracture surface of a typical specimen with a failure strain of 0.9%; (c) plots of failure strain and energy absorption capacity to the percent area of osteons of the specimens. △ represents failure strain, ◇ represents energy absorption capacity. Dot line is the linear trend line for failure strain; solid line is the linear trend line for energy absorption capacity. Osteons characterized by cylindrical lamellae surrounding the Haversian system, which are circled in a, b. Primary bone characterized by laminar structures (see arrows in b). The area percentages of osteon in the whole fracture surface were calculated following Saha's methods [13].

This powerful approach relates the orientation, microstructure, and strain rate to the resulting micro damage in femoral bovine bone. The post-failure fracture and flat surfaces were examined by SEM. The tensile properties are in good agreement with the literatures (Table 4.1). The initiation and propagation of the microcracks in the specimens is indicated by its light illumination visualized by a high speed camera. The correlation of the high speed images to the stress-strain curves showed that microcracks initiated immediately after yielding (Fig. 4.2a, b, and Fig. 4.3a). It was found that the specimens loaded along the osteon direction showed different failure patterns as compared to the specimens loaded along the transverse osteon direction. For the longitudinal spec-

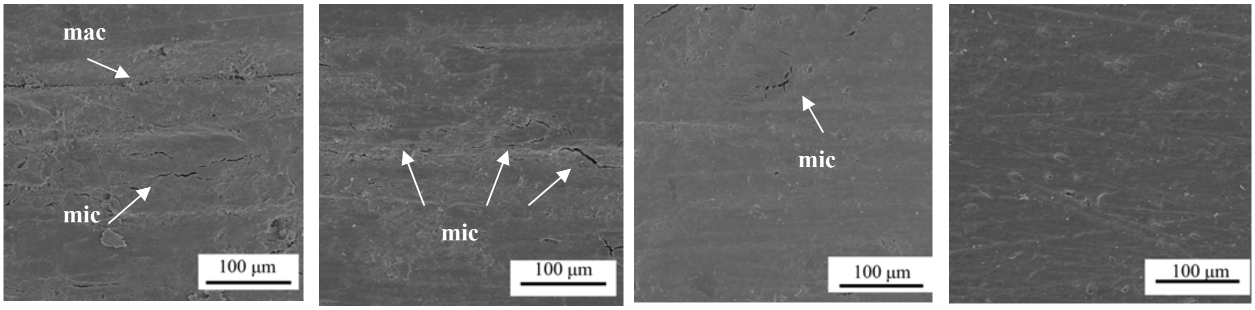

Failure strain: 2.4% **Failure strain: 1.9%** **Failure strain: 0.9%** **Failure strain: 0.5%**

Figure 4.7 Representative SEM post-failure flat surface images (close to the fracture edge) of four typical longitudinal specimens under a constant strain rate of 0.0001 s^{-1}. Example features are labeled: (mac) macrocrack with a crack length over 500 μm, (mic) microcrack with a crack length smaller than 500μm. Long linear macrocracks and many microcracks were observed on the specimen with a large failure strain (a), but not on the specimens with small failure strain (c, d).

imens, the microcracking increased gradually after yielding until failure and microcracks tended to toughen the specimens by showing strain hardening behavior. The specimens that exhibited more microcracks were shown to absorb more plastic energy before failure and the microcracking tended to be more localized with increasing strain rate. However, for the transverse specimens, the microcracking instantly increased to its peak value remaining constant till failure. Strain softening behavior was observed on the transverse specimens.

Table 4.1 Comparison of mechanical tensile properties among different investigators.

	Strain rate s^{-1}	**Specimen**	**Specimen condition**	**Young's Modulus (GPa)**	**Ultimate Stress (MPa)**	**Failure strain%**	**Energy-absorption capacity ($10^6 J/m^3$)**
Present results	**0.0001-0.0012**	**Bovine Femur**	**Wet**	**18.3-54.8**	**83.0-135.8**	**0.2-2.4**	**0.2-1.8**
M.Pithious (2004)	**0.5-500 mm/min**	**Bovine Shaft**	**Dry**	**11.3-17.5**	**105-193**	**0.9-1.8**	**NR**
S.Saha (1973)	**133**	**BovineTibia+Femur**	**Wet**	**12.6**	**121.3**	**1.3**	**NR**
R.D. Crowninshield (1974)	**0.00167-250**	**Bovine Tibia**	**Wet**	**11-12**	**110-250**	**3-6**	**3.8-6.0**
J.D. Currey (1975)	**0.00013-0.16**	**Bovine Femur**	**Wet**	**22.8**	**107.4**	**NR**	**NR**
T.M. Wright (1976)	**0.00053-237**	**Bovine Femur**	**Wet**	**17.7-40.4**	**99.2-271.4**	**NR**	**0.4-1.3**

Microcracking in bone has been shown to contribute to the rising R-curve behavior [27, 25, 17, 18, 19] because its toughening mechanism is similar to brittle materials such as ceramics [28, 29]. It was also found that microcracking tended to impair the mechanical properties of compact bone

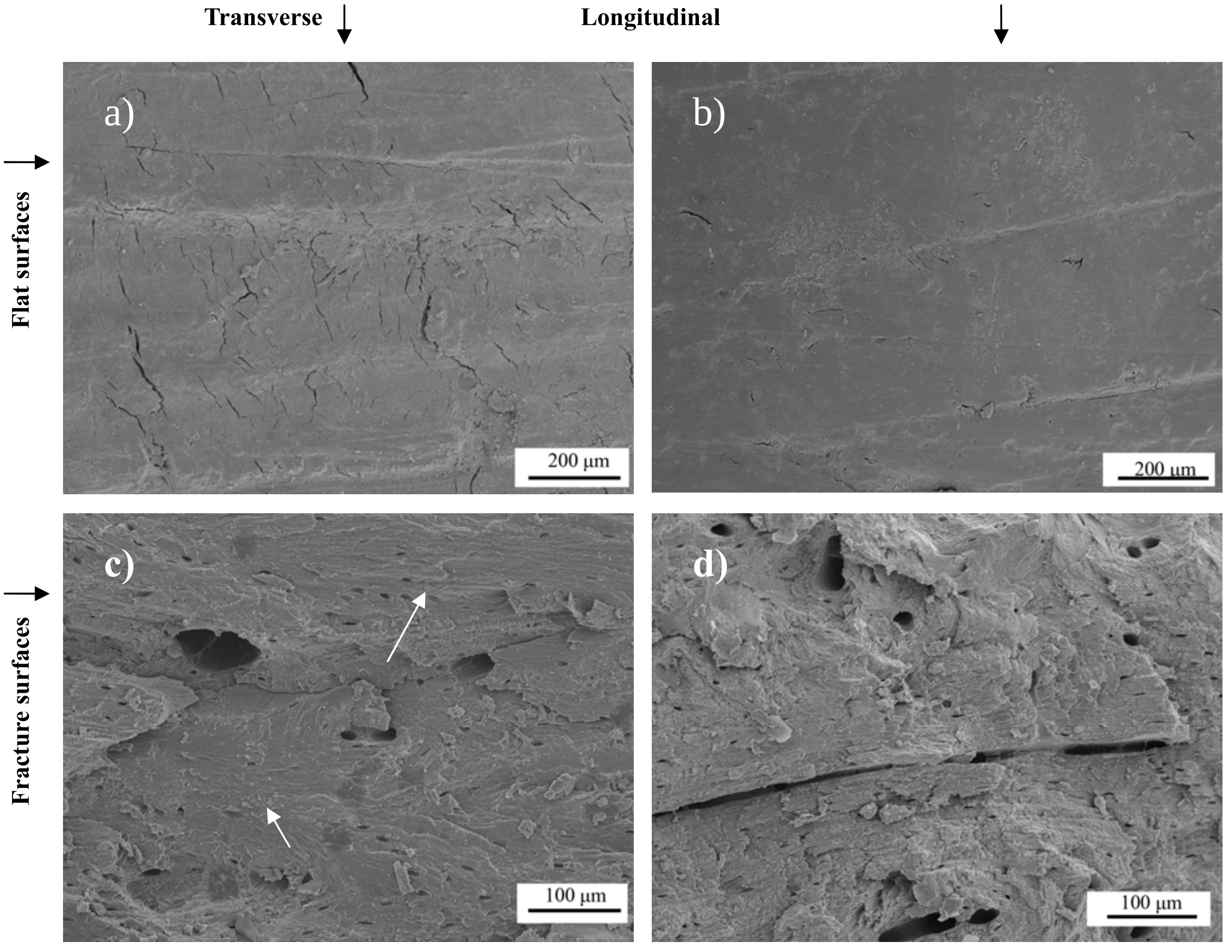

Figure 4.8 Representative SEM post-failure images of two typical specimens (under a strain rate of 0.0001 s^{-1}) for orientation evaluation: (a) the flat surface of the transverse specimen; (b) the flat surface of the longitudinal specimen. Many linear microcracks were observed on the transverse specimens compared to the longitudinal specimen with fewer microcracks; (c) the corresponding fracture surface of the transverse specimen; (d) the corresponding fracture surface of the longitudinal specimen. Smoother tearing surfaces (indicated by arrows) were observed on the transverse specimen in compared to the rough fracture surface of the longitudinal specimen.

during cyclic loading [15, 30, 24, 16]. The present study focused on the effects of microcracking on the mechanical behavior of compact bovine specimens subjected to uniaxial tensile loading. For longitudinal specimens, our results agreed well with the literature [23, 21]. That is, specimen post-yield behavior was affected by the extent of microcracking and the specimen subjected to the low strain rate loading showed more microcracking when compared to the specimens subjected to

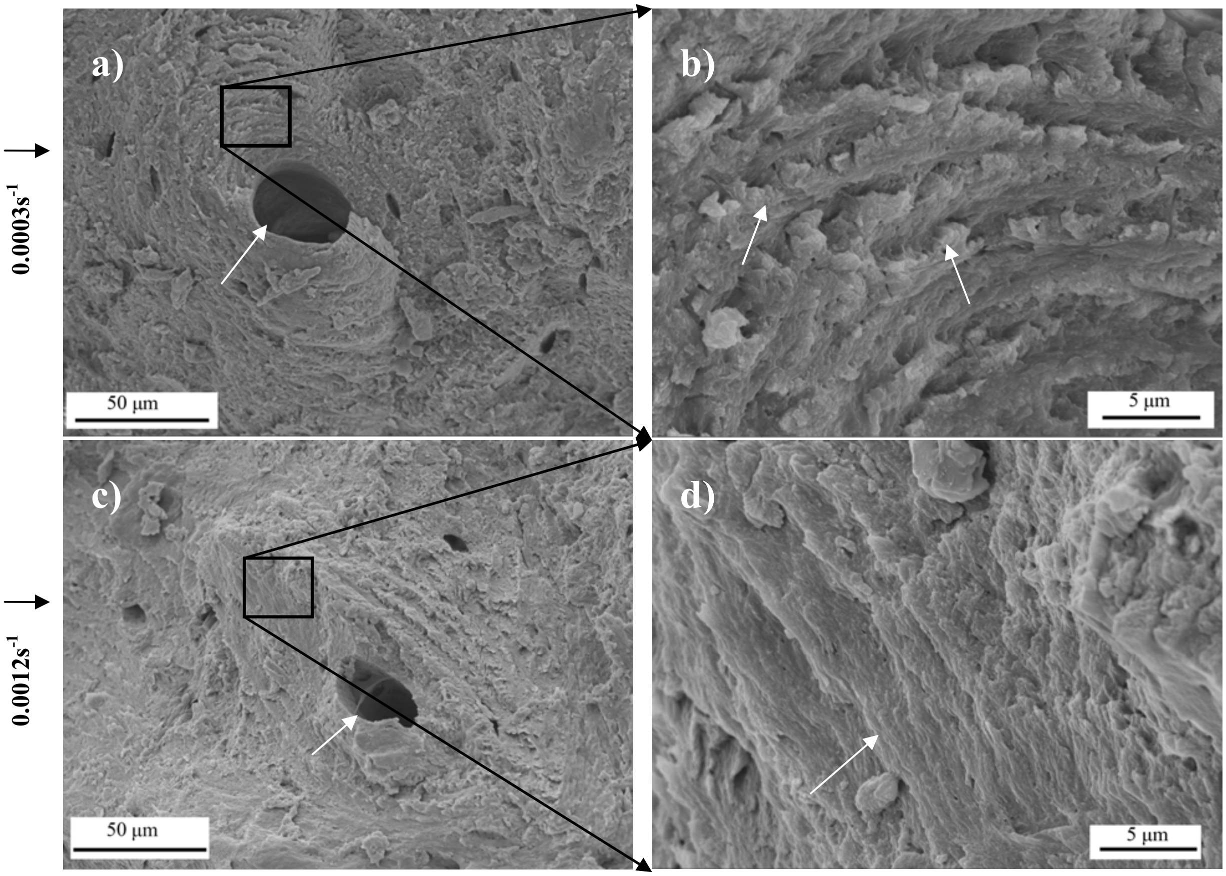

Figure 4.9 Representative SEM post-failure fracture surface images of two typical longitudinal specimens for the strain rate effects evaluation: (a), (b) osteon pullout of the specimen under a strain rate of $0.0003s^{-1}$; (c), (d) osteon-pull out of the specimen under a strain rate of 0.0012 s^{-1}. Osteon is comprised of the Haversian canal (pointed out by arrows) surrounded by cylindrical lamellae. The close view images show that lower strain rate specimen exhibit rougher fracture surface (the ridge rings pointed out by arrows (b)) as compared to the higher strain rate specimen with a smoother tearing surface (see arrow in (d)).

high strain rate loading. The light illumination of microcracking showed that the microcracking tended to be more coalesced in specimens subjected to a high strain rate. The steeper slope of the microcracking illumination suggested a higher propagation speed for the high strain rate specimens. Type I collagen, which is the major organic composition of bone lamellae, contributes to the viscoelastic behavior of cortical bone. With an increase in the loading rate, the collagen tends to be more brittle [27], which is hypothesized to cause the changing in the elastic behavior of bone, leading to a decrease in the energy absorption capacity. Microcracking has been shown to only affect the post-yield behavior of bone. And with an increase in the loading rate, the point-yield strain decreased. Thus, the effects of the post yield behavior on the overall mechanical response of bone tended to decrease. This suggests that when tested under a high strain rate, the effects of type I collagen on the elastic part of the stress-strain curve seemed to be the critical factor to determine bone's failure behavior when compared to the microcracking effects of the mineralized bone tissue.

Although it has been found that diffuse microcracks may develop at the submicron level [31], the hierarchical structure plays a role in determining the bone behavior [32]. At the micro structural level, compact bone can be considered as a bone matrix with osteon fiber distributed along the longitudinal direction. Osteon resulting from bone remodeling is comprised of Haversian channels surrounded by concentric lamellae. Osteon has less mineralization and a relatively weaker connection with the surrounding bone tissue when compared to the primary bone deposited as the bone grows. The post-failure microstructure examination by SEM indicated that the specimens with a higher area percentage of primary bone exhibited the ability to develop more dispersed microcracking than the bone with a higher area percentage of osteons. These results again agreed with similar trends in the literature [7, 8].

Bone is a natural composite where osteons, growing along the loading axis, serve as fibers to enhance the mechanical properties of bone [33, 34]. The orientation effects on the compression mechanical properties of compact bone have been studied by some researchers [5, 9, 27, 35, 36]. It was found that compact bone was stronger in the longitudinal direction than in the transverse direction and that the ultimate strength and the Young's modulus of the longitudinally loading specimens were higher than the specimens loaded in the transverse direction. Reilly [37] conducted tensile, compression, and torsion tests on compact human and bovine bone, where the Young's modulus and ultimate stress were 22 GPa and 133 MPa for the longitudinal specimen, and 11.3 GPa and 51 MPa for the transverse specimen. The corresponding measurements from the present study were 21.8 GPa and 93.5 MPa, and 10.9 GPa and 36.2 MPa, respectively. The correlation of the stress-strain curves and the light illumination of the microcracking showed that microcracking tended to toughen the longitudinal specimens and soften the transverse specimens. The instant jump of the light intensity to the peak plateau (Fig. 4.4c, d) after yielding indicates that many microcracks were induced on the transverse specimens suddenly. The post-failure images by SEM further confirmed the microcracking illumination results by showing that comparatively large numbers of microcracks with lengths up to hundreds of microns were developed on the transverse specimens. The post-failure fracture surfaces of the two-directional specimens clearly showed the different failure pattern of the two directions. The transverse specimens showed much smoother fracture surfaces when compared to the longitudinal specimens, which were characterized by osteon pullout. This can be explained by the pullout along the osteon direction (the fiber direction for a composite material) and would be harder than pulling by the cement line. Transverse specimens showed that many microcracks instantly initiated in the cement lines, which resulted in the stiffness loss in the specimen. The present results show that, to some extent, microcracking serves as a toughening mechanism; but if it is over a critical value, microcracking weakens the specimen leading to failure. It is pertinent to further investigate the toughening mechanism of microcracking in terms of density and length from the aspect of fracture mechanics.

4.2 Microcracking Morphology of Compact Bovine Bone Subjected to Impact Loading

4.2.1 Non-notched Beam Specimens of Compact Bovine Femur Subjected to Charpy Impact Loading

4.2.1.1 Material and Methods

All the specimens were machined out of fresh compact bovine femurs (60 months old) provided by a local beef abattoir. The mid-diaphysis of the bovine femur was cut into rectangular samples. During the entire machining process, the specimens were kept wet with phosphate buffered saline (PBS) solution. After machining, the specimens were covered with gauze dipped in PBS solution and preserved in a $-20^{\circ}C$ freezer until testing. Specimens were thawed prior to testing.

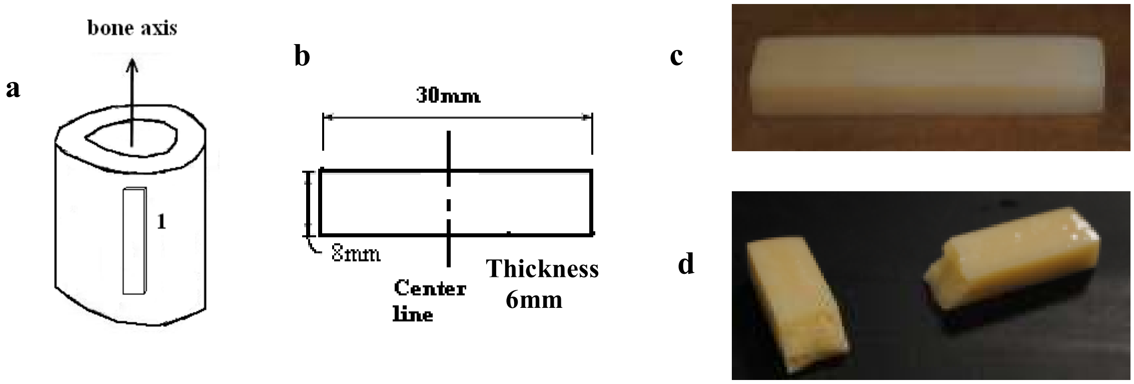

Figure 4.10 Bone specimens: a, A diagram shows the orientation of bone (osteon grows along bone axis); b, Dimensions of bone specimen; c, A typical specimen before testing; d, A typical specimen after testing.

The dimensions of bone specimens are shown in Fig. 4.10. To examine the microcracking morphology subjected to impact loading, non-notched beam specimens of compact bovine femur were loaded with an instrumented Charpy impact system under different impact energy levels.

A tabletop Charpy impact system with light impact mass (0.6 kg) was designed to perform the low energy (ranging from 0.1 to 2.3 J) impact tests. The Charpy impact system is shown in Fig. 4.11, 4.12. The load cell, projectile, and hammer weighed 0.6 kg. When the hammer system was dropped at different heights, various impact energy was imposed on the tested specimens. The projectile was perpendicular to the specimen at the moment of impact.

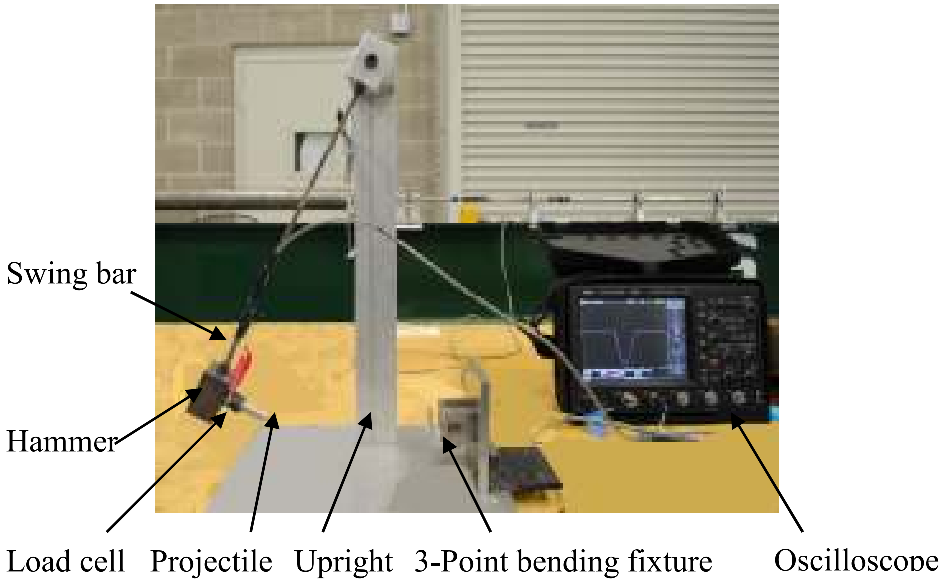

Figure 4.11 Tabletop Charpy impact system.

The length of the swing bar, L, was 0.39 mm. The initial velocity was calculated as

$$v_{initial} = \sqrt{2gL\cos\theta} \tag{4.1}$$

where θ was the initial angle between the center lines of swing bar and the upright.

The load cell was calibrated before the testing and it yields relationships between voltage, strain (ε), force (F), and strain (ε) as

$$1.004Voltage = 125\mu\varepsilon \tag{4.2}$$

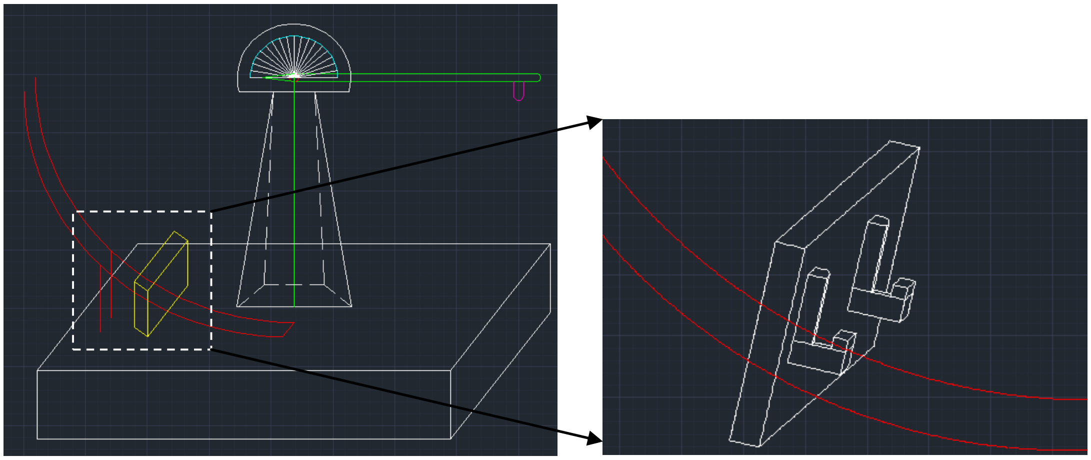

Table-on Charpy Impact Apparatus

Three Point Bending Fixture

Figure 4.12 Schematic representative of the table-on Charpy impact system.

$$F = 7.55\varepsilon \tag{4.3}$$

Thus, the velocity (v) and displacement (s) of the projectile at any time during the impact event can be calculated as

$$a = F/m \tag{4.4}$$

$$v = v_{initial} + \int a dt \tag{4.5}$$

$$s = s_{initial} + \int v dt \tag{4.6}$$

where m is the total mass (0.6 kg) of the projectile, hammer, and load cell. Thus, impact energy (E) can be calculated

$$E = \int F ds \tag{4.7}$$

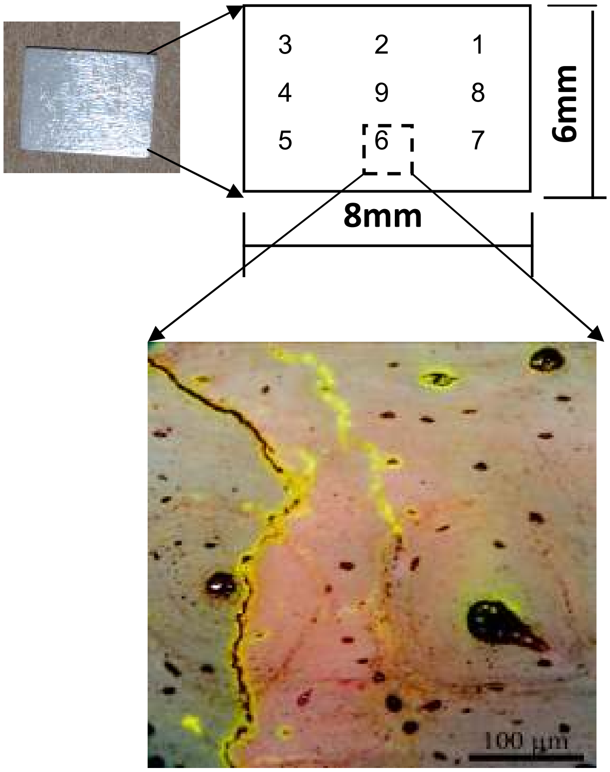

Figure 4.13 The locations and orders of the viewpoints examined and a sample of microscope image.

The impact energy was set up to be 0.14, 0.31, 0.41, 0.53, and 0.67 J respectively. Four specimens were tested in each energy level. After the tests, the tested specimens were soaked in the basic fusion solution according to Frost's basic fusion technique [22]. After bulk stain, a thin section (thickness, 3 mm) was cut off from the end closest to the fracturing surface by a band saw. The surface interested was the cross section of the beam specimen perpendicular to the osteon growing direction. The thin sections were first polished by a Leco wafering saw with a precision of 0.01 mm and then followed by final polishing by a Leco lapcloth polishing machine with precision of 1 μm. The final polished ground sections were 8x6x0.3 mm. Then microcracks and microstructures of each of the ground sections were visualized and photographed by an Olympus BHS microscope with a Spot digital camera (Diagnostics Inc). Microscopic images

Table 4.2 Summaries of all the testing results.

Run No.	Impact Energy Applied (J)	Energy Dissipated (J)	Area Percentage Occupied by Secondary Osteon %	Cracks No.	Sample Status After Testing
E2_Run1	0.14	0.082	100	0	No. Broken
E2_Run2	0.14	0.090	31.85	0	No. Broken
E2_Run3	0.14	0.109	26.78	0	No. Broken
E2_Run4	0.14	0.088	100	0	No. Broken
E3_Run1	0.31	0.284	95	0	No. Broken
E3_Run2	0.31	0.287	90	0	No. Broken
E3_Run3	0.31	0.201	20	1.36	Broken
E3_Run4	0.31	0.306	100	0	No. Broken
E4_Run1	0.41	0.393	15	0	No. Broken
E4_Run2	0.41	0.248	5	0	Broken
E4_Run3	0.41	0.402	100	0	No. Broken
E4_Run4	0.41	0.390	100	0	No. Broken
E5_Run1	0.53	0.487	8	0	Broken
E5_Run2	0.53	0.489	20	0	No. Broken
E5_Run3	0.53	0.517	100	0	No. Broken
E5_Run4	0.53	0.511	5	0	No. Broken
E6_Run1	0.67	0.460	5	1.1	Broken
E6_Run2	0.67	0.624	25	0	No. Broken
E6_Run3	0.67	0.507	5	0.77	Broken

at different magnifications (the maximum field of view was 2.25 x 1.6 mm at magnification x5) were taken for each ground section. The locations and orders of the viewpoints examined and a sample of microscope image are shown in Fig. 4.13.

4.2.1.2 Results and Discussion

The testing results are summarized in Table 4.2. The relationships of impact energy with time and impact force with time are shown in Fig. 4.14, 4.15 respectively. It was found that no specimens fractured at the impact energy of 0.14 J; one specimen fractured at each of the impact energies of 0.31, 0.41, and 0.53 J; and three specimens fractured at the impact energy of 0.67 J. One of the specimens which fractured at the impact energy of 0.67 J possessed pre-existing defects and was therefore discarded and omitted from Fig. 4.14, 4.15, and Table 4.2).

Two representative post-failure microscopic images at each impact energy level are shown in

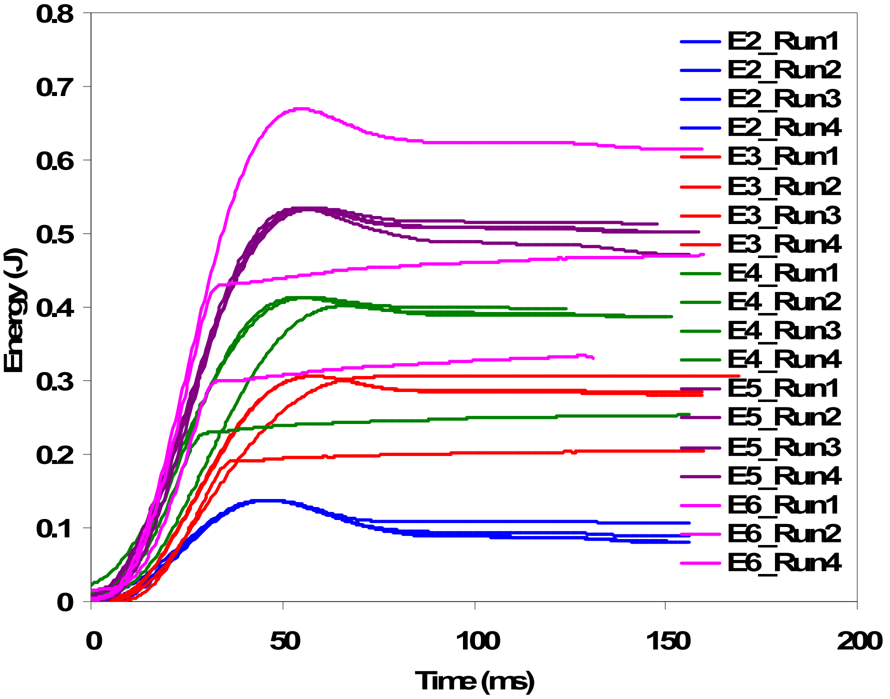

Figure 4.14 Impact force history of bovine cortical bone subjected to Charpy impact loading at various impact energy levels.

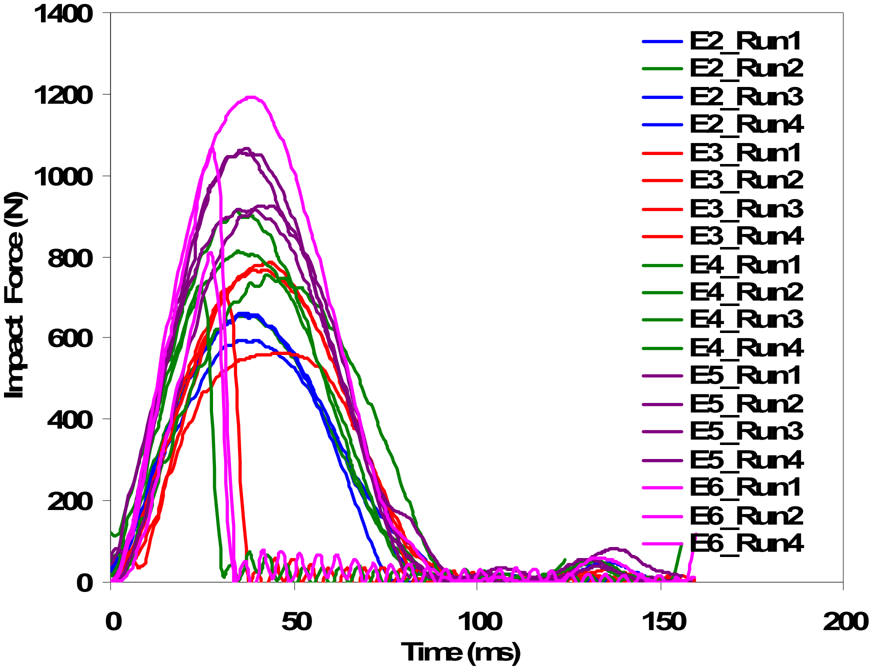

Figure 4.15 Impact energy history of bovine cortical bone subjected to Charpy impact loading at various impact energy levels.

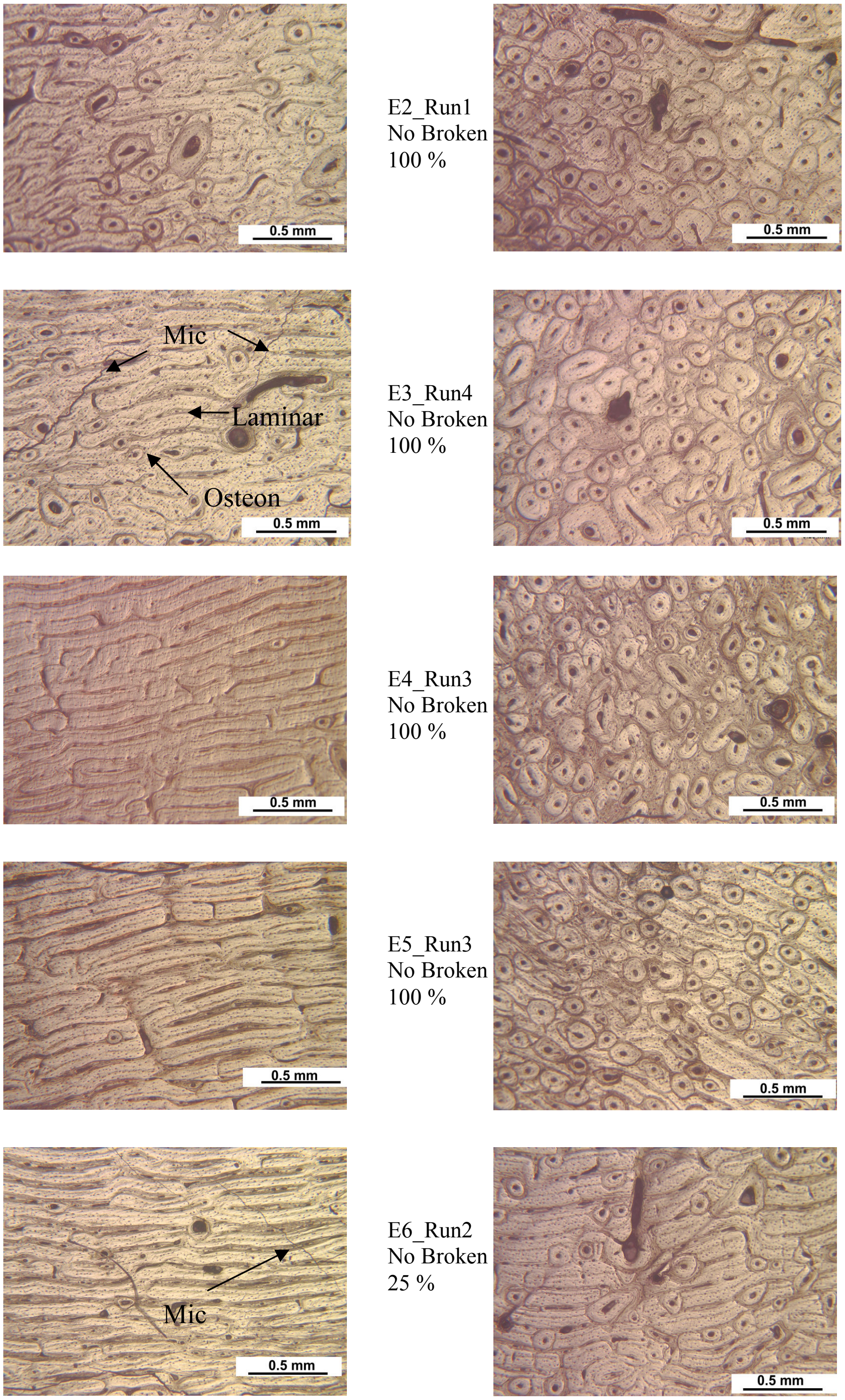

E2_Run2
No Broken
32 %

E2_Run1
No Broken
100 %

E3_Run3
Broken
20 %

E3_Run4
No Broken
100 %

E4_Run2
Broken
5 %

E4_Run3
No Broken
100 %

E5_Run1
Broken
8 %

E5_Run3
No Broken
100 %

E6_Run1
Broken
5 %

E6_Run2
No Broken
25 %

Figure 4.16 Representative post failure microscopic images at each impact energy level. The images are labeled with the run case number (E2_Run2 etc), specimen status after impact (broken or no broken), and the area percentage occupied by the secondary osteon (32%, etc.). Features are labeled as Mic: microcrack, Osteon: secondary osteon, and Laminar: laminar structure.

Fig. 4.16. The correlations of the microcracking numbers to the area percentage occupied by secondary osteon and the impact energy applied are shown in Fig. 4.17. The post-failure examinations showed that no microcracks were visible when the specimen was not broken. The microcracks in the fractured specimens were linear and were usually larger than hundreds of micrometers in length (Fig. 4.16). Fig. 4.17a showed that no specimens fractured or no microcracks were observed when the area occupied by secondary osteon is larger than 25%. The results showed that the threshold energy was lager than 0.14 J. When the applied energy is between 0.31 to 0.53 J, the fracture possibility of specimens was random (Fig. 4.17b) and may rely on the microstructures of the sample. The testing results seemed to conclude that osteon bone can sustain higher impact energy compared to the laminar bone (Fig. 4.16).

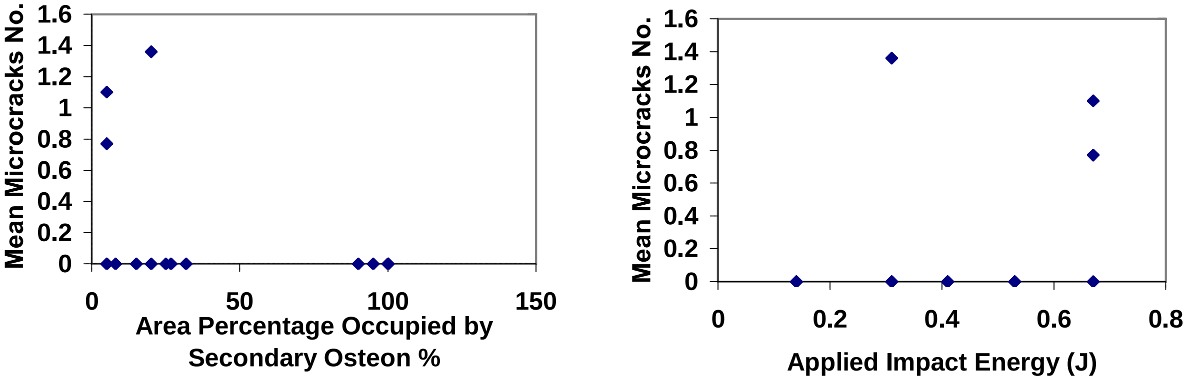

Figure 4.17 a, Correlation of mean microcracking numbers to the area percentage occupied by secondary osteon; b, Correlations of microcracking to the impact energy applied.

4.2.2 High Strain Rate Tensile Tests of Compact Bovine Bone by Split Hopkinson Bar(SHPB)

4.2.2.1 Material and Methods

A designed tensile Split Hopkinson Bar (SHPB) was used to conduct the high strain rate tensile testing (Fig. 4.18). It includes an incident bar (a solid aluminum bar with a big end at the interface with the momentum trap), a transmitted bar (a hollow aluminum bar), a striker (a hollow aluminum cylinder sliding along the incident bar), and a striker stopper also called momentum trap (a solid aluminum bar). The tensile specimen is placed between the incident bar and the transmitted bar with specially designed threaded steel fixture (Fig.4.19).

The tensile specimens were machined from the fresh, compact, bovine femur following the same method as the tensile specimens used for static tensile testing in section 4.1 and are of the same dimensions as the specimen shown in Fig.4.1. The specimens were first glued to the fixture with Loctite E-30CL glass bounder Epoxy adhesive and then were further fixed with four screws in each end (Fig. 4.19). Although the specimens were kept moist with gauze soaked with PBS solution during the preparation of the specimens for the test, the two end of the dog-bone specimen were in dry conditions for the purpose of curing the epoxy. Thus, the conditions of the specimen tested were considered as partially wet.

The incident bar was struck by the striker, which was powered by compressed gas. A tensile wave was created and then propagated through the incident bar toward the specimen. Upon reaching the specimen, part of the pulse was reflected back to the incident bar, and the rest of the pulse was transferred through the specimen to the transmitted bar. The pulse transferring through the specimen caused the deformation of the specimen. A full-bridge strain-gauge configuration was installed on both incident and transmitted bars to capture the wave pulses traveled inside the bar.

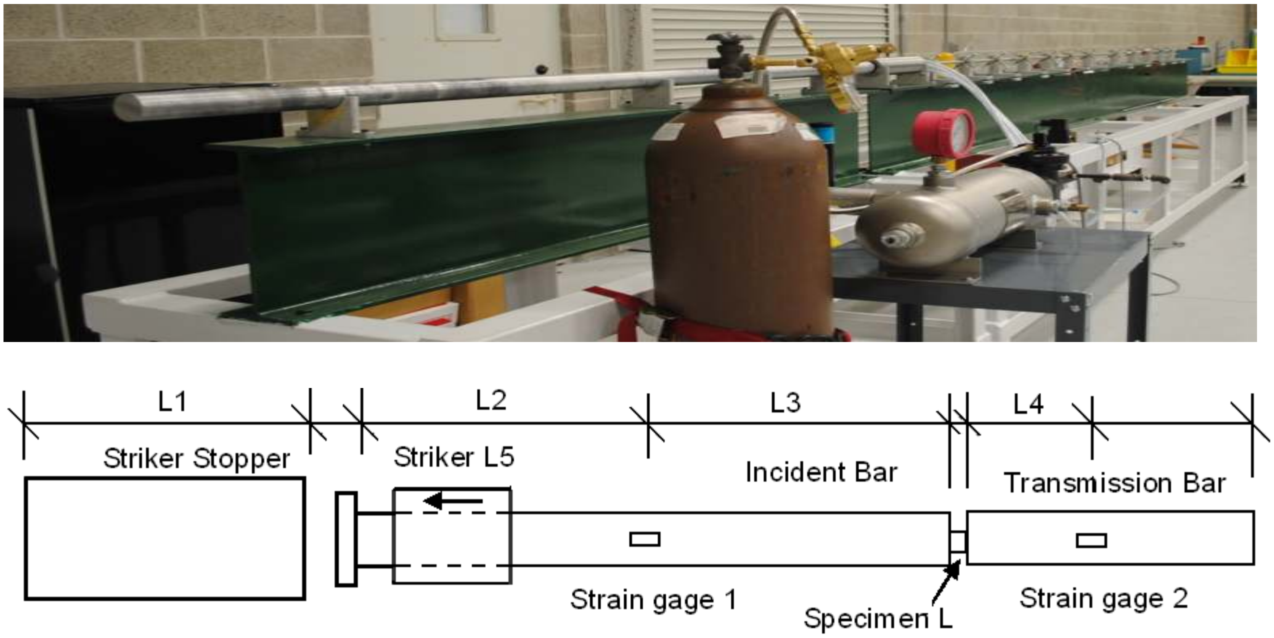

Figure 4.18 SHPB setup for high strain rate testing (300 900 s^{-1}).

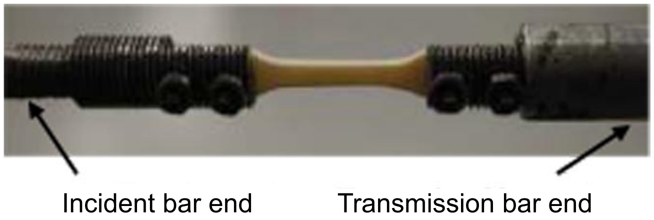

Figure 4.19 A typical specimen fixture used in the SHPB testing.

The pulse waves in the incident and transmitted bars were measured as voltages through an amplifier and an oscilloscope and then were converted to strain. A card-stock paper with a thickness of 0.5 mm was used for pulse shaping to obtain a clean pulse. It has been shown that, by using strong light scattering effects of crack edges, light illuminations of the microcracks on the specimen surface were observed on the specimens subjected to quasi-static tensile testing (see section 4.1) [38]. Thus, in order to visualize the fracture behavior of bovine cortical bone subjected to high strain rate loading, a high speed camera (Phantom v12.1) with a LED panel was also set up to record the fracture process during the SHPB testing.

4.2.2.2 Results and Discussion

A typical incident and transmitted waves measured are shown in Fig. 4.20. It can be seen that only a small portion of the incident pulse was transmitted to the transmission bar. This was due to the low impedance in the bone sample and the area mismatch between the incident and transmitted bar with the dog-bone shaped bone specimens.

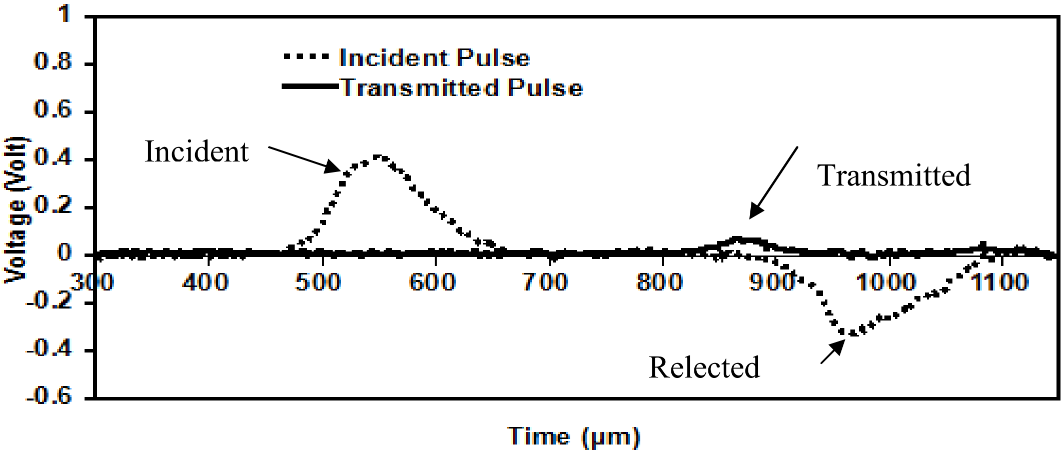

Figure 4.20 A typical incident and transmitted waves measured in the SHPB testing of bovine bone specimens.

The stress and strain fields are derived from the classic wave theory [39]. Stress in the specimen

$$\sigma_s = \frac{A_1 E(\varepsilon_I(t) + \varepsilon_R(t)) + A_2 E \varepsilon_T(t)}{2A_s} \tag{4.8}$$

Strain in the specimen

$$\varepsilon = \frac{C_0}{L} \int_0^t [\varepsilon_I(t) - \varepsilon_R(t) - \varepsilon_T(t)] dt \tag{4.9}$$

Strain rate

$$\dot{\varepsilon} = \frac{C_0}{L} (\varepsilon_I(t) - \varepsilon_R(t) - \varepsilon_T(t)) \tag{4.10}$$

where E is the Young's modulus of the incident and the transmitted bar (aluminum), 70 GPa;

ε_I, ε_R, ε_T is the incident, reflected, and transmitted strain field respectively; A_1, A_2, A_s is cross-section area of incident bar, transmitted bar, and sample respectively; C_0 is the wave speed in the incident and transmitted bar, 5092 m/s; and L is the gauge length of the bone sample. A schematic representation of the interfaces between incident bar with sample and sample with transmission bar is shown in Fig. 4.21.

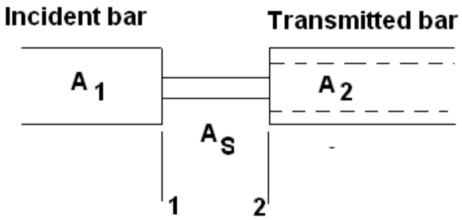

Figure 4.21 Schematic representation of interfaces between incident bar with sample and sample with transmission bar.

The stress and strain relationships obtained from the high stain rate tensile testing are shown in Fig. 4.22. The correlation of the ultimate stress and the strain at ultimate stress with the corresponding strain rate are shown in Fig. 4.23. The results showed that ultimate stress increased with the increase of strain rate before a critical strain rate, 600 s^{-1}. After passing the critical point, the ultimate stress decreased. The average Young's modulus measured was 20.3 GPa. The results have a good agreement with the existing literature [11, 2, 14, 9, 40]. Crowninshiled and Pope [2] examined the response of compact bovine bone in tension at various strain rates (from 0.01 to 200 s^{-1}). Ultimate tensile stress both in longitudinal and transverse increased with the strain rate. Wright and Hayes [14] conducted uniaxial tensile tests of cortical bovine bone at seven strain rates (from 5.3 x 10^{-4} to 237 s^{-1}). The ultimate strength, modulus of elasticity, and energy absorption capacity were found to increase with strain rates. McElhaney [11] investigated the dynamic response of both fresh human and bovine femur subjected to dynamic compressive loading at strain rates up to 1000 s^{-1}. The Young's modulus and ultimate stress increased with the strain rates. Katsmanis

[40] used the SHPB to measure the Young's modulus and Poisson's ratio of human femur cortical bone in both dynamic compressive and tensile loading. Young's modulus in dynamic loading was found to be higher than in static loading, but no difference was found between the Young's modulus in tension and compression. The studies also showed that scattering of results is significant due to its highly heterogeneous structure. The results from the literature and the current study are summarized in Table 4.3.

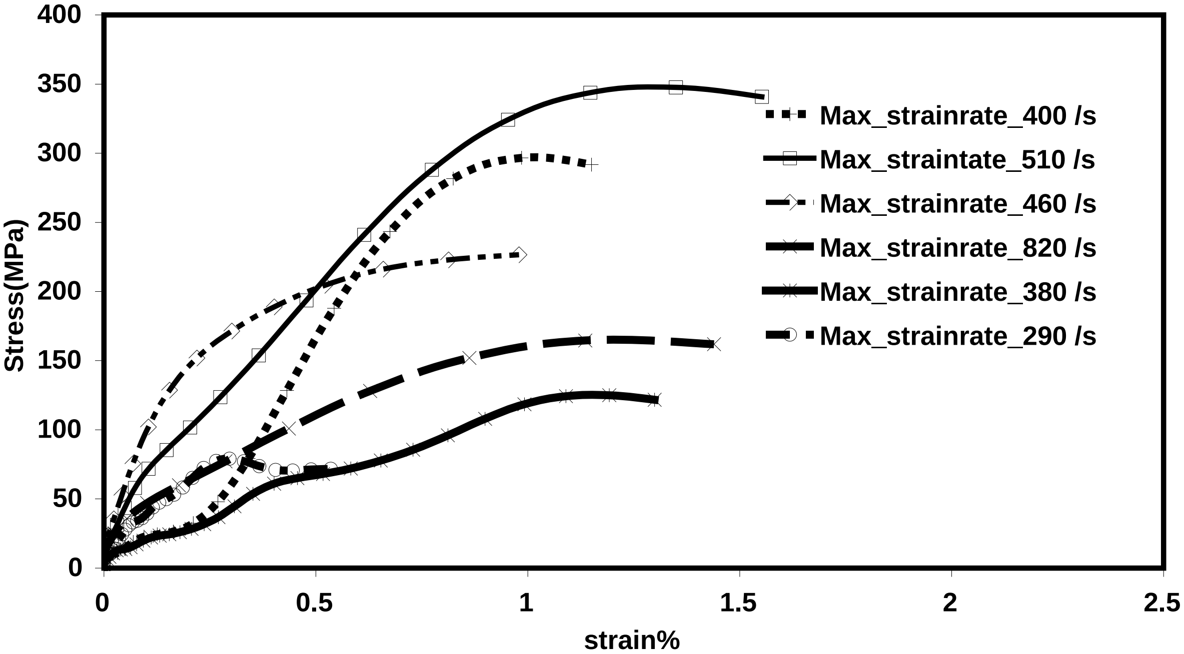

Figure 4.22 Stress-strain relationships of bovine cortical bone subjected to high strain rate tensile loading by SHPB setup.

The maximum frame rate of the Phantom high camera is 1,000,000 FPS with a resolution of 128 x 8 pixels . The wave speed can be roughly calculated as $\sqrt{E/\rho}$. The average density of cortical bone is about 1900 kg/m^3 and the Young's modulus is about 21.5 GPa. Thus, the wave speed in cortical bone is calculated to be 3364 m/s. The length of the dog-bone shaped tensile specimen is 60 mm. Thus, it takes about 17.8 μs for the wave to pass through the specimen. It has been demonstrated that when the raising time of the incident pulse is long enough to allow the

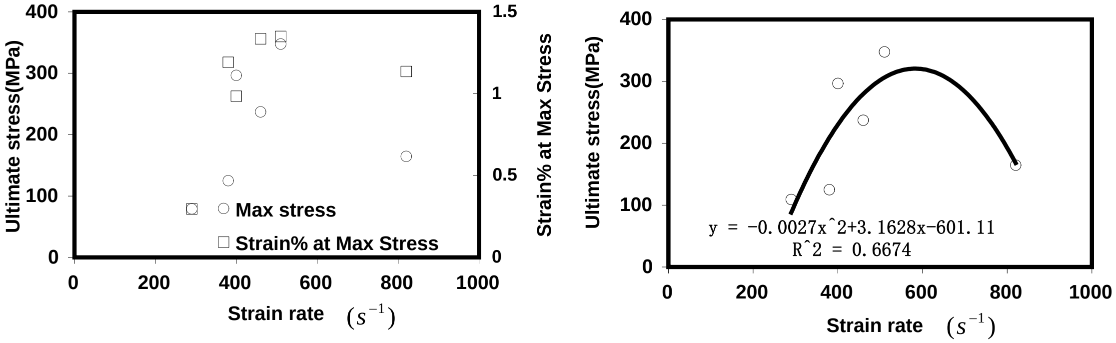

Figure 4.23 a) Correlation of ultimate stress and strain at ultimate stress to the strain rate; b)The polynomial regression model of ultimate stresses at different strain rates.

Table 4.3 Comparison of mechanical properties of cortical bone subjected to high strain rate loading among different investigators.

	Strain rate s^{-1}	Specimen	Loading Type	Specimen condition	Young's Modulus (GPa)	Ultimate Stress (MPa)	Failure strain%	Energy-absortion capacity ($10^6 J/m^3$)
Present results	290-820	Bovine Femur	Tensile	PartiallyWet	10.5-36.8	125-348	0.3-1.2	NR
F. Ferreira (2006)	368-795	Bovine Femur	Compressive	Dry	9.3-19.4	223-310	1.5-3.2	NR
M.Pithious (2004)	1000 m/s	Bovine Shaft	Tensile	Dry	10-21.7	33-50	0.2-0.4	NR
F. Katsamanis (1990)	100	Human Femur	Tensile	Dry	18-23.3	NR	NR	NR
T.M. Wright (1976)	0.00053-237	Bovine Femur	Tensile	Wet	17.7-40.4	99-271	NR	0.4-1.3
R.D. Crowninshield (1974)	0.00167-250	Bovine Tibia	Tensile	Wet	11-12	110-250	3-6	3.8-6.0
J.H. McElhaney(1966)	0.001-1500	Bovine Femur	Compressive	Wet	12.4-48.3	133-400	0.7-2.9	2.2-4.8

wave to reflect back and forth three to four times inside the sample, force equilibrium could be achieved within the initial time [41, 42, 43, 44]. Thus, in order to capture the deformation process of the bone sample during the high strain rate tensile testing, the camera has to be able to record a video with a length of about 50-80 μs (about three to four times the time required for a wave to pass through the specimen) and with a reasonable frame rate. For the present testing, the horizontal resolution of the high speed image was set to be 500-256 pixels and vertical resolution was 100-60 pixels. This setup yielded a frame rate of about 240,000 FPS. Typical stress-strain curves and their corresponding high speed images are shown in Fig. 4.24.

As shown in Fig. 4.25, it took about 50 μs to fracture the sample(from 0 to 0.003ε). The time interval was 8 μs from 0.002ε to 0.003ε. With the current high speed camera used, there was only

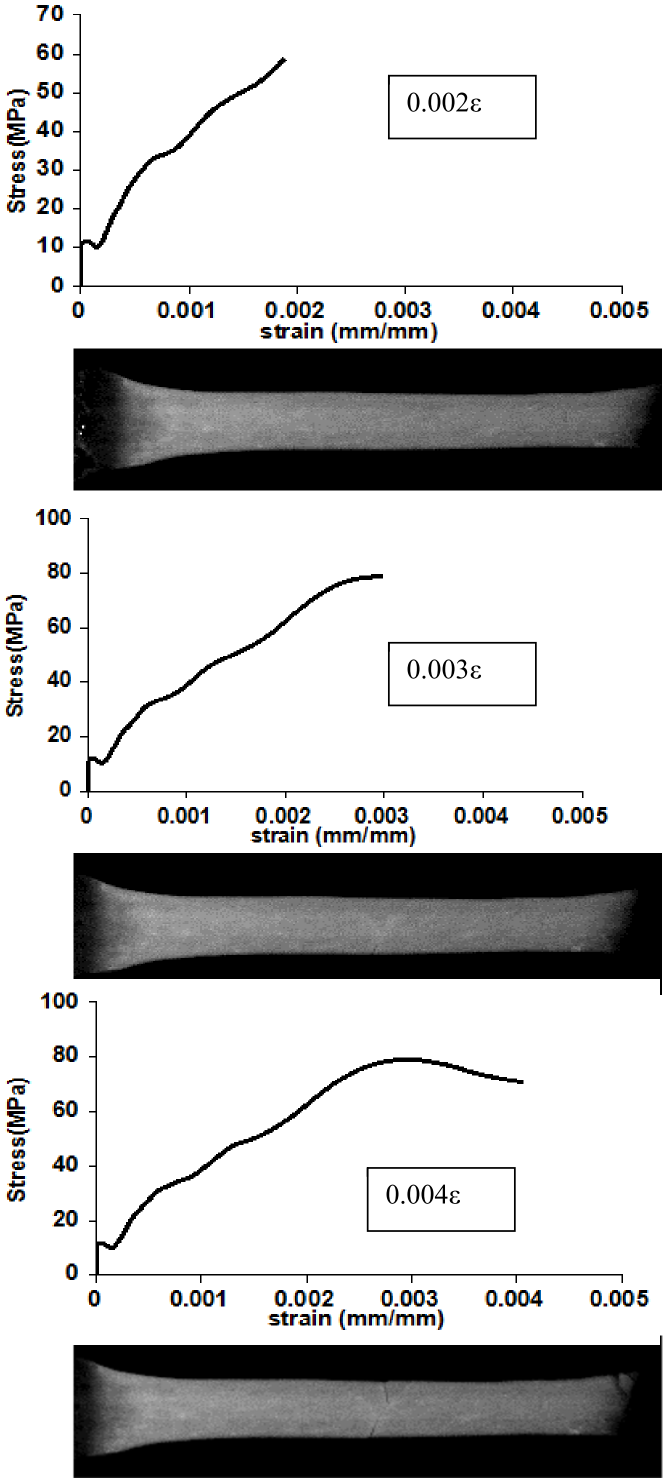

Figure 4.24 Typical stress-strain curves and their corresponding high speed images.

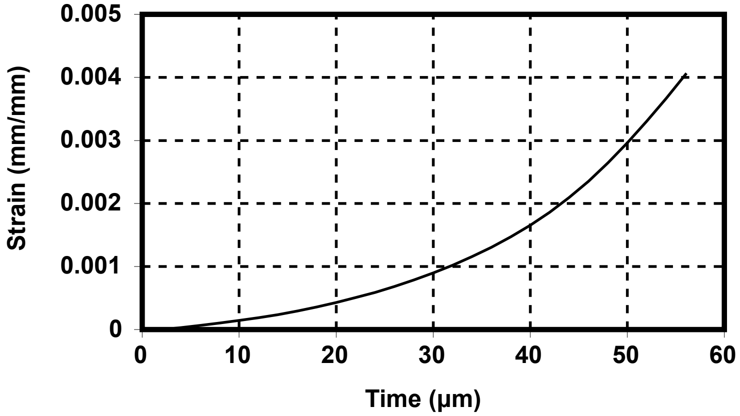

Figure 4.25 The time history of strains of the specimen showed in 4.24.

one image captured at each of these two strains (Fig. 4.24)and no image captured between the two points. Macro-cracking was visualized in the high speed image at 0.003ε and there is no micro- or macro-cracking observed in the high speed image at 0.002ε. There is no micro-cracking being visualized for all the tested samples and the failure behavior followed the similar trend as the one shown in Fig. 4.24, 4.25. It implied that the microdamage or microcracking once initiated would coalesce and extend rapidly (less than several microseconds) to cause the catastrophic failure of the sample. Thus, compared to the ductile failure behavior exhibited during quasi-static tensile tensile, the failure of the bovine cortical bone subjected to high strain rate tensile testing is governed by brittle failure. The observations agree with the existing literature [2, 14, 9].

4.2.3 Conclusion

Damage accumulation in compact bovine femur subjected to uniaxial tensile loading was examined by strong light illumination effects of microcracking. Imaging was done using a high-speed camera capturing images at 200 to 1500 FPS. The tensile tests were performed in a multipurpose tensile testing system with cross-head speeds ranging from 0.5 to 10 mm/min which leads to strain rates of 0.0001 to 0.0012 s^{-1} (physiologically relevant to walking and running [10]). The post-failure images were examined in a scanning electron microscope (SEM); and the effects of microstructure, strain rate, and orientation were evaluated. Correlation of the high-speed images with stress-strain curves indicated that optically visible microcracks were most likely initiated at yielding, and the specimens with dispersed microcracks exhibited a higher energy absorption capacity compared to the specimens with coalesced local cracks. It was found that damage accumulation negatively correlates to strain rate and that transverse specimens exhibited a different failure pattern compared to the longitudinal specimens. Strain hardening and softening were found in the longitudinal and transverse specimens respectively. The microcracking in the transverse specimens instantly increased to a peak after yielding compared to the gradual growth until failure in the longitudinal specimens. The average Young's modulus (21.5 GPa) and ultimate stress (93.5 MPa) of the specimens loaded in the longitudinal direction were more than twice that of the specimens (10.9 GPa and 36.2 MPa respectively) loaded in the transverse direction. The current technique has shown potential in relating real time damage accumulation in bone samples subjected to the static tensile loading condition. This information will be helpful in relating the role of micro-damage accumulation in initiating failure and remodeling in bone.

The microcracking morphology of compact bovine femur subjected to impact loading was investigated by an instrumented Charpy impact system under different impact energy levels. The post failure examinations were performed by a bright-field microscope. The microcracks were counted for each of the samples and were correlated to its microstrutures. The results showed that no samples were broken under the impact energy of 0.14 to 0.67 J when the area percentage occupied by the secondary osteon was higher than 25 %. The microstructures of the broken specimens featured as laminar structures. The threshold energy for the non-notched rectangular specimens was larger than 0.14 J. The experiments showed that osteon bone can sustain higher impact energy compared to the laminar bone.

The microcracking morphology and high strain rate failure behavior of compact bovine femur subjected to high strain rate tensile loading were studied through a designed tensile SHPB system. The ultimate stress and strain at ultimate stress were measured to be in ranges of 125-348 MPa and 0.3-1.2 mm/mm respectively with a strain rate of 290-820 s^{-1}. The Young's modulus was in the range of 10.5 to 36.8 GPa. The ultimate stress was found to increase with strain rate. The fracture processes were recorded through a high speed camera with a frame rate of about 240,000 FPS. The high-speed images were synchronized to the stress-strain curves. Unlike the static tensile testing, no optically visible microcracks were captured during the high strain rate tensile testing. The results indicted that the failure of the cortical bovine bone was governed by brittle failure at a high strain rate. The microdamage initiated and coalesced in a short period of time (less than several microseconds) to cause the catastrophic failure of the sample.

In conclusion, the experiments showed that the microcracking toughening mechanism is the major toughening mechanism of cortical bone in low strain rate loading. In an impact or a high strain rate, the failure behavior depends more on its micro-structure. In the next chapter, the correlation between the microstructures and the macro performance of osteon bone is studied through computational methods.

REFERENCES

REFERENCES

[1] Dennis R Carter, William E Caler, Dan M Spengler, and Victor H Frankel. Fatigue behavior of adult cortical bone: the influence of mean strain and strain range. *Acta Orthopaedica*, 52(5):481–490, 1981.

[2] RD Crowninshield and MH Pope. The response of compact bone in tension at various strain rates. *Annals of Biomedical Engineering*, 2(2):217–225, 1974.

[3] JD Currey and K Brear. Tensile yield in bone. *Calcified tissue research*, 15(1):173–179, 1974.

[4] Charles H Turner. Bone strength: current concepts. *Annals of the New York Academy of Sciences*, 1068(1):429–446, 2006.

[5] Raghavendra R Adharapurapu, Fengchun Jiang, and Kenneth S Vecchio. Dynamic fracture of bovine bone. *Materials Science and Engineering: C*, 26(8):1325–1332, 2006.

[6] Martine Pithioux, Damien Subit, and Patrick Chabrand. Comparison of compact bone failure under two different loading rates: experimental and modelling approaches. *Medical engineering & physics*, 26(8):647–653, 2004.

[7] JD Currey. The effects of strain rate, reconstruction and mineral content on some mechanical properties of bovine bone. *Journal of Biomechanics*, 8(1):81–86, 1975.

[8] S Saha and WC Hayes. Tensile impact properties of human compact bone. *Journal of biomechanics*, 9(4):243–251, 1976.

[9] F Ferreira, MA Vaz, and JA Simoes. Mechanical properties of bovine cortical bone at high strain rate. *Materials characterization*, 57(2):71–79, 2006.

[10] Ulrich Hansen, Peter Zioupos, Rebecca Simpson, John D Currey, and David Hynd. The effect of strain rate on the mechanical properties of human cortical bone. *Journal of biomechanical engineering*, 130(1):011011, 2008.

[11] James H McElhaney et al. Dynamic response of bone and muscle tissue. *J. appl. Physiol*, 21(4):1231–1236, 1966.

[12] Diane Margel Robertson and Dennis C Smith. Compressive strength of mandibular bone as a function of microstructure and strain rate. *Journal of biomechanics*, 11(10):455–471, 1978.

[13] S Saha and WC Hayes. Relations between tensile impact properties and microstructure of compact bone. *Calcified tissue research*, 24(1):65–72, 1977.

[14] TM Wright and WC Hayes. Tensile testing of bone over a wide range of strain rates: effects of strain rate, microstructure and density. *Medical and biological engineering*, 14(6):671–680, 1976.

[15] David B Burr, Mark R Forwood, David P Fyhrie, R Bruce Martin, Mitchell B Schaffler, and Charles H Turner. Bone microdamage and skeletal fragility in osteoporotic and stress fractures. *Journal of Bone and Mineral Research*, 12(1):6–15, 1997.

[16] MB Schaffler, EL Radin, and DB Burr. Long-term fatigue behavior of compact bone at low strain magnitude and rate. *Bone*, 11(5):321–326, 1990.

[17] D Vashishth, JC Behiri, and W Bonfield. Crack growth resistance in cortical bone: concept of microcrack toughening. *Journal of Biomechanics*, 30(8):763–769, 1997.

[18] D Vashishth, KE Tanner, and W Bonfield. Contribution, development and morphology of microcracking in cortical bone during crack propagation. *Journal of Biomechanics*, 33(9):1169–1174, 2000.

[19] D Vashishth, KE Tanner, and W Bonfield. Experimental validation of a microcracking-based toughening mechanism for cortical bone. *Journal of Biomechanics*, 36(1):121–124, 2003.

[20] Fergal J OBrien, David Taylor, and T Clive Lee. Microcrack accumulation at different intervals during fatigue testing of compact bone. *Journal of Biomechanics*, 36(7):973–980, 2003.

[21] Peter Zioupos, Ulrich Hansen, and John D Currey. Microcracking damage and the fracture process in relation to strain rate in human cortical bone tensile failure. *Journal of biomechanics*, 41(14):2932–2939, 2008.

[22] HM Frost. Presence of microscopic cracks in vivo in bone. *Henry Ford Hosp Med Bull*, 8(2):35, 1960.

[23] P Zioupos, JD Currey, and AJ Sedman. An examination of the micromechanics of failure of bone and antler by acoustic emission tests and laser scanning confocal microscopy. *Medical engineering & physics*, 16(3):203–212, 1994.

[24] Gwendolen C Reilly and John D Currey. The development of microcracking and failure in bone depends on the loading mode to which it is adapted. *Journal of experimental biology*, 202(5):543–552, 1999.

[25] Ravi K Nalla, Jamie J Kruzic, and Robert O Ritchie. On the origin of the toughness of mineralized tissue: microcracking or crack bridging? *Bone*, 34(5):790–798, 2004.

[26] RK Nalla, JS Stölken, JH Kinney, and RO Ritchie. Fracture in human cortical bone: local fracture criteria and toughening mechanisms. *Journal of biomechanics*, 38(7):1517–1525, 2005.

[27] Robb M Kulin, Fengchun Jiang, and Kenneth S Vecchio. Loading rate effects on the¡ i¿ r¡/i¿-curve behavior of cortical bone. *Acta biomaterialia*, 7(2):724–732, 2011.

[28] AG Evans and KT Faber. Crack-growth resistance of microcracking brittle materials. *Journal of the American Ceramic Society*, 67(4):255–260, 1984.

[29] Anthony G Evans and Robert M McMeeking. On the toughening of ceramics by strong reinforcements. *Acta Metallurgica*, 34(12):2435–2441, 1986.

[30] David B Burr, Charles H Turner, Pratap Naick, Mark R Forwood, Walter Ambrosius, M Sayeed Hasan, and Ramana Pidaparti. Does microdamage accumulation affect the mechanical properties of bone? *Journal of Biomechanics*, 31(4):337–345, 1998.

[31] Gagik P Parsamian and Timothy L Norman. Diffuse damage accumulation in the fracture process zone of human cortical bone specimens and its influence on fracture toughness. *Journal of Materials Science: Materials in Medicine*, 12(9):779–783, 2001.

[32] JW Ager, G Balooch, and RO Ritchie. Fracture, aging, and disease in bone. *Journal of materials research*, 21(08):1878–1892, 2006.

[33] JC Behiri and W Bonfield. Orientation dependence of the fracture mechanics of cortical bone. *Journal of biomechanics*, 22(8):863–872, 1989.

[34] Jae-Young Rho, Liisa Kuhn-Spearing, and Peter Zioupos. Mechanical properties and the hierarchical structure of bone. *Medical engineering & physics*, 20(2):92–102, 1998.

[35] R Shahar, P Zaslansky, M Barak, AA Friesem, JD Currey, and S Weiner. Anisotropic poisson's ratio and compression modulus of cortical bone determined by speckle interferometry. *Journal of biomechanics*, 40(2):252–264, 2007.

[36] Y Tanabe, S Tanaka, M Sakamoto, T Hara, H Takahashi, and Y Koga. Influence of loading rate on anisotropy of compact bone. *Le Journal de Physique IV*, 1(C3):C3–305, 1991.

[37] Donald T Reilly and Albert H Burstein. The elastic and ultimate properties of compact bone tissue. *Journal of biomechanics*, 8(6):393–405, 1975.

[38] Wei Zhang, Srinivasan Arjun Tekalur, Melissa Baumann, and Laura R McCabe. The effects of damage accumulation on the tensile strength and toughness of compact bovine bone. *Journal of biomechanics*, 46(5):964–972, 2013.

[39] Karl F Graff. *Wave motion in elastic solids*. Courier Corporation, 2012.

[40] Fotios Katsamanis and Demetrios D Raftopoulos. Determination of mechanical properties of human femoral cortical bone by the hopkinson bar stress technique. *Journal of biomechanics*, 23(11):1173–1184, 1990.

[41] Kenneth S Vecchio and Fengchun Jiang. Improved pulse shaping to achieve constant strain rate and stress equilibrium in split-hopkinson pressure bar testing. *Metallurgical and materials transactions A*, 38(11):2655–2665, 2007.

[42] W Chen, B Zhang, and MJ Forrestal. A split hopkinson bar technique for low-impedance materials. *Experimental Mechanics*, 39(2):81–85, 1999.

[43] Guruswami Ravichandran and Ghatuparthi Subhash. Critical appraisal of limiting strain rates for compression testing of ceramics in a split hopkinson pressure bar. *Journal of the American Ceramic Society*, 77(1):263–267, 1994.

[44] Lal Ninan, J Tsai, and CT Sun. Use of split hopkinson pressure bar for testing off-axis composites. *International Journal of Impact Engineering*, 25(3):291–313, 2001.

Chapter 5

Investigating the Fracture and Toughening Mechanism of Cortical Bone Using XFEM and Multiscale Modeling Methods

5.1 Introduction

Osteon (also called secondary osteon) is the major bone unit of cortical bone in the microstructure level (from 10-500 μm) [1]. The primary constituent of osteon bone is osteon, which grows along the loading axis and comprises a center Haversian system surrounded by cylindrical lamellae formed by collagen fibrils and embedded mineral in nanostructure level (from a few hundred nanometers to 1 μm). Osteon bone resembles the fiber-reinforced composite with a higher Young's modulus and tensile strength along the osteonal direction or the loading axis, and lower ones in the transverse direction which is perpendicular to the loading axis. The boundary between osteons and surrounding bone tissue (interstitial bone), called the cement line, exhibits different morphology and composition compared to its surrounding osteon [2] and is hypothesized to serve as a barrier or ductile interface between osteons and interstitial bone. Although extensive studies have been focusing on the fracture and toughening mechanism of cortical bone, the correlations between microstructure and microcracking, fracture toughness, and failure mechanism of bone has not yet been fully understood.

It has been shown that crack deflection, microcracking, and uncracked ligament bridging are the major toughening mechanisms of cortical bone [3, 4, 5, 6, 7]. Micocracking formed ahead of the crack tip increasing the inherent fracture resistance of bone is the intrinsic toughening mechanism; the uncracked ligaments operated in the wake of the crack tip preventing the two newly formed crack edges from falling apart is the extrinsic toughening mechanism. The raising R-curve behavior observed [8, 6, 7] is believed to be due to contributions of the above two toughening mechanisms. The deflection of cracks is potentially due to the interference of cement lines, which prevent cracks from penetrating through osteons to lead to a catastrophic failure. A cement line is shown to be of lower mineralization compared to its surrounded osteon [9]. Thus, this soft interface separates osteons from interstitial bone to prevent microcracks from propagating into osteons. The above hypothesis supports the claim that osteon bone has a higher fracture toughness compared to primary bone, although its Young's modulus and strength is lower than the primary bone [10].

Limited in the ability to capture moving microcracks, differentiate the roles of bone constituents, and bridge macro- and micro-scale mechanics, experimental methods alone seem unable to provide full insight into the fracture and toughening mechanism of bone. Thus, finite element modeling (FEM) has been widely used in bone fracture study. Cohesive element with linear fracture mechanics method (LFEM) [11] is one of the major techniques used to study the interaction of microcracking and microstructure. Although the cohesive element method is capable of capturing interface delaminating behaviors, the cracking path is specified and is mesh dependent. Thus, it may not be applicable in the case of path independent microcracking.

A newly developed FEM technique, XFEM, solved the singular problems at the crack tip by adding a discontinuous jump function across the crack surfaces to the traditional shape function [12, 13, 14]. XFEM does not require conforming mesh to the geometry of discontinuities and cracks can propagate along an arbitrary path. Thus, XFEM is suitable for modeling fracture of cortical bone.

In the present dissertation, the XFEM technique for discontinuities is used to investigate the interaction between microcracking, fracture, microstructure, and its mechanical properties. The fracture toughness of a compact tensile specimen (CTS) of cortical bone is simulated. The simulations studied the significant role of cement lines in cortical bone fracture mechanism by calculating fracture toughness at various modulus ratios, various fracture energy ratios, and initial damage ratios of cement line and osteon. The osteon size effect on the fracture toughness is also investigated. To study the role of density and size of osteons and the properties of each constituent on the tensile strength of cortical bone, a multiple-scale modeling approach [15] based on the classical homogenization scheme was used to investigate the tensile behavior of cortical bone subjected to uniaxial tensile loading. To evaluate the orientation effects, the simulated compact bovine was loaded in the longitudinal and transverse directions, respectively. Lastly, a semi-concurrent modeling scheme for impact testing simulations was developed and implemented in ABAQUS/EXPLICIT 6.11 to study the role of cement lines on the impact behavior of bone.

5.2 Methods

5.2.1 Multi-Scale Modeling of Uniaxial Tensile Testing

The multiscale modeling approach proposed by Kouznetsova [15] bridges the microstructure to the macroscale behavior by the classic computational homogenization scheme [16, 17]. The deformation gradient from the macro-model is imposed on the microstructural representative volume element (RVE) to form a microscopic boundary value problem. The results obtained by solving the microscopic boundary problem are the variable input to compute the macroscopic output.

The scheme of macro-micro-macro transition relies on three hypotheses: volume averaging theorem, separation of microscale and macroscale, and the global periodicity. The macro-micro couplings including deformation gradient coupling, stress coupling, and internal energy coupling are implemented by the volume averaging theorem. The deformation gradient coupling [15] can be determined from the following equations:

The stress couplings

$$F_M = \frac{1}{V_0} \int\limits_{V_0} F_m dV_0 \tag{5.1}$$

$$P_M = \frac{1}{V_0} \int\limits_{V_0} P_m dV_0 \tag{5.2}$$

$$\sigma_M = \frac{1}{\det(F_M)} P_M \bullet F_M^T \tag{5.3}$$

The internal work coupling

$$\frac{1}{V_0} \int P_m : \delta F_m^T dV_0 = P_M : \delta F_m^T \tag{5.4}$$

where V_0 is the initial RVE volume; F_M is the macroscopic deformation gradient tensor; F_m is the microscopic deformation gradient tensor; P_M is the macroscopic first piola-Kirchhoff stress tensor; P_m is the microscopic first piola-Kirchhoff stress tensor; σ_M is the macroscopic Cauchy stress tensor; and σ_m is the microscopic Cauchy stress tensor.

The separation of two scales requires that the dimension of RVE must be much smaller than the dimension of the macro-model so that the gradient is constant for RVE. Based on the continuity condition of composite materials, a periodic boundary condition is assumed [15].

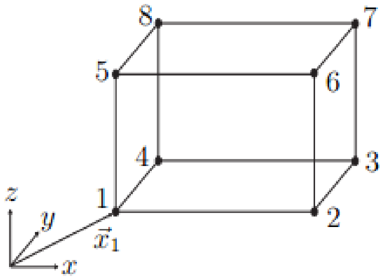

Figure 5.1 Schematic picture of the corner nodes numbering for a RVE in 3D view.

The computational homogenization multiscale problem can be solved numerically using the FEM method. Fig. 5.1 shows a schematic 3D RVE with the numbers of the 8 corner nodes. The corner nodes of 1, 2, 4, 5, are the master nodes. In order to preserve the periodicity of RVE at the deformed state, the displacements of the master corner nodes and the surface pairs (top and bottom, right and left, and front and back) should be correlated as follows [15]:

$$\vec{u}_{top} = \vec{u}_{bottom} + \vec{u}_5 - \vec{u}_1 \tag{5.5}$$

$$\vec{u}_{right} = \vec{u}_{left} + \vec{u}_2 - \vec{u}_1 \tag{5.6}$$

$$\vec{u}_{front} = \vec{u}_{back} + \vec{u}_1 - \vec{u}_4 \tag{5.7}$$

where $\vec{u}_1$, $\vec{u}_2$, $\vec{u}_4$, $\vec{u}_5$ are the initial displacement vectors of the four master corner nodes; the $\vec{u}_{top}$ and $\vec{u}_{bottom}$, $\vec{u}_{right}$ and $\vec{u}_{left}$, $\vec{u}_{front}$ and $\vec{u}_{back}$ are the initial displacement vectors for the perspective pair of nodes on the three pair of surfaces.

Thus, the above applied constraints implied that the total deformation of the RVE can be imposed by the displacement of the four corner nodes. P^M and σ^M can be computed by [15]

$$P_M = \frac{1}{V_0}\left\{\vec{f}_1^e\vec{x}_{0_1} + \vec{f}_2^e\vec{x}_{0_2} + \vec{f}_4^e\vec{x}_{0_4} + \vec{f}_5^e\vec{x}_{0_5}\right\} = \frac{1}{V_0}\sum_{p=1,2,4,5}\vec{f}_p^e\vec{x}_p \tag{5.8}$$

$$\sigma_M = \frac{1}{V}\left\{\vec{f}_1^e\vec{x}_1 + \vec{f}_2^e\vec{x}_2 + \vec{f}_4^e\vec{x}_4 + \vec{f}_5^e\vec{x}_5\right\} = \frac{1}{V}\sum_{p=1,2,4,5}\vec{f}_p^e\vec{x}_p \tag{5.9}$$

where f_p is the reaction external forces acted on four corner nodes, 1,2,4,5. Tangent stiffness tensor can be computed as [15]

$$^4C_M^\tau = \frac{1}{V_0}\sum_i\sum_j\left(\vec{x}_{(i)}K_M^{ij}\vec{x}_{(j)}\right)^{LT} : {}^4I^S + \ {}^4I \bullet \ \tau_M \tag{5.10}$$

$$\delta\tau_M = {}^4C_M^\tau : D_{\delta M} \quad \tau_M = \det(F_M)\sigma_M \ D_{\delta M} = \frac{1}{2}(L_{\delta M} + L_{\delta M}^T) \tag{5.11}$$

where K_M^{ij} is the component of RVE reduced stiffness matrix,K_M,${}^4I^S$, and ${}^4I$ are the symmetric fourth-order unit tensor and fourth-order unit tensor, respectively.

In the microscopic level, osteon with a central canal (Harvension system), cement line, and interstitial bone (matrix) are the three major continents of osteon bone. Fig. 5.2a shows a typical microscopic image of a bovine cortical bone. A microstructural RVE for osteon bone chosen to represent the microstructure of cortical bone in the multiscale modeling is shown in Fig. 5.2b. The RVE was cubic with a dimension of 500x500x500 *mu*m. The diameters of the central canals and width of the cement lines were kept as constant values, 35 *mu*m and 5 *mu*m respectively. The diameters of osteons were selected in the range of 100 to 200 *mu*m [14]. The various microstructure configurations for the RVE are summarized in Table 5.1. To study the osteon size effects, the area percentage occupied by the secondary osteon was kept constant and the diameters of the osteons were varied (Cases 1 to 4 (longitudinal direction) and Cases 5 to 8 (transverse direction) in Table

5.1). To study the effects of the area percentage occupied by osteons, the diameter of osteons were kept constant and the area percentage was varied (Case 4&9, longitudinal direction and Case 8&10, transverse direction). All the microstructure configurations were generated by a MATLAB code with random distributions of osteons in the matrix. The dimensions and loading conditions of the macro-model resembled the uniaxial tensile testing by Zhang [18]: a dog bone specimen with dimensions of 60x8x2 mm was loaded in a constant speed of 0.1 mm/s.

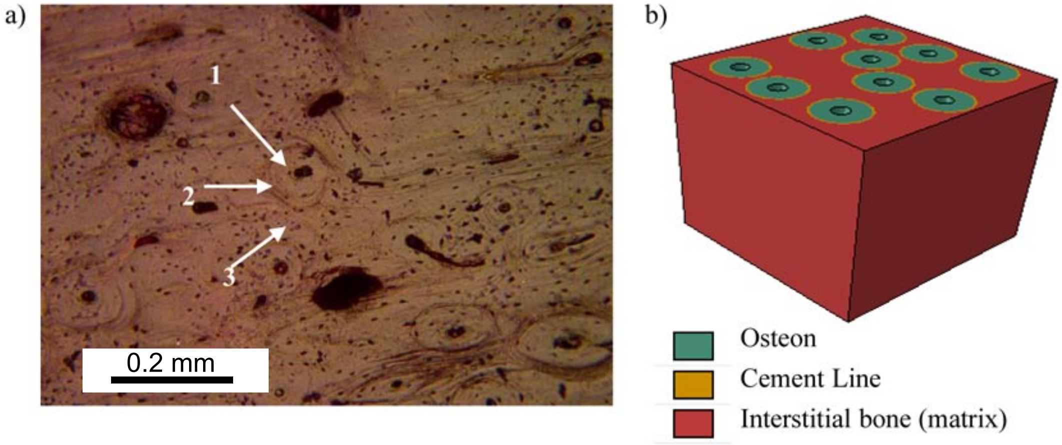

Figure 5.2 a) Microstructure of cortical bone: 1) Osteon, 2) Cement line, 3) Interstitial bone, b) RVE.

Table 5.1 Cortical bone with various microstructures simulated in the uniaxial tensile testing.

Case No.	Numbers of Osteons	Diameter of Osteon (mm)	Area Percentage Occupied by Osteon %	Loading Direction
1	3	0.19271	35	Longitudinal
2	5	0.14927	35	Longitudinal
3	7	0.12616	35	Longitudinal
4	10	0.10555	35	Longitudinal
5	3	0.19271	35	Transverse
6	5	0.14927	35	Transverse
7	7	0.12616	35	Transverse
8	10	0.10555	35	Transverse
9	5	0.10555	17.5	Longitudinal
10	5	0.10555	17.5	Transverse

The simulations were implemented by the commercial FEA software ABAQUS/Standard 6.11 with two user subroutines coded by FORTRAN, which was compiled by Intel (R) Visual Fortran

Compiler Version 11.1.072. The materials of the RVE components were defined by using the ABAQUS built-in material models. Osteons and interstitial bone (matrix) were treated as transversely isotropic and cement lines were treated as isotropic. The material properties of osteons and interstitial bone (matrix) used in the simulations are shown in Table 5.2.

Table 5.2 Elastic properties of osteon and matrix.

Elastic Properties	**Osteon**	**Matrix**
E_T (GPa)	11.51	12.66
E_L (GPa)	20.71	22.78
ν_T	0.17	0.153
ν_L	0.18	0.162
G_{TL} (GPa)	8.4	8.4
G_{TT} (GPa)	3.57	3.93

5.2.2 Characterizing the Fracture Toughness of Cortical Bone with Various Microstructures by XFEM

The dimensions and meshes of the C(T) specimen [19] simulated are shown in Fig. 5.3. It included two parts: Part 2, the area within the crack front, was the concerned zone; Part 1, the area away from the crack front, was less concerned. Thus, Part 2 was modeled with detailed microstructures of cortical bone including osteon, cement line, and interstitial bone, while part 1 was modeled as a bulk bone matrix. Boundary surfaces between Part 1 and Part 2 were tied together. The microstructures were created using the same method described in the previous section, as well as the dimensions of the three constituents also followed the same rules in the previous sections. The loading conditions complied to the ASTM E399 [19] by fixing the three translation degrees of freedom of one loading hole and moving another loading hole in z direction (Fig. 5.3) with a constant low speed (1 mm/s).

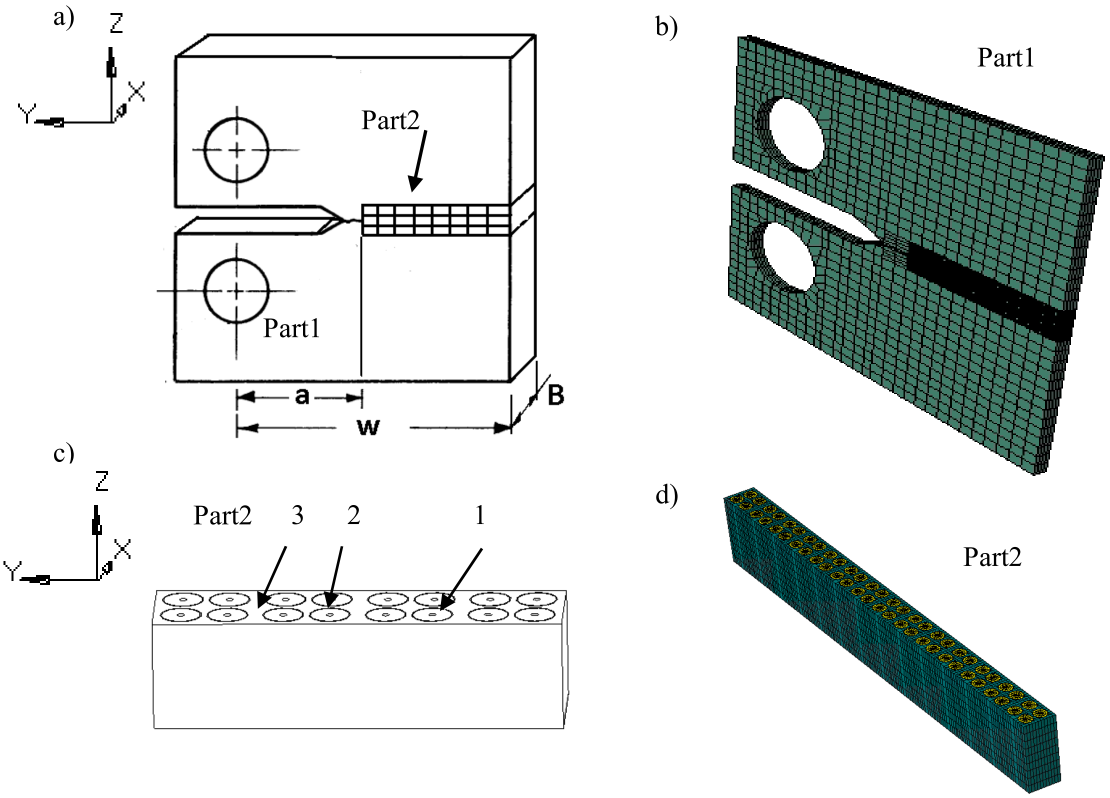

Figure 5.3 Meshes and dimensions of the C(T) specimen: a) Schematic drawing of C(T) specimen (Part 2 is the concerned zone with detailed microstructures of osteon bone; Part 1 is represented with bulk bone matrix without showing detailed microstructures): a=70 mm, W=140 mm, B=0.5 mm; b) Meshes of the C(T) specimen; c) Schematic drawing of the concerned zone (Part 2): 1: osteon, 2: cement line, 3: interstitial bone, d) Meshes of Part 2.

The fracture toughness, K_Q (MPa.m$^{1/2}$), is calculated as [19]

$$K_Q = \left(P_Q/BW^{1/2}\right) \bullet f(a/W) \tag{5.12}$$

where

$$f(a/w) = \frac{(2+a/W)(0.886+4.64a/W-13.32a^2/W^2+14.72a^3/W^3-5.6a^4/W^4)}{(1-a/W)^{3/2}} \tag{5.13}$$

P_Q is the load (kN) determined from the load-displacement curve following the rule of ASTM E399 [19]; B is the specimen thickness (cm) as shown in Fig. 5.3; W is the specimen width (cm) as shown in Fig. 5.3; a is the crack length (cm) as shown in Fig. 5.3.

The simulations were implemented by the commercial FEA software, ABAQUS/Standard. As quasi-brittle material, the fracture of cortical bone has been shown to be strain controlled [4]. Thus, the maximum principal strain failure criterion was chosen for the criterion of damage initiation and a mixed-mode, energy-based damage evolution law was chosen for the criterion of damage propagation. Initiation occurs when the maximum principal strain reaches a critical value ($\varepsilon^0_{\max}$)

$$f = \frac{(\varepsilon_n)}{\varepsilon^0_{\max}} \tag{5.14}$$

The relevant material data for the damage initiation and propagation of cortical bovine bone are as follows [14, 11]: $\sigma^0_{\max} = 40MPa$, $G_{IC} = 1374$N/m, $G_{IIC} = 4016$ N/m, $G_{IIIC} = 4016$ N/m. Where G_{IC} is the normal mode fracture energy, G_{IIC} is shear mode fracture energy for failure in the first shear direction, and G_{IIC} is the shear mode fracture energy for failure in the second shear direction. Since there is a lack of respective material data for individual constituents, it is assumed the osteon has the same properties as above, and the matrix takes a 10 percent increase of the matrix principal stress and a 10 percent decrease in Young's modulus. By changing the cement line properties, various configurations are studied to evaluate the interface effects on the fracture toughness of osteon bone.

5.2.3 Semi-Concurrent Multi-scale Modeling Approach for Modeling Impact Testing on Cortical Bone by ABAQUS/EXPLICIT

To investigate the role of cement lines on the impact behavior of bone, a semi-concurrent modeling scheme for impact testing simulations was developed and implemented in ABAQUS/EXPLICIT 6.11. The stress coupling in this approach is also based on the averaging theorem used in the computational homogenization scheme [15, 17, 20, 21]. It provides correct results only when the localization in RVE is absent. Thus, this method cannot predict failure. In this work, a method was developed to perform a halfway coupling from the macro-model to the micro-model. The boundary conditions of macro-model were passed to the micro-model through shape functions. Thus, deformation of the micro-model was concurrent to the macro-model. The analysis result of the micro-model provided an insightful view of how cement lines and osteons reacted to impact loading.

ABAQUS/EXPLICIT uses the explicit method [22] to solve dynamic equilibrium equations at each time increment, which does not enforce equilibrium of the internal forces with the externally applied loads. It updates the stiffness matrix based on geometry changes and material changes at the end of each time increment and then uses this stiffness matrix to calculate the next increment of load (or displacement) applied to the system. Thus, to avoid the drifting of results from the correct solution, a small time increment should be used in ABAQUS EXPLICIT. ABAQUS/STANDARD enforces equilibrium at each time increment by Newton-Raphson iterations. Thus, large time increment could be used in ABAQUS/STANDARD. However, it would require a reconstruction and a tangent stiffness matrix inversion at each iteration. The construction of the stiffness matrix can be computationally costly. Choosing the correct solver based on the analysis type is important for improving the accuracy and time efficiency of a FEM analysis. ABAQUS/EXPLICIT works better for impact problems and is chosen as the solver for the semi-concurrent approach.The computational framework of the semi-concurrent multi-scale modeling scheme is shown in Fig. 5.4.

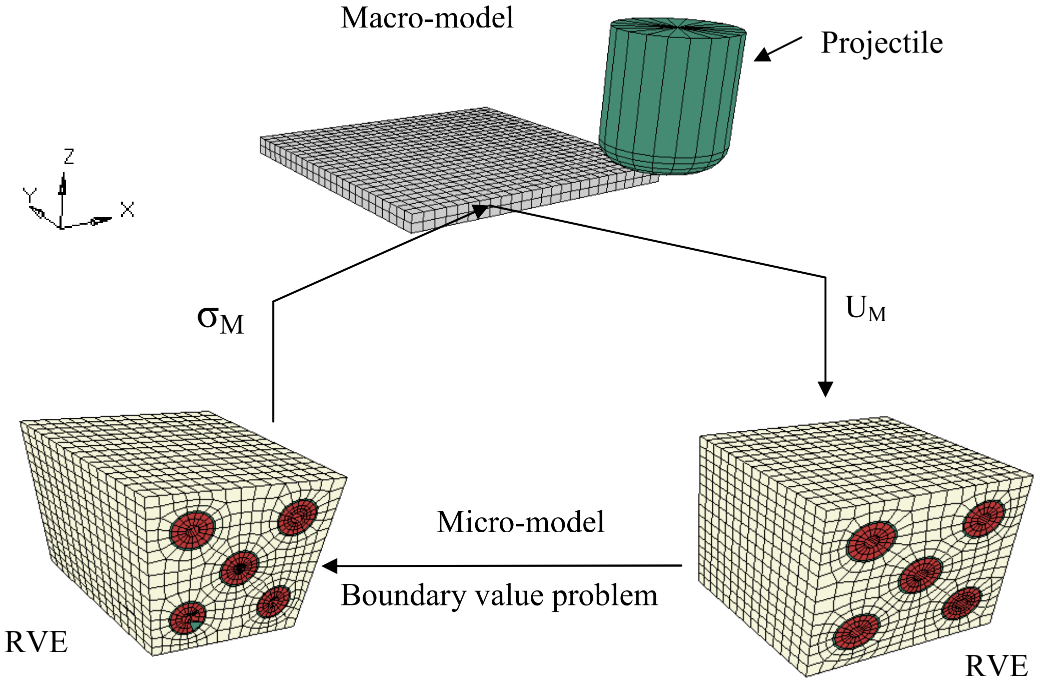

Figure 5.4 Computational framework of the concurrent multi-scale modeling scheme.

The plate simulated in the macro-model was a quarter of a plate with dimensions of 25x25 mm. The two surfaces of the corner under the projectile (Fig. 5.4) were simulated as symmetric along the x and y axes. One of the remaining two surfaces of the plate was set free, and another was fixed in the z direction. The plate was meshed with the element size equaling the size of RVE, 500x500x500 μm. A linear brick element with reduced integration point was chosen as the element type for both of the macro-model and micro-model. At each time increment, the boundary conditions of each element in the macro-model were passed to the 8 corner nodes of a corresponding RVE through ABAQUS subroutines. Then, in the micro-model, the boundary conditions of all the surface nodes were mapped through the nodal displacements of the 8 corner nodes of the RVE by the first order brick shape function

$$
\begin{aligned}
u = {} & (1/8)(1-g)(1-h)(1-r)u_1 + (1/8)(1+g)(1-h)(1-r)u_2 \\
& +(1/8)(1+g)(1+h)(1-r)u_3 + (1/8)(1-g)(1+h)(1-r)u_4 \\
& +(1/8)(1-g)(1-h)(1+r)u_5 + (1/8)(1+g)(1-h)(1+r)u_6 \\
& +(1/8)(1+g)(1+h)(1+r)u_7 + (1/8)(1-g)(1-h)(1+r)u_8
\end{aligned} \tag{5.15}
$$

where u_1, u_2, u_3, u_4, u_5, u_6, u_7, u_8 are the displacements of the 8 corner nodes passed from the macro-model; g, h, r are the local coordinates inside of RVE (Fig. 5.5).

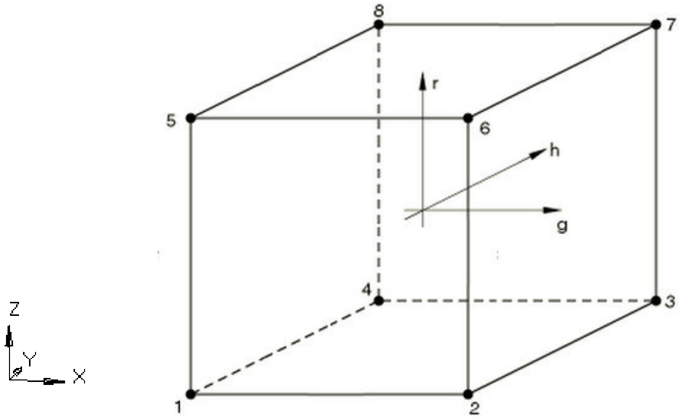

Figure 5.5 Schematic picture of RVE with both local and global coordinate systems.

Through the nodal mapping of the isoparametric interpolation, the boundary conditions of each element in the macro-model were copied to RVE. The advantage of this method is that the periodicity and continuity conditions are persevered without applying the prescribed linearly periodic boundary conditions for RVE in the traditional computational homogenization scheme [15, 17, 20].

The average stress theorem was applied to the first Piola-Kirchhoff stress tensor as well as the Cauchy stress tensor. For the macro first Piola-Kirchhoff stress, P_M, is given in terms of micro first Piola-Kirchhoff stress P_m as

$$P_M = \frac{1}{V_0} \int_{V_0} P_m \, dV_0 \tag{5.16}$$

where V_0 is the initial volume of RVE. After applying the divergence theorem, the P_M can be calculated as [15, 17]

$$P_M = \frac{1}{V_0} \int_{\Gamma_0} \vec{p}\vec{x}_0 \, d\Gamma_0 \tag{5.17}$$

where $\vec{p} = \vec{n}_0 \cdot P_m^T$ is the first Piola-Kirchhoff stress vector; x_0 is the position vector; Γ_0 is the surface of RVE.

After applying the boundary conditions, P_M, is further simplified as

$$P_M = \frac{1}{V_0} \left\{ \vec{f}_1^e \vec{x}_{0_1} + \vec{f}_2^e \vec{x}_{0_2} + \vec{f}_3^e \vec{x}_{0_3} + \cdots\cdots\cdots \vec{f}_n^e \vec{x}_{0_n} \right\} = \frac{1}{V_0} \sum_{p=1,2,3.....n} \vec{f}_p^e \vec{x}_p \tag{5.18}$$

where $\vec{f}_p^e$ is the reaction (resulting) external forces acted on the surface nodes of RVE [15, 17]. The Cauchy stress tensor σ_M then can be calculated as

$$\sigma_M = \frac{1}{det(F_M)} P_M \cdot F_M^T \tag{5.19}$$

where F_M is the deformation gradient at the integration point of element in the macro-model. The concurrent multiscale framework was implemented through ABAQUS/EXPLICIT through subroutine Vumat, Vdisp, and ABQMAIN. The flow chart showing the numerical implementation of the framework is shown in Fig. 5.6.

When Vumat was called at each integration point at every time increment, the nodal displacements (obtained through user subroutine 'Post_macro.for') of the element containing the integration point was passed to the subroutine Vdisp. In the meantime, the deformation gradient of the integration point was passed to 'Post_micro.for' for calculating Cauchy stress. Then the Cauchy

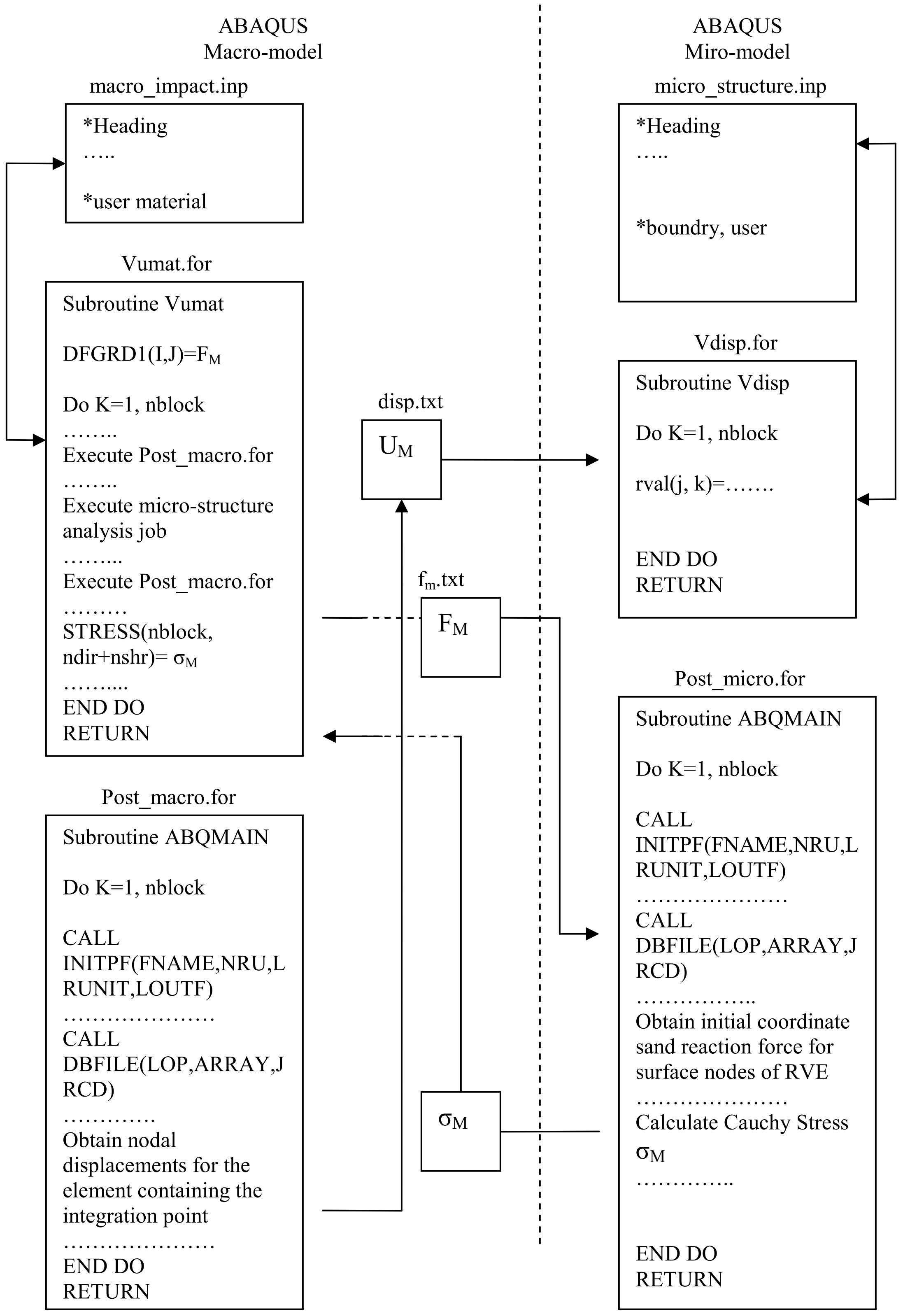

Figure 5.6 Numerical implementation flow chart of the concurrent multiscale modeling scheme in ABAQUS/EXPLICIT

Table 5.3 The geometric parameters and elastic properties of RVE for all the cases studied.

Case No.	1	2
Young's Modulus of Osteon E_T/E_L(GPa)	11.51/20.71	11.51/20.71
Young's Modulus of Matrix E_T/E_L(GPa)	12.66/22.78	12.66/22.78
Young's Modulus of Cement Line E (GPa)	11.51/20.71	5.755
Poisson's Ratio of Osteon v_T/v_L	0.17/0.18	0.17/0.18
Poisson's Ratio of Matrix v_T/v_L	0.153/0.162	0.153/0.162
Poisson's Ratio of Cement Line v	0.17/0.18	0.4
Shear Modulus of Osteon G_{TL}/G_{TT}(GPa)	8.4/8.4	8.4/8.4
Shear Modulus of Matrix G_{TL}/G_{TT}(GPa)	3.57/3.93	3.573.93
Shear Modulus of Cement Line G_{TL}/G_{TT}(GPa)	8.4/8.4	N/A
Numbers of Osteons	5	5
Diameter of Osteon (mm)	0.14927	0.14927
Area Percentage Occupied by Osteon %	35	35
Loading Direction	Transverse	Transverse

stress tenser was sent back to Vumat to complete one loop of analysis.

The geometric parameters and elastic properties are shown in Table 5.3. The geometry and mesh of the macro-model and micro-model are shown in Fig. 5.4. The mass of the projectile is 3.2 g and the impact speed is 300 m/s.

5.3 Results

5.3.1 Multiscale Modeling of Bovine Bone under Uniaxial Tensile Loading

The effective Young's moduli (both longitudinal and transverse directions) of osteon bone were calculated by the classical homogenization scheme to study the effects of osteon size and area percentage occupied by secondary osteons on the macro performance of cortical bone. The simulations resembled the real life uniaxial tensile testing with fixing the bottom of the dog-bone specimen and moving the top end with a constant speed of 0.1 mm/s. The reaction force at the top end is used to calculate engineering stress and the displacement at the top end is used to calculate the engineering strain. Fig. 5.7 shows both of the longitudinal and transverse Young's moduli decrease with an increase in osteon quantity (decrease in osteon diameter).The stress contours of a macro-model and the unit cell corresponding to one integration point are shown in Fig. 5.8 to illustrate how the unit cell interacts with the macro-model. To study the effects of the area occupied by secondary osteon, another two cases with area percentage occupied by secondary osteon of 17.5% were studied. All calculated Young's moduli for various cases are summarized in Table 5.4.

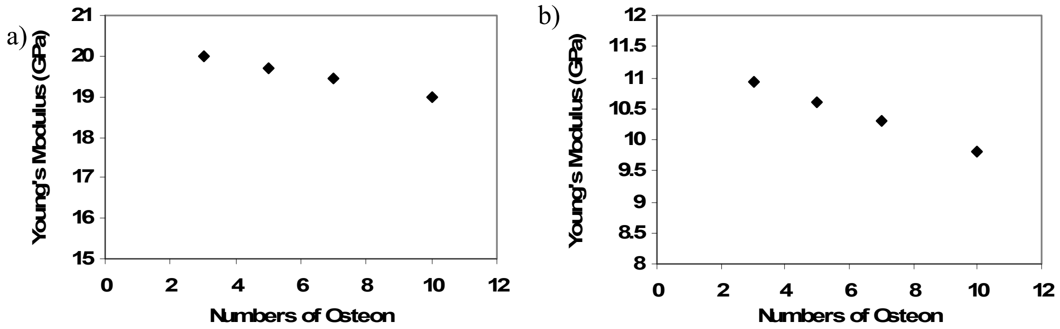

Figure 5.7 Effective Young's modulus versus osteon size for cortical bone with 35% area occupied by secondary osteon: (a) Longitudinal direction (b) Transverse direction.

5.3.2 Characterizing the Fracture Toughness of Cortical Bone with Various Microstructures by XFEM

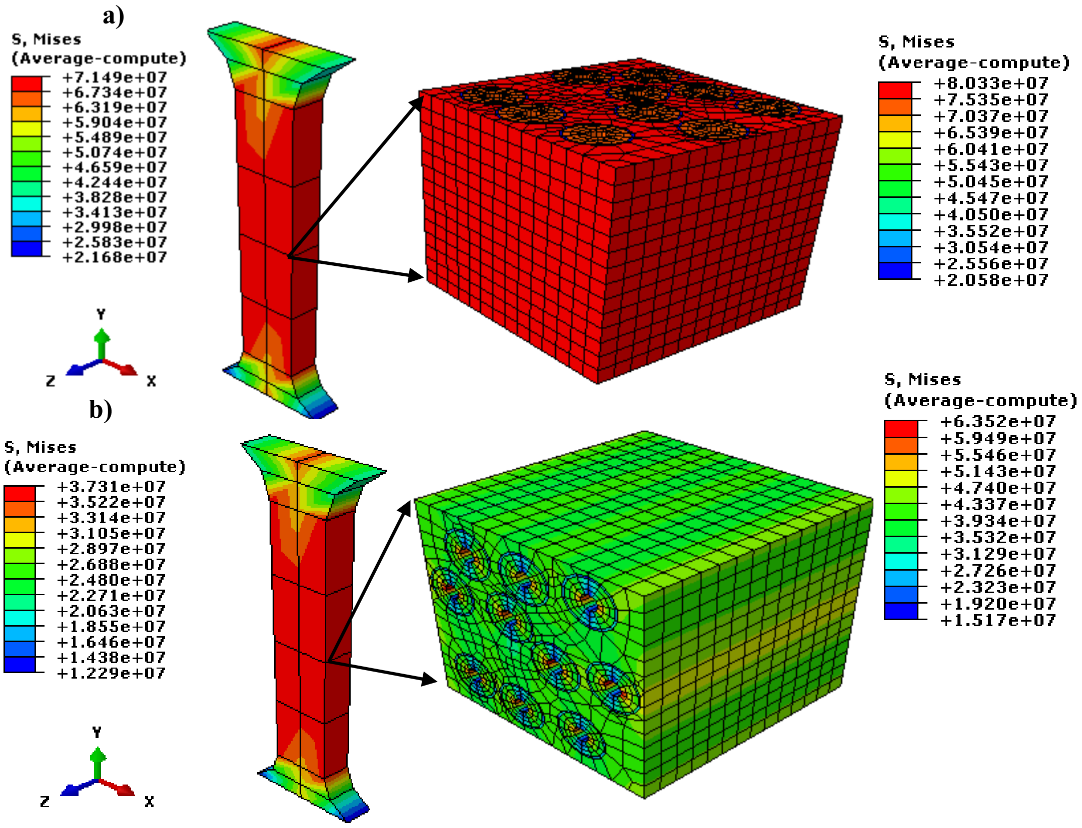

Figure 5.8 Stress contours of a macro-model and the unit cell corresponding to one of the integration points in macro-model: a) Longitudinal direction; b) Transverse direction.

Table 5.4 Summaries of calculated Young's moduli and their corresponding microstructures.

Case No.	Young's Modulus (GPa)	Numbers of Osteons	Diameter of Osteon (mm)	Area Percentage Occupied by Osteon %	Loading Direction
1	20.01	3	0.19271	35	Longitudinal
2	19.72	5	0.14927	35	Longitudinal
3	19.44	7	0.12616	35	Longitudinal
4	19.00	10	0.10555	35	Longitudinal
5	10.92	3	0.19271	35	Transverse
6	10.60	5	0.14927	35	Transverse
7	10.30	7	0.12616	35	Transverse
8	9.81	10	0.10555	35	Transverse
9	20.25	5	0.10555	17.5	Longitudinal
10	10.81	5	0.10555	17.5	Transverse

It has been shown in the literature[10, 3, 4, 5]that the microstructure of cortical bone has strong effects on its fracture toughness. The cement line seems to serve as a barrier to stop the microcrack from propagating through osteons. Although the osteon bone shows a lower Young's modulus and tensile strength than primary bones, the matrix-cement line-osteon microstructure enhances its resistance to fracture. Thus, in this section, the fracture toughness of various microstructure configurations was evaluated to study the interaction of osteon-cement line-interstitial bone with cracking. The force-displacement curves and the calculated fracture toughness for various configurations are shown in Fig. 5.9. The results for all the simulated configurations are shown in Table 5.5.

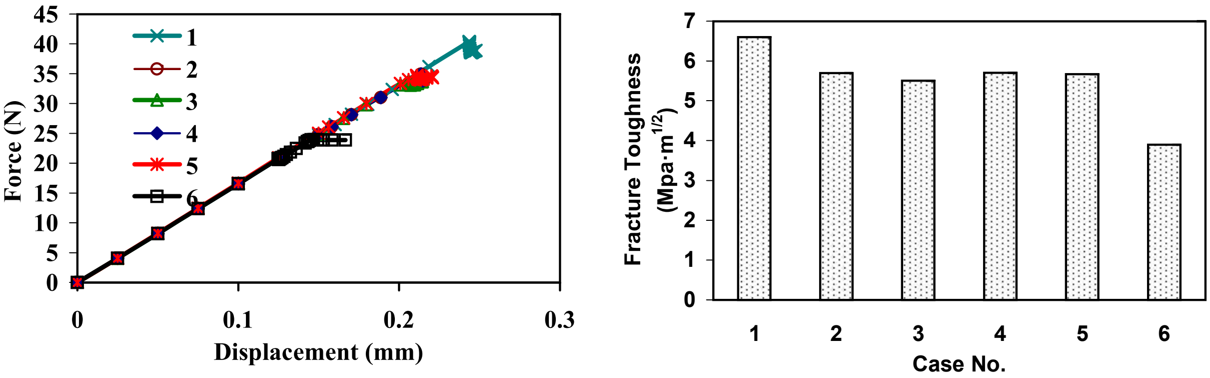

Figure 5.9 a) Force-displacement curve; b) Calculated fracture toughness.

Table 5.5 Summary of fracture toughness for all the cases studied.

Case No.	E_C/E_O	G_C/G_O	$\varepsilon_C/\varepsilon_O$	Orientation	K (MPa.m$^{1/2}$)
1	0.5	1	2	Transverse	6.6
2	0.5	1	1	Transverse	5.7
3	1	1	1	Transverse	5.51
4	0.5	0.5	1	Transverse	5.71
5	2	1	1	Transverse	5.67
6	0.5	1	0.5	Transverse	3.9

The maximum principal stress contours at the last increment of four studied cases are shown in Fig. 5.10. The top four contours show the crack extension on the CT specimen surface, the middle four contours show the crack extension in the osteon fibers, and the last four contours show the crack extension in the cement line. As shown in Table 5.5, the Young's modulus of the cement line is half that of the Osteon for Case 1, which yielded to a highest fracture toughness of all the cases

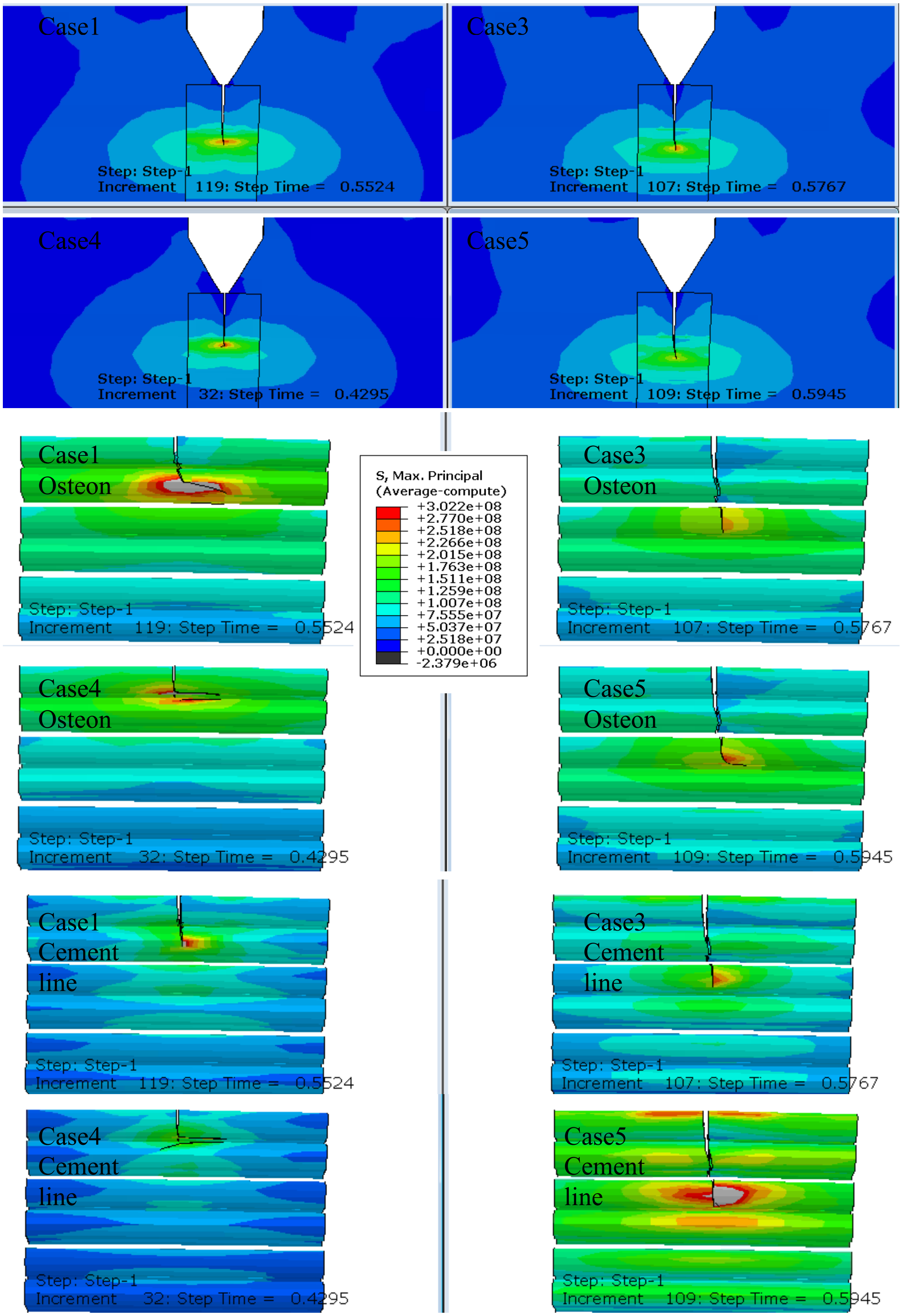

Figure 5.10 Stress contour at the last increment of the four of the cases (Case 1, 3, 4, and 5) studied in the CT fracture toughening simulations

studied. The second highest fracture toughness is Case 4 in which the Young's modulus is also half that of the osteon. The contour plots in Fig. 5.10 give an insightful view of how cracks propagated through the osteons and cement lines inside the bone matrix. It shows that cracks only propagated through the first two layers of osteons in Cases 1&4, and cracks penetrate three layers of osteons in Cases 3&5. The contours also showed that cracks tended to deflect along the longitudinal direction of osteons in Cases 1&4 instead of extending across osteons.

The fracture toughness of each simulated configuration at different crack extension was also calculated. The results are shown in Fig. 5.11.

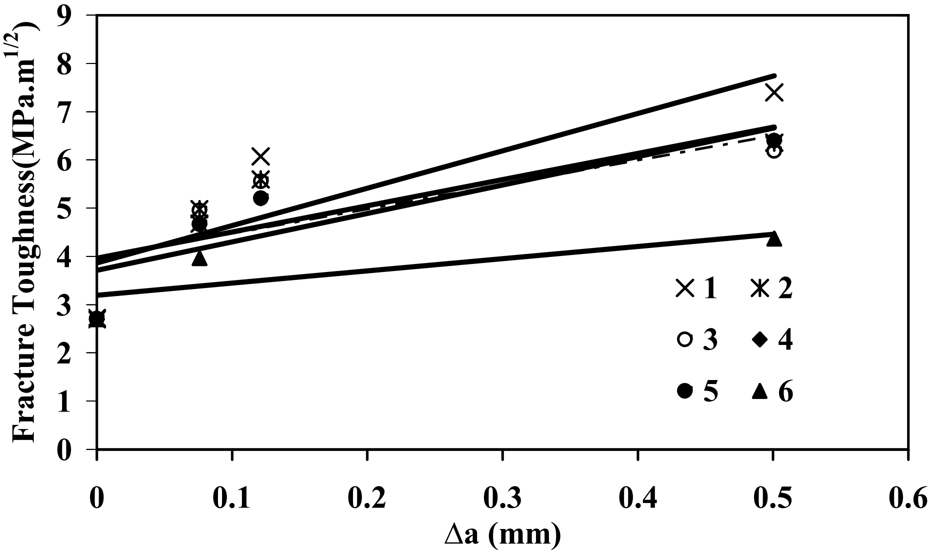

Figure 5.11 Fracture toughness versus cracking extension.

5.3.3 Semi-Concurrent Multi-scale Modeling of Impact Testing on Cortical Bone

The boundary conditions applied to the micro-model were passed from the element 25 of the macro-model (Fig. 5.12) at step time 0.6 ms. The results of the two cases (Table 5.5) studied are shown in Fig. 5.13. It can be seen that the maximum tensile stresses in osteons 3&4 were constrained to the osteons (see the stresses contour in the top figures in Fig. 5.13). However, in Case 1 the stresses in the two osteons extended to the surrounding interstitial bone. Furthermore, tensile stress zones were observed in Osteons 3&5 in Case 1, but not in Case 2. The results indicated that soft interface introduced by cement lines interfered with the wave traveling inside the bone. It worked as a barrier to separate osteons from the surrounding bone. Therefore, the cracks and failure were constrained in the local area, which prevented the macroscopic failure of cortical bone.

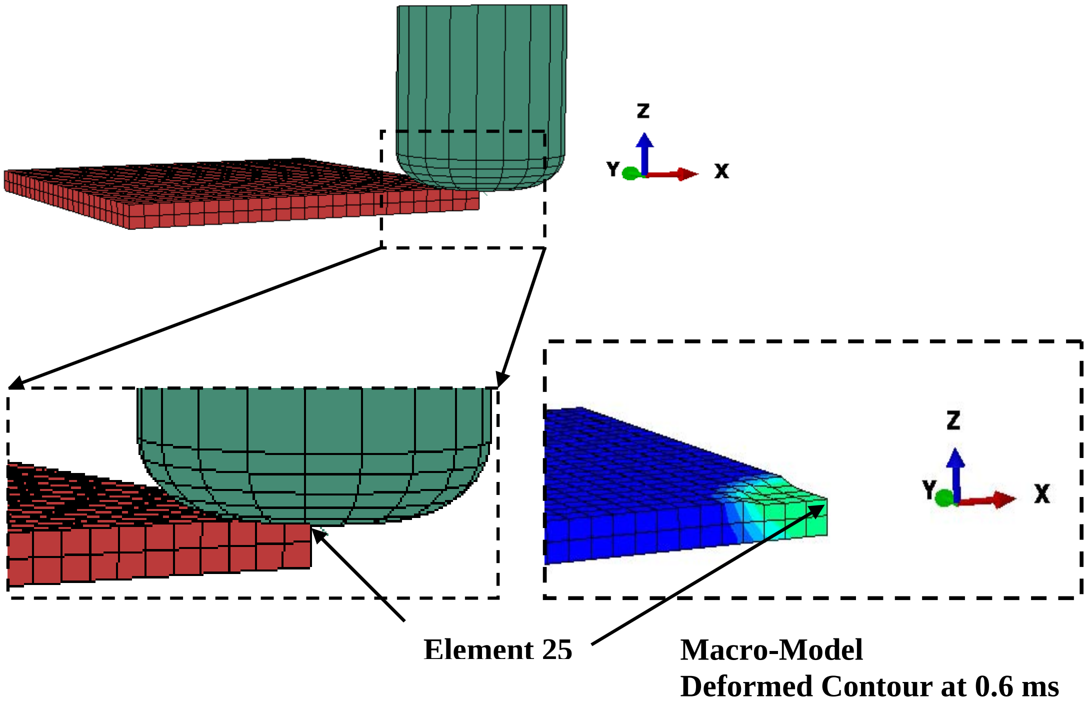

Figure 5.12 Geometry and mesh of macro-model of impact testing simulated.

5.4 Discussion

The multiscale modeling using classical homogenization method for evaluating the material properties of heterogeneous materials [23, 24, 25, 17, 20, 16] was used to evaluate the macroscopic

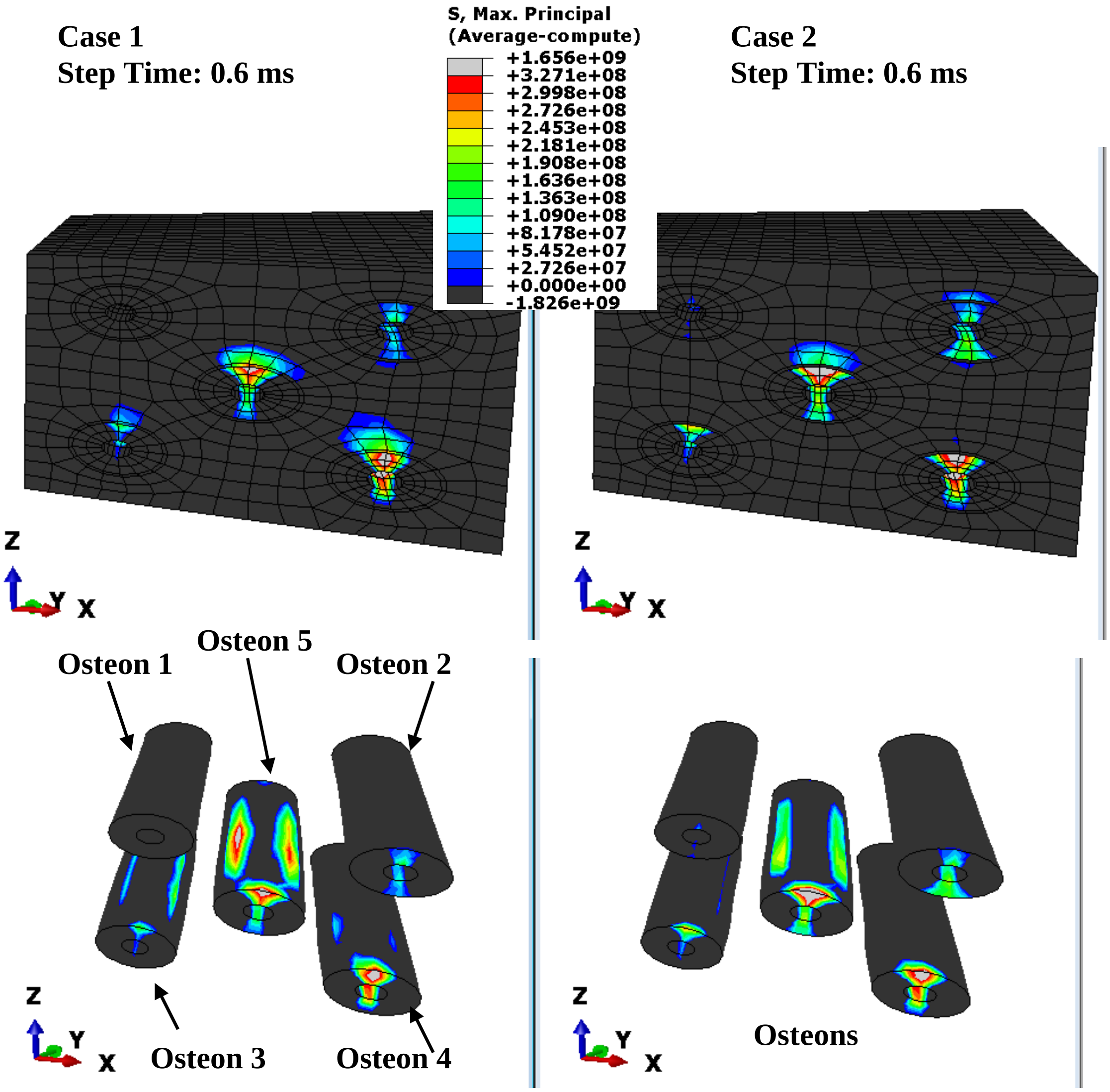

Figure 5.13 Stress contour of the two micro-models studied at impact time of 0.6 ms.

Young's modulus of cortical bone with various microstructure configurations. The Young's modulus in both longitudinal and transverse directions was found to decrease with the increase of numbers of osteon or decrease of the diameter of osteon with a constant area percentage occupied by secondary osteon. The reason is that increasing the numbers of osteon increases the porosity of the cortical bone because each osteon comprises a central canal, Harvention system.

The results also showed that macroscopic Young's modulus in the longitudinal direction decreased with the area percentage occupied by the secondary osteon with a constant osteon size. The results agree with the experimental observations in the literature. Saha and Hayes [10, 26] measured the tensile strength and the modulus of elasticity, which was found to be negatively correlated with the area percentage of secondary osteons.

However, the central canal and cement effects on the Young's modulus in the transverse direction are slightly different than in the longitudinal direction. The Young's modulus is 10.81 GPa with an area percentage of 17.5 and 5 osteons (Case 10). This value is slightly lower than the value, 10.98 GPa, with an area percentage of 35 and 3 osteons(Case 6) but larger than all the other cases. Thus, it seems that there exists an optimal diameter of osteons for the Young's modulus in the transverse direction. This difference between the effects of area occupied by secondary osteons on the Young's modulus of longitudinal and transverse directions is likely due to the effect of cement lines. Case 6, 7, and 8 include more osteons or more soft interfaces than case 10. Thus, lower Young's moduli were observed in Case 6, 7, and 8 than Case 10. However, compared to Case 10, Case 5 comprised less cement lines. Therefore, Case 5 exhibited a higher Young's modulus than Case 10. The experimental results of the uniaxial tensile testing of cortical bone in Chapter 4 also showed that cement lines weaken the cortical bone in transverse direction with that many microcracks instantly initiated in the cement lines resulting in a quick stiffness loss in the transverse specimen.

The fracture toughness of cortical bone was evaluated by XFEM method to investigate the role of cement lines in the fracture process of cortical bone. The fracture toughness calculated for all the cases studied are in the range of 3.9-6.6 MPa.m$^{1/2}$ (Table 5.5). The results agree with the literature [4, 3, 7]very well. The results also showed that a case with a Young's modulus of cement lines half of its surrounded osteon and a cracking initiation stain double of the surrounded osteon exhibited the highest fracture toughness among all the cases studied. However, a brittle cement line interface seemed to decrease the fracture toughness. The results agree with the experimental observation that the cement line acts as a barrier to stop or deflect the crack propagation. Crack deflection, microcracking, and uncracked ligament bridging are the major toughening mechanism of cortical bone [4, 3, 7, 6, 8, 5]. The simulations support the hypnosis that the osteon-cement line-interstitial bone has benefits in the bone fracture process and properties of cement lines play a critical role in it.

The effects of fracture energy including normal modes and two shear models of cement lines on the fracture toughness of the C(T) specimen were also evaluated. In Case 4 and Case 2, all the other factors are kept the same besides the values of fracture energy. However, very close results were obtained for Case 2 and 4. Compared to the fracture initiation criterion, fracture evolution seemed to have less effect on the results.

The rising fracture resistance with the crack extension was also studied. The fracture toughness versus crack extension is plotted in Fig. 5.7. Linear regression lines are added to each case. The fracture toughness at zero crack extension for all the configurations studied was the same, $2.72 MPa.m^{1/2}$. This is due to the first layer at the precrack front was the interstitial bone, which has the same material properties for all the cases. After crack initiation, rising R-curve behavior was observed all the cases, which agrees with the literature very well [4]. Each case exhibited a different rising slope. Case 1 with a soft and ductile interface showed the steepest rising R-curve and case 6 with brittle interface seemed to exhibit a most flat rising R-curve among all the cases.

The role of cement lines on the impact behavior of cortical bone was also evaluated through the use of semi-concurrent modeling approach. The results showed that a RVE with a soft interface introduced by cement lines exhibited less damage in both interstitial bone and osteons than the RVE without cement line. Thus, the soft interface also benefits impact behavior of cortical bone, which may explain the higher impact resistance of osteon bone observed in the Charpy impact testing in Chapter 4.

Osteon bone comprising three constituents (secondary osteon, cement line, and interstitial bone) in the microscopic level is hypothesized to exhibit fiber-reinforced composite material behavior. With different morphology and composition compared to its surrounded osteon, the cement line is assumed to act as a barrier or soft interface to prevent microcrack penetrating through osteon to lead to a catastrophic failure. Understanding the micro interactions between cement, osteon, interstitial bone, and micorcracking helps disclose the fracture mechanism of cortical bone. In the present paper, the correlation between the micro components and the macro performance of osteon bone was studied using multi-scale modeling methods and XFEM technique. By using the classical computational homogenization method, the tensile moduli of cortical bone with various microstructures were evaluated. The Young?s moduli in both longitudinal and transverse directions were found to have a positive correlation with the diameter of osteons when the area percentage occupied by secondary osteons was kept constant. And Young's modulus in longitudinal direction was found to decrease with the increase of the area percentage occupied by secondary osteons. However, it seems that there exists an optimal diameter of osteons benefiting the Young's modulus in the transverse direction due to effects of the weaker interface introduced by cement lines. The fracture toughness of cortical bone with various micro configurations was characterized using the ABAQUS/XFEM technique. The highest fracture toughness was the case with a soft and ductile cement line interface. Raising R-curve behavior was observed. A semi-concurrent modeling scheme for impact loading simulations was developed and implemented in ABAQUS/EXPLICIT 6.11 to investigate the role of cement lines on the impact behavior of cortical bone. The study showed that soft interface introduced by cement lines interfering with the wave traveling inside the RVE (representative volume element) resulted in a mitigating in the micro damage compared to the RVE without cement lines.

REFERENCES

REFERENCES

[1] Jae-Young Rho, Liisa Kuhn-Spearing, and Peter Zioupos. Mechanical properties and the hierarchical structure of bone. *Medical engineering & physics*, 20(2):92–102, 1998.

[2] Mitchell B Schaffler, David B Burr, and Richard G Frederickson. Morphology of the osteonal cement line in human bone. *The Anatomical Record*, 217(3):223–228, 1987.

[3] Ravi K Nalla, Jamie J Kruzic, and Robert O Ritchie. On the origin of the toughness of mineralized tissue: microcracking or crack bridging? *Bone*, 34(5):790–798, 2004.

[4] RK Nalla, JS Stölken, JH Kinney, and RO Ritchie. Fracture in human cortical bone: local fracture criteria and toughening mechanisms. *Journal of biomechanics*, 38(7):1517–1525, 2005.

[5] Fergal J O'Brien, David Taylor, and T Clive Lee. Microcrack accumulation at different intervals during fatigue testing of compact bone. *Journal of Biomechanics*, 36(7):973–980, 2003.

[6] D Vashishth, KE Tanner, and W Bonfield. Contribution, development and morphology of microcracking in cortical bone during crack propagation. *Journal of Biomechanics*, 33(9):1169–1174, 2000.

[7] D Vashishth, KE Tanner, and W Bonfield. Experimental validation of a microcracking-based toughening mechanism for cortical bone. *Journal of Biomechanics*, 36(1):121–124, 2003.

[8] D Vashishth, JC Behiri, and W Bonfield. Crack growth resistance in cortical bone: concept of microcrack toughening. *Journal of Biomechanics*, 30(8):763–769, 1997.

[9] David B Burr, Mitchell B Schaffler, and Richard G Frederickson. Composition of the cement line and its possible mechanical role as a local interface in human compact bone. *Journal of Biomechanics*, 21(11):939–945, 1988.

[10] S Saha and WC Hayes. Relations between tensile impact properties and microstructure of compact bone. *Calcified tissue research*, 24(1):65–72, 1977.

[11] Susan Mischinski and Ani Ural. Finite element modeling of microcrack growth in cortical bone. *Journal of Applied Mechanics*, 78(4):041016, 2011.

[12] Ted Belytschko and Tom Black. Elastic crack growth in finite elements with minimal remeshing. *International journal for numerical methods in engineering*, 45(5):601–620, 1999.

[13] Ted Belytschko, Nicolas Moës, Shuji Usui, and Chandu Parimi. Arbitrary discontinuities in finite elements. *International Journal for Numerical Methods in Engineering*, 50(4):993–1013, 2001.

[14] Élisa Budyn and Thierry Hoc. Multiple scale modeling for cortical bone fracture in tension using x-fem. *European Journal of Computational Mechanics/Revue Européenne de Mécanique Numérique*, 16(2):213–236, 2007.

[15] Varvara Kouznetsova, Wouter Wilson, and Marc Geers. Multi-scale modeling of textile composites thiam wai chua mt 10.19. 2011.

[16] V Kouznetsova, WAM Brekelmans, and FPT Baaijens. An approach to micro-macro modeling of heterogeneous materials. *Computational Mechanics*, 27(1):37–48, 2001.

[17] Varvara Kouznetsova, Marc GD Geers, and WA Marcel Brekelmans. Multi-scale constitutive modelling of heterogeneous materials with a gradient-enhanced computational homogenization scheme. *International Journal for Numerical Methods in Engineering*, 54(8):1235–1260, 2002.

[18] Wei Zhang, Srinivasan Arjun Tekalur, Melissa Baumann, and Laura R McCabe. The effects of damage accumulation on the tensile strength and toughness of compact bovine bone. *Journal of biomechanics*, 46(5):964–972, 2013.

[19] ASTM Designation. E399-90. standard test method for plane-strain fracture toughness of metallic materials. *1991 Annual Book of ASTM Standards*, 3:485–51, 1997.

[20] VG Kouznetsova, MGD Geers, and WAM Brekelmans. Multi-scale second-order computational homogenization of multi-phase materials: a nested finite element solution strategy. *Computer Methods in Applied Mechanics and Engineering*, 193(48):5525–5550, 2004.

[21] Stefan Loehnert, L Krstulovic-Opara, Matej Vesenjak, and Dana Mueller-Hoeppe. Homogenization principle based multi-scale modeling of cellular structures. *Journal of the Serbian Society for Computational Mechanics/Vol*, 4(2):97–109, 2010.

[22] ABAQUS Version. 6.11 documentation. *Dassault Systemes Simulia Corp., Providence, RI, USA*, 2011.

[23] Christian Miehe, Jörg Schröder, and Martin Becker. Computational homogenization analysis in finite elasticity: material and structural instabilities on the micro-and macro-scales of periodic composites and their interaction. *Computer Methods in Applied Mechanics and Engineering*, 191(44):4971–5005, 2002.

[24] Christian Miehe and Nikolas Apel. Anisotropic elastic–plastic analysis of shells at large strains. a comparison of multiplicative and additive approaches to enhanced finite element design and constitutive modelling. *International journal for numerical methods in engineering*, 61(12):2067–2113, 2004.

[25] PE McHugh, RJ Asaro, and CF Shih. Computational modeling of metal matrix composite materials. *Modeling the deformation of crystalline solids*, 1991.

[26] S Saha and WC Hayes. Tensile impact properties of human compact bone. *Journal of biomechanics*, 9(4):243–251, 1976.

Chapter 6

Conclusion

6.1 New and Original Contributions Made

Low velocity drop weight impact tests were conducted to evaluate the threshold conditions indicating the onset of damage and failure mechanism of monolithic and bi-layered PMMA and PC plates. A material model based on the Arruda and Boyces physical model for amorphous polymers was coded and implemented in ABAQUS/EXPLICIT to predict the strain rate and pressure dependent behavior of polymers. The impact behavior of monolithic PMMA and PC and layered PMMA/PC laminate at low and high impact loading were numerically investigated by use of ABAQUS/EXPLICIT. The failure mechanism, crack pattern, and energy dissipation were transversely compared. The FEM simulation provided a comprehensive insight into the energy dissipation and toughening mechanism of the impact events. An optimal design was performed interactively using the optimization tool in MATLAB and commercial finite element modeling (FEM) software ABAQUS/EXPLICIT to study the effects of aspect ratio, material properties of PMMA and PC, etc., on the toughening mechanism of the laminate panel. This work serves as a design tool for effectively choosing materials and structures for optimizing ballistic performance of ceramic-plastic laminate-based armor.

The prior literature on bone failure and fracture mechanism showed that the microcracking toughening mechanism is one of the major toughening mechanisms of cortical bone by use of the post-processing microcracking detection technique. In this research work, the microcracking toughening mechanism was visualized concurrently with the fracture process of cortical bones subjected to uniaxial tensile loading. Strain hardening and softening were observed in the longitudinal and transverse specimens respectively. The microcracking in the transverse specimens were found to instantly increase to peak after yielding compared to the gradual growth until failure in the longitudinal specimens. Transverse specimens showed that many microcracks instantly initiated in the cement lines, which resulted in the stiffness loss in the specimen. The present results showed that, to some extent, microcracking serves as a toughening mechanism; but if it is over a critical value, microcracking weakens the specimen instead. The Charpy impact testing and the SHPB high strain rate uniaxial tensile testing were conducted to study the failure behavior of the cortical bone under high strain rate loading. The results showed that microcracking seems to not be the toughening mechanism of cortical bone at high strain rate failure. Rather, it is the unique osteon-cement line-interstitial bone microstructure, which plays an important role in toughening the failure behavior of the cortical bone at high strain rate. A multiscale modeling based on the classic first order homogenization scheme was implemented in ABAQUS/STANDARD to study the constitutive behavior of the cortical bone in terms of the osteon size, orientation, and area percentage occupied by osteon. The computational results verified the experimental observations that tensile modulus of cortical bone has a negative correlation with the area percentage occupied by osteon. XFEM element with linear fracture mechanics method was used to evaluate the role of cement line, osteon, interstitial bone, and their corresponding mechanical properties on the fracture toughness of bone. The results numerically proved that the experimental observation that cement lines, the soft interface between osteon and its surrounding bone matrix, act as barriers to stop or deflect the crack propagation. A semi-concurrent modeling scheme for impact loading simulations was proposed and implemented in ABAQUS/EXPLICIT to investigate the role of cement lines on the impact behavior of the cortical bone. The study showed that the soft interface introduced by cement lines interferes with the wave traveling inside the RVE, resulting in a greater mitigation in the micro damage compared to an RVE without cement lines. The research work provides inspiration for bone replacement material and impact resistance material design and synthesis, as well as improving the understanding of bone fracture.

6.2 Future Work

As for future work, three research directions extended from this work would be interesting: methods bridging failures of RVE to the failure of macro-model for both ABAQUS/STANDARD and ABAQUS/EXPLICIT, an optimization scheme for multiscale modeling, and mesh independent cracking method. Although multiscale modeling methods have been studied and developed extensively in the past decades, bridging the micro and macro failure is still challenging nowadays. Similar difficulties exists in the mesh independent cracking method. Although ABAQUS/XFEM is a crack path and remeshing independent, it fails to converge when multi-cracks are initiated in one element. Advance in the computational failure and cracking method is the key for resembling the real life failure behavior of materials in simulations. Optimization method for multiscale modeling is also of great engineering interest for material optimal design.